University of São Paulo
Physics Institute

Turbulent temperature fluctuations in TCABR tokamak

Wilson Andres Hernandez Baquero

Supervisor: Prof. Dr. Zwinglio de Oliveira Guimarães Filho

Thesis submitted to the Physics Institute of the University of São Paulo in partial fulfillment of the requirements for the degree of Doctor of Science.

Examining Committee:
Prof. Dr. Zwinglio de Oliveira Guimarães Filho - Supervisor (IFUSP)
Prof. Dr. Iberê Luiz Caldas (IFUSP)
Prof. Dr. Ivan Cunha Nascimento (IFUSP)
Prof. Dr. Dennis Lozano Toufen (IFS)
Prof. Dr. Munemasa Machida (UNICAMP)

São Paulo
2017

FICHA CATALOGRÁFICA
Preparada pelo Serviço de Biblioteca e Informação do Instituto de Física da Universidade de São Paulo

Baquero, Wilson Andres Hernandez

Flutuações turbulentas de temperature no tokamak TCABR / Turbulent temperature fluctuactions in TCABR tokamak. São Paulo, 2017.

Tese (Doutorado) – Universidade de São Paulo. Instituto de Física. Depto. de Física Aplicada.

Orientador: Prof. Dr. Zwinglio de Oliveira Guimarães Filho
Área de Concentração: Física dos Plasmas

Unitermos: 1. Turbulência; 2. Sonda; 3. Temperatura.

USP/IF/SBI-122/2017

Universidade de São Paulo
Instituto de Física

Flutuações turbulentas de temperatura no tokamak TCABR

Wilson Andres Hernandez Baquero

Orientador: Prof. Dr. Zwinglio de Oliveira Guimarães Filho

Tese de doutorado apresentada ao Instituto de Física da Universidade de São Paulo, como requisito parcial para a obtenção do título de Doutor em Ciências.

Banca Examinadora:
Prof. Dr. Zwinglio de Oliveira Guimarães Filho - Orientador (IFUSP)
Prof. Dr. Iberê Luiz Caldas (IFUSP)
Prof. Dr. Ivan Cunha Nascimento (IFUSP)
Prof. Dr. Dennis Lozano Toufen (IFS)
Prof. Dr. Munemasa Machida (UNICAMP)

São Paulo
2017

A las personas que quiero....

En un alba sin pájaros el mago vio cernirse contra los muros el incendio concéntrico. Por un instante, pensó refugiarse en las aguas, pero luego comprendió que la muerte venía a coronar su vejez y a absolverlo de sus trabajos. Caminó contra los jirones de fuego. Éstos no mordieron su carne, éstos lo acariciaron y lo inundaron sin calor y sin combustión. Con alivio, con humillación, con terror, comprendió que él también era una apariencia, que otro estaba soñándolo.
Las ruinas circulares, Jorge L. Borges.

Acknowledgements

Special thanks to professor Zwinglio Guimarães-Filho for their advice.

I would like to thank the TCABR tokamak group, specially Nelio, Alexandre and Ablicio for their help.

To CPG, especially to Eber.

I would like to thank IFUSP and CNPQ for give me the tools and financial support during my doctoral studies.

To the latinoamerican people of IFUSP that let me discover so many things about our common culture.

To my friends.

To my wife Luisa.

To my father, my mom, my sister, my brother, my nieces ....

Resumo

A contribuição dos eventos extremos, chamados *bursts*, relacionados com estruturas coerentes que se propagam na turbulência, parece ser parte da explicação para o transporte anômalo que acontece em plasmas confinados. Porém, ainda não existe um modelo adequado no quadro da teoria neoclássica de transporte, para explicar adequadamente a contribuição destes eventos extremos. Assim, a caracterização do transporte de partículas e energia, devido a esses eventos extremos, e a sua estrutura interna, são questões relevantes no estudo do plasma de fusão. Para isso, medições locais da temperatura dos elétrons são necessárias, pois o transporte de partículas e energia sofre correções devido à temperatura. Por terem boa resolução espacial e serem relativamente fáceis de construir, as sondas eletrostáticas são comumente utilizadas em tokamaks para medir a temperatura local na região da borda de plasmas confinados magneticamente. Os métodos de varredura de tensão e a configuração de sonda tripla estão dentre os métodos mais usados para medir a temperatura local na borda do plasma com sondas eletrostáticas. Neste trabalho, é apresentada uma comparação entre as medições de temperatura usando esses dois métodos no tokamak TCABR. Para esse fim, foram utilizadas descargas de plasma em condições padrão, onde a corrente de plasma e a densidade são mantidas praticamente estáveis e há baixa atividade MHD, isto é, a fase estacionária da descarga, com os parâmetros macroscópicos de equilíbrio aproximadamente constantes. As medições da temperatura pelos dois métodos têm boa correspondência na região da sombra do limitador, mas existem discrepâncias quando as medidas são feitas dentro da coluna de plasma. Verificou-se que esta discrepância se deve ao efeito de expansão da região de transição entre o plasma e a superfície da sonda, conhecida como bainha de plasma. Portanto, foram modificadas as equações do método da sonda tripla a fim de considerar, de maneira adequada, este efeito. Esta modificação conduz a medições de temperatura compatíveis entre os dois métodos. Também se estudou as estruturas coerentes que se propagam na turbulência da borda (*bursts*), que são detectados como picos no sinal de corrente de saturação iônica. Para esse fim, foi usada a técnica da análise condicional. Os resultados obtidos parecem ser compatíveis com estruturas que apresentam uma inclinação no plano radial-poloidal. Esta inclinação implica que o método comumente usado para medir a velocidade de propagação das estruturas, baseado no atraso entre a detecção do pico entre dois pinos próximos, pode levar a resultados completamente errados. Os resultados para a evolução média da temperatura durante os *bursts* são incompatíveis entre os dois métodos. De fato, os resultados fornecidos pelo método de sonda tripla aparentam estar fisicamente errados, uma vez que indicam um alto gradiente de temperatura dentro dos *bursts*. Constatou-se que este problema é devido aos altos gradientes de potencial dentro dos *bursts* que inviabilizam a hipótese de potencial uniforme na região entre os pinos da sonda tripla.

Abstract

The contribution of the extreme events related to propagating structures in the turbulence, the so-called bursts, seems to be part of the explanation to anomalous transport in confined plasma. But, up to now, there is not an adequate model in the frame of neoclassical transport theory to properly account the contribution of these extreme events. Therefore, the characterization of the particle and energy transport due to the extreme events and the burst internal structure are an important issue in fusion plasma research. However, local electron temperature measurements are necessary to investigate those topics, because particles and energy transport have temperature corrections. Due to their good spatial resolution and relatively easy construction, electrostatic probes are often used to measure temperature in the plasma edge of tokamak. The triple probe configuration and voltage sweep technique are among the most common techniques used with electrostatic probes to measure local temperature in the plasma edge. We present a comparison between the temperature measurement using these two techniques in the tokamak TCABR. For this purpose, it was used stationary standard plasma discharges (it is, discharges with almost stable plasma current and density and with low MHD activity). For temperature measurement, the two methods have good correlation in the Scrape-Off-Layer region but there are discrepancies between their values inside the plasma column. We found that this discrepancy is due to the sheath expansion effect. Therefore, the triple probe equations were modified to properly consider this effect. The modification leads to compatible average temperature measurements between the two methods. We also studied coherent structures propagating in the edge turbulence (detected as bursts in the saturation current) by using the conditional analysis technique. The results seem to be compatibles with structures tilted in the radial-poloidal plane. This tilt implies that the common method to measure the propagation velocity using the delay time of detection between two probes, could produce wrong values. The results for the average temporal behavior of temperature during the bursts are inconsistent between the two methods. Indeed, the triple probe results seems to be physically wrong, once it indicates a strong temperature gradient inside the bursts. We found that this problem is due to the strong potential gradients inside the burst, breaking the assumption that the pins used in the triple probe configuration are in a homogeneous plasma.

List of Figures

Contents

Introduction

The *tokamak* is a device developed in the 50's in Soviet Union with the objective of creating a reactor to achieve controlled thermonuclear fusion of deuterium and tritium. After decades of investigation, an international engineering project for a prototype of nuclear reactor has been developed. This international project, called ITER (International Thermonuclear Experimental Reactor), is led by USA, EU, Russia, Japan, China, South Korea and India. ITER is being constructed in France and will establish the bases for the use of thermonuclear fusion as a real alternative for an energy source [1].The tokamak is a toroidal system that uses a poloidal magnetic field generated by the plasma current and a applied strong toroidal magnetic field to create magnetic surfaces to confine and compress the plasma. However the *anomalous transport* of energy and particles in magnetic confinement plasmas yields a characteristic confinement time one or two orders of magnitude smaller than the theoretical predictions, via neoclassical transport theory.

Experimental and theoretical developments have shown that the radial anomalous transport has origin in plasma fluctuations of density, temperature and electric and magnetic fields, that are produced by several instabilities[2]. The turbulent radial flux has a mean velocity value that is related with the $\mathbf{E} \times \mathbf{B}$ drift velocity where $\mathbf{E}$ is poloidal electric field and $\mathbf{B}$ the toroidal magnetic field. Besides the small-scale turbulent fluctuations, there are also large-scale fluctuations, the so-called bursts, which are*coherent structures* that extend for meters along magnetic field lines, but instead extend just a few centimeters in the perpendicular direction [3]. The bursts propagate in the radial direction across the scrape-off-layer, leaving the plasma column producing losses of energy and particles. Therefore the study of structure, propagation and the formation of these structures is important to understand and control the losses in confinement devices as the tokamak.

There are several diagnostics to study turbulence, one of the most common diagnostics used to measure turbulent fluctuations is the *electrostatic probes*, also known as *Langmuir probe.* This diagnostic consists of a piece of metal that is immersed in the plasma and is used in different configurations. Depending on the used configuration, the electrostatic probes can provide spatial or time resolution at the edge and near the edge regions outside the plasma column to measure *temperature*, *electric field* (calculated in general as the difference of two plasma potentials) and *density* [4]. There are two widely used techniques that involve electrostatic probes to measure temperature: the *potential sweep* [5] and the *triple probe* [6]. In the potential sweep method, a voltage source generates an oscillating signal which is applied to bias a single electrostatic probe. The applied potential and the generated current in each time are registered and with those data the characteristic response curve in the voltage-current plane is constructed. Then, this curve is fitted by using a known phenomenological function that depends on the temperature, saturation current (proportional to density) and fluctuation potential (related to plasma potential). In the triple probe configuration, a fixed potential is applied between two pins and a third is left fluctuating. The potentials in the pins are measured and a relation between them gives the temperature value.

In this work, results of the measurements with the triple probe and the potential sweep techniques are presented. It is shown for the potential sweep method that is needed to take into account the effect of the expansion of the sheath around the electrostatic probe caused when a bias potential is applied to the probe. Therefore, a correction for the triple probe technique based on the sheath expansion was proposed and tested. The tests show that this correction is necessary to avoid the overestimation of the temperature obtained by the usual triple probe technique. It was also found that this overestimation is stronger inside the plasma column.

We also present the results of the application of the above mentioned techniques to the study of coherent structures. We calculated the probability density function (PDF), and using the *conditional analysis* [7] are calculated the mean profile of the temperature, fluctuating potential and saturation current, electron density and plasma potential. It is shown for the triple probe technique, that due to the spatial distribution of the array, each pin is placed in a different part of the internal structure of coherent structures. This spatial distribution gives an inaccurate result for the temperature because it breaks the hypothesis considered in the triple probe method about the homogeneity of the plasma.

Firstly, the text presents an introduction to plasma and nuclear fusion in the chapter 1. Chapter 2 presents a brief review of the more important facts about the coherent structures and transport. Then, the theory of the electrostatic probe and measurement techniques is presented Chapter 3. Chapter 4 shows the results for the measurements with the triple probe and potential sweep technique, and a comparison between them is presented. Chapter 5 presents the results obtained from the study of coherent structures, and the use of the conditional analysis to get detailed information about these structures. Chapter 6 presents a conclusion from the obtained results and the perspectives to the future work. presented.

Chapter 1

Plasma and Fusion

Although not be present in everyday life (with a few exceptions, such as in lightning bolt, neon or fluorescent light, some PC screen), at least 99% of the universe is plasma: the stars and nebulae have is component matter in the plasma state. The fact that explain that uncommonness of plasma on earth surface is the Saha equation [8]

$$\left(\frac{n_i}{n_n}\right)^2 = 2.4 \times 10^{15} \frac{T^{3/2}}{n_n} \exp\left(\frac{-U_i}{k_B T}\right) \tag{1.1}$$

where n_i and n_n are the volumetric number density of ionized and neutral atoms in cm^{-3}, T is the temperature of the gas in Kelvins, $k_B \approx 8.617 \times 10^{-5}\mathrm{eV/K}$ is the Boltzmann constant and U_i is the ionization energy in ergs. Using the values of normal conditions on the surface of the earth, that is $T \approx 300\mathrm{K}$, $n_n \approx 3 \times 10^{19}\ \mathrm{cm}^{-3}$ and using the ionization energy of the nitrogen 14.5eV (78% of the atmospheric composition) the result is that for each ionized atom there are 10^{122} neutral atoms. Therefore, a very low percentage of particles in the air are ionized, then the plasma phenomena are not appreciable under normal conditions on earth surface, on the contrary, in the corona of the sun by each ionized atom there are 10^{-18} neutral atoms.

The study of plasma physics encompasses from the stars creation and evolution to materials science, but one of the main interests in plasma study is the application of generation of energy by nuclear fusion, following the same nuclear process that occurs in stars. The interest resides on the promise of low pollution produced in the process and inexhaustible fuel.

1.1 Definition of plasma

Following Chen [8], the definition of plasma is:

"A plasma is a *quasi-neutral* gas of charged and neutral particles which exhibits *collective behaviour*"

therefore, in this definition we have two important concepts, quasi-neutral and collective behavior. In a neutral gas, the particles interact just via collisions, but if the particles in a gas are charged, a new form of interaction appears. Charge accumulations and current create electric and magnetic fields. Then the electromagnetic interactions made that behavior of the particles in one given position depends on particles at long distance regions. Because of this *collective behavior* new phenomena appears in plasma.

Due to free charges in the plasma, any charge accumulation tends to be shielded. But the thermal energy causes an imperfect shield, forming a region with partial shielding (the charge is only screened), till the region where the thermal energy and electric potential energy equals. The radius of this region is known as Debye length λ_D. This characteristic shielding makes the plasma *quasi-neutral.*

To calculate the approximated value of the Debye length let suppose the following model. A transparent grid held at potential ϕ_0, let the ratio between electrons and ions mass be zero and that the ions are glued to an immobile background and electrons have a Maxwellian distribution function

$$n_e = n_\infty \exp\left(\frac{e\phi}{k_B T_e}\right) \tag{1.2}$$

where n_∞ is the background plasma density.

To derive the electric potential we use the Poisson's equation

$$\nabla^2\phi = \frac{d^2\phi}{dx^2} = -4\pi e(n_i - n_e) \tag{1.3}$$

where we have assume an one-dimensional variation of the potential. Using in the Poisson's equation, the maxwellian distribution for the electrons from equation 1.2 and using the fact that the thermal energy inside the non shielded region is stronger than the electric potential we expand in Taylor's series, then:

$$\frac{d^2\phi}{dx^2} = 4\pi e n_\infty \left[\frac{e\phi}{k_B T_e} + \left(\frac{1}{2} \frac{e\phi}{k_B T_e} \right)^2 \right] \tag{1.4}$$

retaining only the linear term we have the following differential equation

$$\frac{d^2\phi}{dx^2} = \frac{4\pi n_\infty e^2}{k_B T_e} \phi \tag{1.5}$$

This equation has a solution given by

$$\phi = \phi_0 \exp\left(-\frac{|x|}{\lambda_D} \right) \tag{1.6}$$

where λ_D is the so-called Debye length

$$\lambda_D = \sqrt{\frac{k_B T_e}{4\pi n e^2}} \tag{1.7}$$

With the definition of Debye length it is possible to define the conditions to apply the plasma physics equations. Because of quasi-neutrality condition the characteristic length L of the system needs to be much greater than the Debye's length, then

$$L \gg \lambda_D \tag{1.8}$$

The validity of the shielding as statistical concept requires a sufficient quantity of particles for the screening purpose. Then defining the number of particles in a "Debye's sphere" as

$$N_D = n \frac{4}{3} \pi \lambda_D^3 \tag{1.9}$$

then we need the next condition

$$N_D \gg 1 \tag{1.10}$$

Finally due to the free charges in the plasma, any disturbance of the electric field induces a plasma response moving free charges neutralizing the field. In the plasma, the charge distribution perturbation is produced by the phenomena of thermal collisions. Then if ω is the frequency of a typical plasma oscilation and τ the mean colission time with neutral atoms, an important condition which ensures that the plasma behavior is mainly dominated by electromagnetic effects is:

$$\omega\tau \gg 1 \tag{1.11}$$

if not, the electromagnetic effects are irrelevant since plasma dynamics will be dominated by collisions as in the case of a neutral fluid. Then to be a plasma the gas we have to fulfill the conditions of equations 1.8, 1.10 and eq 1.11.

1.2 Nuclear fusion

The nuclear fusion aims the production of energy from nuclear reactions. In this kind of process an amount of matter becomes energy, the amount determined by the Einstein equation. Therefore if we have

$$A + B \rightarrow C + D \tag{1.12}$$

and the process is of the form

$$(m_A + m_b)c^2 > (m_C + m_D)c^2 \tag{1.13}$$

there will be a quantity of energy released.

In the case of the fusion reaction, the more interesting reaction for future use in energy production is

$$\mathrm{D}^2 + \mathrm{T}^3 \rightarrow \mathrm{He}^4(3.5\mathrm{MeV}) + \mathrm{n}(14.1\mathrm{MeV}) \tag{1.14}$$

where the initial matters are deuterium (D^2) and tritium (T^3), on the other hand the products of the reaction are charged α particles (He^4) confined by a magnetic field and could be reused for heating the plasma, and a neutron of high energy that can not be confined but can be trapped in a surrounding blanket of $\mathrm{Li}^6/\mathrm{Li}^7$ that is heated by the neutrons making possible obtain energy. In the process there will breeding T^3 for new fusions.

The initial combustible for the reaction can be obtained from the ocean water. In the ocean there are 6500 molecules of normal water for every molecule of deuterium. Because of that, it is usual in Plasma community to say that the deuterium in one liter of water can be used to produce near of 10^{10} J of energy, compared with 3×10^7 produced by one liter of fossil fuel like gasoline. But in order to obtain this class of reaction for energy production, we need calculate the power balance to know the conditions to achieve the fusion, that is, the energy produced and lost in the plasma. First, we have the energy produced by thermonuclear process

$$P_T = \frac{1}{4} n^2 \left\langle \sigma v \right\rangle E_T, \quad E_T \approx 22.4\mathrm{MeV} \tag{1.15}$$

where n is the plasma density, $\langle \sigma \nu \rangle$ is the average nuclear reaction rate with σ the cross-section of the D-T reactions and v the relative speed of the nuclei, and E_T is the average energy released in the D-T reaction.

A second term is the power loss caused by Bremsstrahlung, i.e. deceleration of the ions and electrons by collisions. The equation of this loss has the form

$$P_B = \alpha n^2 \tilde{T}^{1/2}, \quad \alpha = 3.8 \times 10^{-29} \mathrm{J}^{1/2} \mathrm{m}^3 \mathrm{s}^{-1} \tag{1.16}$$

Finally, a third term takes into account the loss caused by heat transport through the plasma which is described by

$$P_L = \frac{3n\tilde{T}}{\tau_E} \tag{1.17}$$

where $3n\tilde{T}$ is the kinetic energy of electrons and ions and τ_E is the confinement time which is influenced by anomalous transport [9] .

Now, to calculate the transport is used the Lawson criterion [10] that involves the power balance as

$$P_B + P_L = \eta(P_T + P_B + P_L) \tag{1.18}$$

where η is the efficiency to convert the wall heath into usable energy: 1/3 for an original Lawson criteria and $\eta \approx 0.135$ in a more modern approach [11]. The left terms represent the lost power and the right terms the power generated in the plasma. Then using equations 1.15, 1.16 and 1.17 in the power balance equation, we have the relation

$$n\tau_E = \frac{3\tilde{T}}{\frac{\eta}{1-\eta} f\left(\tilde{T}\right) - \alpha\tilde{T}^{1/2}} \tag{1.19}$$

then, from this equation the parameters to achieve fusion are obtained. The values of the parameters are presented in the Table 1.1.

Temperature T	10^8 K (10KeV)
Particle density n	10^{21}m^{-3}
Power density	10MWm^{-3}
Time scale τ	100s

Table 1.1: Parameter approximated for obtain reliable energy from nuclear fusion in plasma. The values are taking from reference [11].

1.3 Plasma confinement

As it can be seen in table 1.1, the nuclear fusion requires a high temperature and a high density of the plasma for a relatively long time, this conditions can destroy any known material. Therefore, the technical problem of the plasma confinement arises. The solution considered in this work is the magnetic confinement, however, there are other ways to contour the problem, for example inertial confinement [12].

Although exist several ways to reach the magnetic confinement as stellarator, reverse field pinch or magnetic mirror, the more promising way to get fusion is the *tokamak*[1]. The theoretical concept of tokamak was formulated by I. E. Tamm and A. D. Shafranov in 1950 and was implemented in the Kurchatov institute in 1951 [13]. Since this first experiment the technology of the tokamak has evolved it performance several orders of magnitude, this development is expected to be enhanced in the ITER, achieving the required parameters for the first fusion ignition as shown in figure 1.1. The ITER is an international effort to obtain sustainable plasma confinement at the fusion parameters for energy production, this scientific collaboration involved China, the European Union, India, Japan, Russia, South Korea and the United States. The first plasma was scheduled to 2025 although this date is reevaluated due to bureaucratic and technical issues.

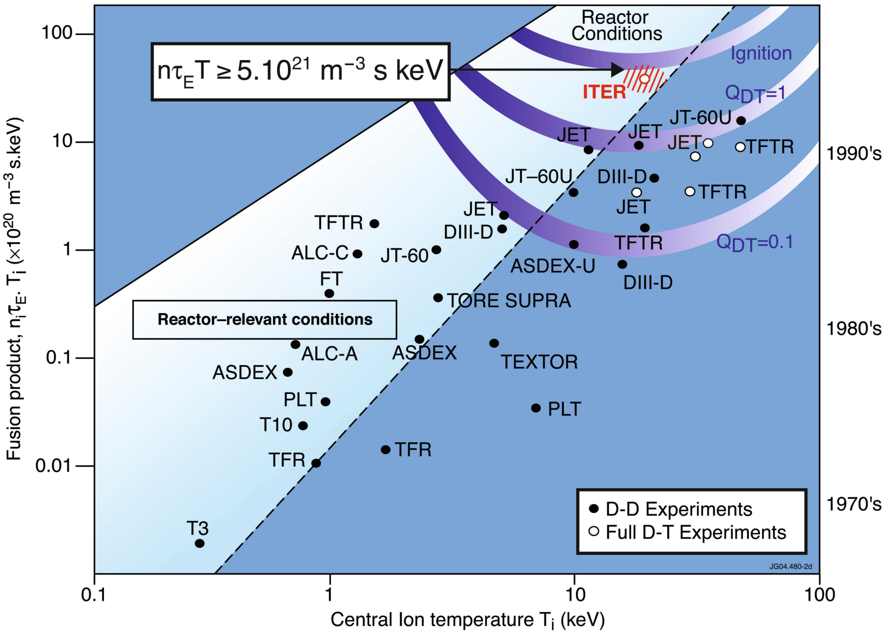

Figure 1.1: Evolution of the tokamak performance to achieve the ignition conditions [14].

The main idea of the tokamak is crudely speaking a combination two configurations to obtain plasma confinement, the z-pinch and the θ-pinch, both cylindrical devices, as shown in Figure 1.2. The z-pinch is made by creating a current in the axial direction of the plasma column, then a magnetic field in the poloidal direction is generated (figure 1.2). Due to Lorentz force $\mathbf{j} \times \mathbf{B} = -j_z B_\theta \mathbf{e}_r$, a force in the

---

[1] The word tokamak is a transliteration of the Russian word токамак, an acronym of “тороидальная камера с магнитными катушками” (toroidal'naya kamera s magnitnymi katushkami) - toroidal chamber with magnetic coils.

inward radial direction compresses the plasma. The problem is that equilibrium is so fragile, the plasma blows up in the time scale of μs. Another configurations for magnetic confinement is the θ-pinch shown in figure 1.2. In this case a current in the poloidal direction is generated, then an axial magnetic field is produced. Therefore, by Lorentz force a pressure in the inward radial direction is produced as in θ-pinch. However this type of configuration has instabilities that blow up the plasma in the time scale of μs. In addition to the instability of those confinement approaches, due to the open endings there is an important particles loss.

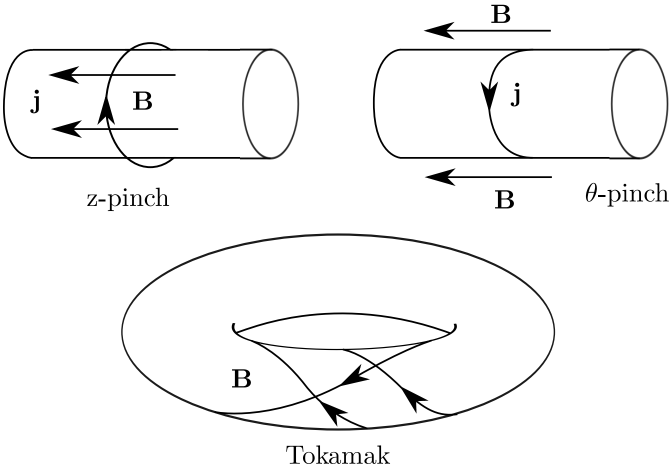

Figure 1.2: z-pinch, θ-pinch and the mixture of the two ideas, the tokamak [11]

In the tokamak the two fields toroidal and poloidal are added to create a bend total field on the toroidal surfaces, leading to a more stable configuration. To obtain this magnetic configuration the device is constructed in the way shown in figure 1.3. The toroidal magnetic field B_{tor} is produced by an external array of coils along the toroid. A toroidal plasma current generate the poloidal magnetic field B_{pol}, becoming the plasma the secondary coil of a transformer taking advance of the plasma conductivity. The toroidal component of the field is larger than poloidal for stability issues.

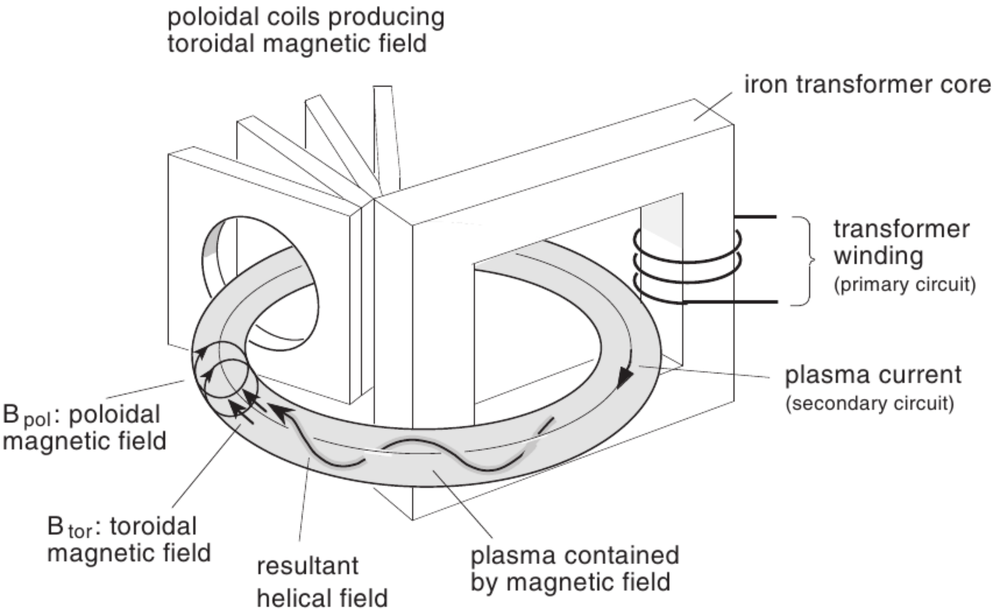

Figure 1.3: Practical implementation of the tokamak configuration. A transformer is used to generate the plasma current that generates the poloidal magnetic field B_{pol} and the poloidal coils produce the toroidal magnetic field B_{tor}. [11]

Since the 80's one important topic of research in magnetic confinement is the plasma column edge physics, due to the turbulence and it influence on the transport of energy and particles [15] [16]. This edge loses decrease the confinement time much more than was expected by the first theoretical attempts to describe the the transport. Those approached only consider collisional effects in cylindrical (classical theory) and toroidal (neoclassical theory) configurations, not the turbulence which dominates the dynamics of the plasma edge.

1.4 The TCBAR tokamak

The Tokamak Chauffage Alfvén Brésilien or TCABR was designed and constructed at Ecole Politechnique de Lausanne/Switzerland with the main objective of study the plasma column heating using Alfvén waves. After several years of investigation, the tokamak was transferred to Brazil. The basic parameters of the TCABR are presented in the table 1.2

Table 1.2: TCABR tokamak characteristics.

Parameter	Symbol	Value
Major radius	R_0	0.61m
Minor radius	a	0.18m
Plasma current	I_P	120kA
Discharge time	T_D	120ms
Central electrons temperature	T_e	500eV
Central electrons density	n_e	$6\times10^{19}\mathrm{m}^{-3}$
Toroidal magnetic field	B_ϕ	1.07 T

An interesting characteristic of the TCABR tokamak is that, due to the relatively low energy flux in the edge region of the plasma column, it is possible to study the turbulence with electrostatic probes without destroying the pins due to the low density and temperature compared with another machines. The use of electrostatic probes to study the turbulence in the column edge in the TCABR tokamak has been done in previous works related to particle transport, [17], fluctuations of plasma parameters [18, 19, 20], turbulence with MHD activity [21, 22, 23] and vorticity measurements [24]. In our work is introduced the conditional analysis as a the technique to characterize the turbulence in TCABR tokamak.

Chapter 2

Transport and Coherent structures

2.1 Turbulent transport

Transport of energy and particles in plasma, also simply called *transport* has been investigated since the beginning of the research on fusion. An initial theoretical attempt used only the cylindrical geometry and the diffusion phenomena to obtain the particles and energy transport in confined plasmas, this is the so-called *classical transport* [25]. However, the experimental measurements made, showed a discrepancy between experimental and theoretical calculations for the *radial transport* by roughly two orders of magnitude. The discrepancy led to develop the *neoclassical transport* where the toroidal geometry is taken into consideration. This new calculation enhanced the theoretical transport values, but it not yet explain satisfactorily the measurements[26].

In 1976 Mazzucato showed experimentally that there are small scale turbulent fluctuations in the electron density of the plasma [27]. After this discovery, the *anomalous transport*, i.e. the transport that is not explained by neoclassical transport theory, begun to be attributed to the microscopic plasma turbulence. This plasma turbulence is introduced in terms of large fluctuations in plasma parameters as potential, density, temperature, magnetic field, etc. The fact that fluctuations are included in the calculations of plasma transport is a complete break with the neoclassical theory.

On the edge of the plasma, the fluctuations are broadband with range $f \backsim 10kHz - 100kHz$, as shown for different confined plasmas in Figure 2.1.a. For plasma density, the fluctuations amplitude is very large, $\delta n/n \backsim 5 - 100\%$, which typically increases with the radial position. Similar levels of amplitude fluctuations are measured for the electron temperature and plasma potential. On the other hand, for the magnetic field the amplitude of the fluctuations is smaller. As an example, in Figure 2.1.b the amplitude of some fluctuations are shown for the TEXTOR tokamak. The size scale, range $\backsim$ 0.1 – 10 cm in the perpendicular direction to the magnetic field lines. However, in the direction parallel to the magnetic field lines, the scale is of the order of meters, therefore the turbulent structures are nearly 2D [28].

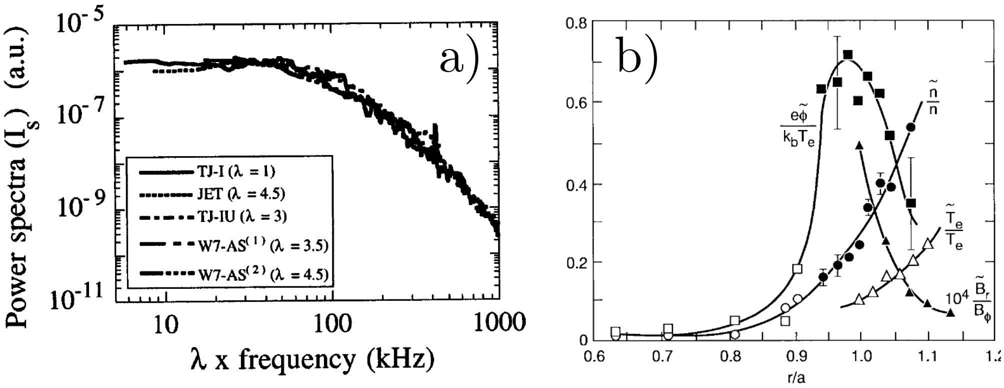

Figure 2.1: a) Frequency spectra for saturation current fluctuations in several tokamaks [29]. b) Amplitude fluctuations in the electron temperature, density and magnetic field in TEXTOR tokamak [2, 30].

From the theoretical point of view, for the turbulent fluctuations, the radial transport of energy and particles are calculated as [31]:

Particle flux

$$\Gamma_j^f = \Gamma_j^{f,E} + \Gamma_j^{f,b} \tag{2.1}$$

$$\Gamma_j^{f,E} = \frac{\left\langle \tilde{E}_\theta \tilde{n}_j \right\rangle}{B_\phi} \tag{2.2}$$

$$\Gamma_j^{f,b} = -\frac{\left\langle \tilde{j}_{\parallel j} \tilde{b}_r \right\rangle}{eB_\phi} = g_1 \frac{\tilde{b}_r}{B_\phi} \tag{2.3}$$

Energy flux

$$Q_j^f = Q_j^{f,E} + Q_j^{f,b} \tag{2.4}$$

$$Q_j^{f,E} = \frac{3}{2} k_b n \frac{\left\langle \tilde{E}_\theta \tilde{T}_j \right\rangle}{B_\phi} + \frac{3}{2} k_b T_j \frac{\left\langle \tilde{E}_\theta \tilde{n}_j \right\rangle}{B_\phi} \tag{2.5}$$

$$Q_j^{f,b} = g_{2j} \nabla T_j \frac{\tilde{b}_r}{B_p hi} \tag{2.6}$$

where $\tilde{E}$, $\tilde{n}$, $\tilde{T}$, $\tilde{b}$, $\tilde{j}$ are respectively the fluctuating parts of the electric field, density, temperature, magnetic field and current density. The subscripts r, θ, ϕ, $\|$, $\perp$ refer to directions radial, poloidal, toroidal, parallel and perpendicular to the magnetic field, $\langle ... \rangle$ denotes average and k_B the Boltzmann's constant. Typically the value of the term $g_1(\tilde{b}_r/B_\phi)$ is small, therefore, the magnetic fluctuations are negligible for the transport of particles. For electrons $g_{2e}(\tilde{b}_r/B_\phi) \approx \pi R v_{the} (\tilde{b}_r/B_\phi)^2$ for collisionless plasma, where v_{the} is the thermal velocity and R the plasma column major radius. In the collisional case $g_{2e}(\tilde{b}_r/B_\phi) \approx \chi_{e\|} (\tilde{b}_r/B_\phi)^2$ with $\chi_{e\|}$ the classical parallel electron thermal diffusivity.

The anomalous transport is of practical importance for plasma fusion technology because it implies that energy and particles reach the chamber walls at higher rates that expected, as shown in reference [32]. Therefore, when the particles collide with the wall generates an impurities flux into the plasma and degrade the wall material. In D-shaped tokamaks, these particles are expected to collide mainly with the divertor.

2.2 Coherent structures

As the theoretical, experimental and simulation techniques enhanced, new aspects of the anomalous transport were unveiled. One of the more important facts about the nature of the anomalous transport is that it is not only diffusive but convective too, as it was studied experimentally by Zweben in 1985 in Ref. [33]. In [34] those convective structures are discussed in the framework of the Self-Organized Critically (SOC) theory. The convective nature is also shown in different machines as tokamaks [35], stellarators [36] and Q machines[37].

One of the important accepted aspects of the anomalous transport is the existence of *coherent structures* that propagate in the edge and scrape-off-layer (SOL) [1] of the plasma. These filament structures are elongated in the direction parallel to magnetic field lines as shown in Figure 2.2

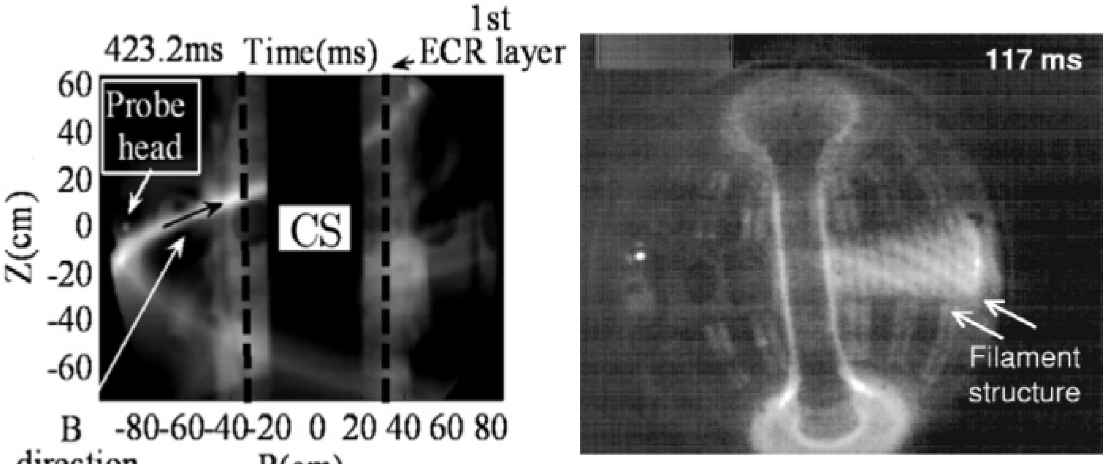

a) b)

Figure 2.2: a) Blob image taken with a fast camera in the spherical tokamak QUEST [38]. b) Blob image using the gas puff image (GPI) diagnostic in the NSTX [39]

As it is shown in Ref.[40], although, these structures correspond to only 20% of the time, the particle transport due to these structures correspond up to 60% of all the turbulent particle transport. The experimental existence of these coherent structures also called *burst* or *blobs*, are reported in several tokamaks, stellarator and other plasma devices as shown in the table II and III of Ref. [3].

Due to the presence of coherent structures, the turbulent density fluctuations have an important and common feature: their probability density function (PDF) for the local density measurements (related to the ion saturation current) is a non-Gaussian one [41]. This characteristic PDF is present in several devices and seems to be universal as show in Figure 2.3.a. The presence of the positive tail is the most important feature, because this tail indicates that the structures have higher

---

[1] The SOL is the region where the magnetic field lines are linked either with the limiter (or the divertor) and even with the chamber walls.

density values than the surrounding plasma.

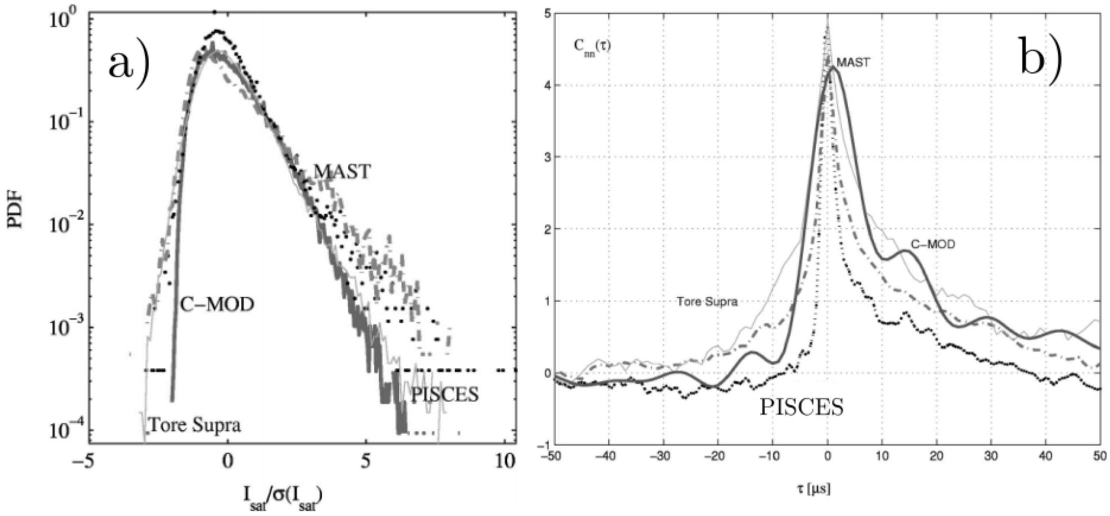

Figure 2.3: a) PDF for the saturation current normalized in terms of standard deviations, in Tore Supra (solid line), Alcator C-Mode (thick solid line), MAST (dashed-dotted line) and PISCES (dots) [41]. b) The autoconditional average in Tore Supra (solid line), Alcator C-Mod (thick solid line), MAST (dashed–dotted line), and PISCES (dots)[41].

Another known fact about the blobs is its characteristic shape. As is shown in Figure 2.3.b, there is a rapid increase of the density, then a peak value and after this peak, a slower density fall. The shape can be explained supposing a blob shape-like structure with a dense center and a less dense tail in the direction contrary to the propagation. For the electric potential, it has been measured a dipole structure for the burst in different machines [3], [35]. The dipole structure and the density peak are exemplified in Figure 2.4

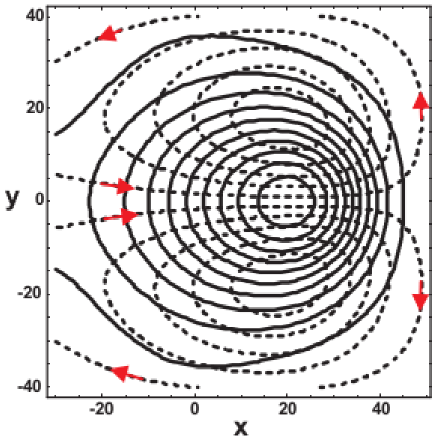

Figure 2.4: Density contours in solid lines and equipotential contours in dashed lines times [35].

With respect to the propagation mechanism, is accepted that the propagation velocity in the direction perpendicular to the magnetic field lines, depends on the poloidal electric field and the toroidal magnetic field $\mathbf{V}_r = \mathbf{E} \times \mathbf{B}/B^2$.

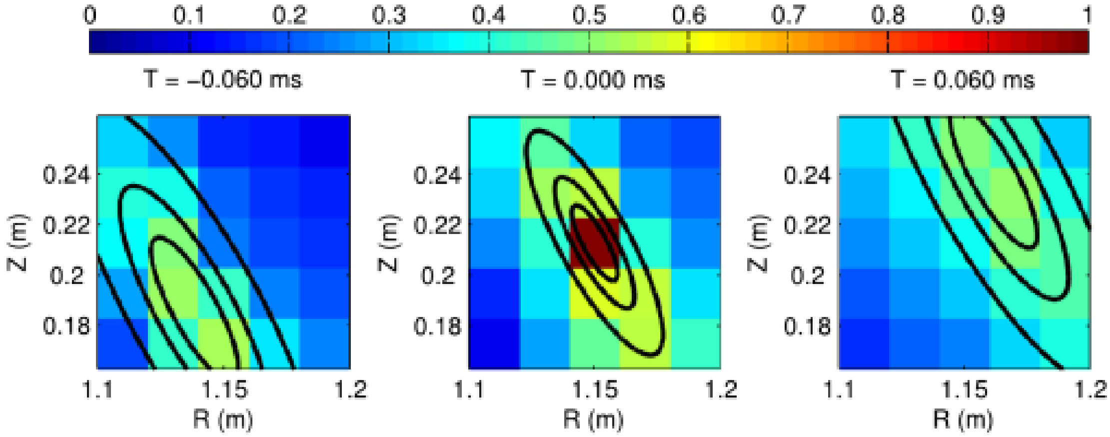

Figure 2.5: Profile for the relative amplitude for a burst in three different times[42].

More recent studies of the bursts, with a 2D probe array show an elongated and tilted shape [42] as shown in Figure 2.5. Another interesting fact is that there is not only radial but also poloidal velocity. Usually this poloidal velocity is not considered in models or simulations.

The measurement of those structures requires diagnostics with high spatial and temporal resolution. The spatial resolution need is around the size of the blob in the plane perpendicular to the magnetic file line, ∼2cm as shown in the Figure 2.6. And besides, the time resolution is due to the apparent velocity of the structures, as shown in Figure 2.6 this velocity has values around 1Km/s. Using the order of size of the structure before mentioned we have times around 20μs. Due to the above mentioned limits, not all diagnostics are suitable to perform measurements of blobs. For this reason the more commonly used diagnostic are the Langmuir probes and optic diagnostics as Gas Puff Image (GPI) and Beam Emission Spectrography (BES).

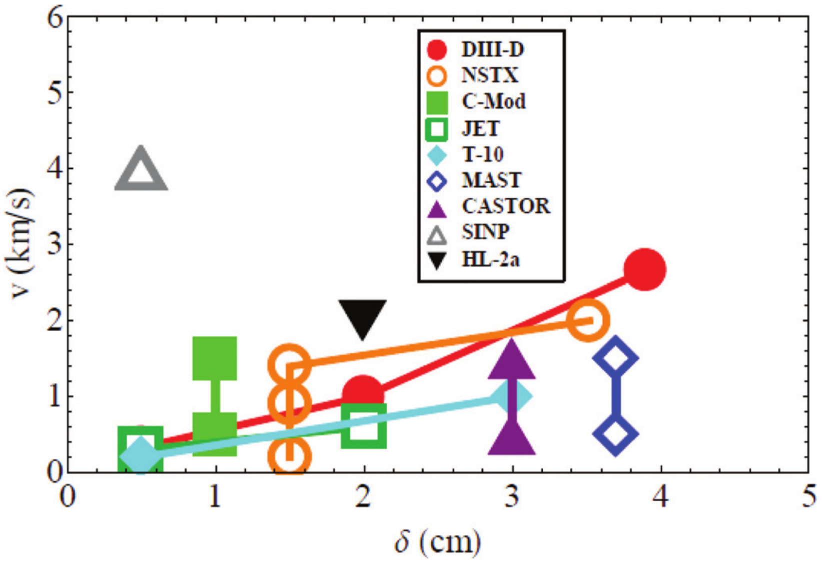

Figure 2.6: Apparent radial outward speed of the convective structures as a function of it size from data reported in different machines [3].

The mechanism that generates the blobs is yet an open question. A model proposed in Ref.[43] is based on the drift wave plasma turbulence. In this model is considered a Boltzmann distribution of electrons

$$n_e(\mathbf{r},t) = n(\mathbf{r}_\perp)\exp\left(e\phi(\mathbf{r},t)/T_e\right) \tag{2.7}$$

where the electron temperature T_e has been considered constant and $n(\mathbf{r}_\perp)$ is the density in the absence of electric potential. This model also use the continuity equation for ions

$$\frac{\partial n_i}{\partial t} + \nabla\cdot(n_i\mathbf{V})_i = 0 \tag{2.8}$$

where the *cold ion approximation* is employed for the ion velocity

$$\mathbf{V}_i = \mathbf{V}_0 - \rho_s^2\frac{d}{dt}\nabla\phi \qquad \mathbf{V}_0 = -D_B\left(\nabla\times\mathbf{b}\right) \tag{2.9}$$

where d/dt is the convective derivative, $\rho_s^2 = T_eM(c/eB)^2$, $D_B = cT_e/eB$, M is the ion mass and B the strength of the magnetic field. Then, using 2.7 and 2.9 in 2.8 we obtain

$$\mathrm{e}\frac{d\mathrm{e}^{\phi}}{dt} - \rho_s^2 \nabla \cdot \left(\mathrm{e}^{\phi} \frac{d}{dt} \nabla \phi \right) - \Lambda \mathrm{e}^{\phi} \hat{\mathbf{e}}_x \cdot \left(\mathbf{V}_0 - \rho_s^2 \frac{d}{dt} \nabla \phi \right) \tag{2.10}$$

Now, considering the case when $|\partial(...)/\partial y >> \partial(...)/\partial x|$, which implies an stream like solution, the last equation becomes

$$\frac{\partial \mathrm{e}^{\phi}}{\partial t} - \rho_s^2 \frac{\partial}{\partial y} \left(\mathrm{e}^{\phi} - \rho_s^2 \frac{\partial^2 \phi}{\partial y \partial t} \right) + U_{DW} \frac{\partial \mathrm{e}^{\phi}}{\partial y} = 0 \tag{2.11}$$

where $U_{DW} \equiv \Lambda D_B$ is the phase velocity of the linear drift waves when the long wavelength approximation is used. Considering traveling wave solutions for equation 2.11. This is, solutionts that satisfy $\partial(...)/\partial t = -U_{NLE} \partial(...)/\partial y$, we get

$$\kappa_{NLE}^2 \frac{de^{\phi}}{dy} + \frac{d}{dy} \left(e^{\phi} \frac{d^2 \phi}{dy^2} \right) = 0 \tag{2.12}$$

where $\kappa_{NLE}^2 = \rho_s^{-2} (U_{DW}/U_{NLE} - 1)$

It can be show that the equation 2.12 has an approximate solution of the form [43]

$$\exp \phi_{max} \approx 2 \sqrt{-\frac{\alpha}{\pi} \ln \hat{C}} \tag{2.13}$$

where ϕ_{max} is the maximum potential value for which there is a solution, with the constants $\hat{C}$ and $\alpha > 1$. Using the fact that $e^{\phi} \approx n$ implies $e^{\phi_{max}} \approx n_{blob}$ and considering $\left\langle e^{\phi_{max}} \right\rangle = 1$, then, the next relation for densities is obtained

$$\frac{n_{blob}}{< n_e >} \approx 2 \sqrt{-\frac{\alpha}{\pi} \ln \hat{C}} \tag{2.14}$$

.

Using the values $\hat{C} = 0.1$ and $\alpha = 3$, the density of the blob is about 3 times the density of the surrounding plasma. Besides, it can be shown that the *mean distance* between two blobs is [43]

$$L_2 \approx 2^{3/2} \frac{\sqrt{-\alpha \ln \hat{C}}}{\kappa_{NLE}} \tag{2.15}$$

and the effective size of the blob is

$$\delta_b \approx \frac{\left[2^{3/2}\ln\left(2\sqrt{-(\alpha/\pi)\ln(\hat{C})}\right)\right]^{1/2}}{\kappa_{NLE}} \tag{2.16}$$

then, the relation between the size of the blob and the mean distance between two blobs can be calculated and has the next value:

$$\frac{L_2}{\delta_b} \approx 5 \tag{2.17}$$

.

The relations 2.14 and 2.17 imply an important characteristics of the blobs: they are isolated structures with it density higher than the surrounding plasma.

Due to nonlinearity of the equations used to model the plasma turbulence, an important part of the theoretical work is done in simulation, studying principally the movement of the blobs across the SOL.

An accepted basic model of burst propagation was proposed in Ref.[44]. In this model, the drift $\nabla\mathbf{B}$ cause a polarization that generates a current along the magnetic lines that ends in the divertor or limiter, those currents was measured in Ref. [45]. The polarization creates an electrostatic potential ϕ and an electric field $\mathbf{E}$, perpendicular to $\mathbf{B}$ but constant along $\mathbf{B}$, this electrostatic potential causes an $\mathbf{E}\times\mathbf{B}$ velocity drift of the burst. This model is presented in Figure 2.7

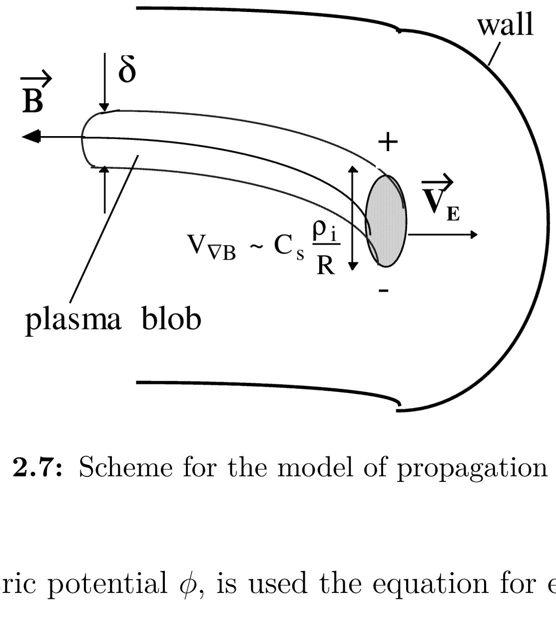

Figure 2.7: Scheme for the model of propagation of blobs.

To find the electric potential ϕ, is used the equation for electric current

$$\nabla \mathbf{j}_{\perp} + \nabla \mathbf{j}_{\parallel} = 0 \tag{2.18}$$

with

$$\mathbf{j}_{\perp} = c\frac{\mathbf{B} \times \nabla P}{\mathbf{B}^2} \tag{2.19}$$

where the pressure is given by $P = nT$. Then, by using the blob plasma continuity equation, the radial burst velocity due to $\mathbf{E} \times \mathbf{B}$ drift is obtained

$$V_b = C_s \left(\frac{\rho_i}{\delta}\right) \frac{l_b}{R} \frac{n_b}{n_t} \tag{2.20}$$

where C_S is the plasma sound speed, ρ_i the ion gyro-radius, δ the blob size in the poloidal direction, l_b the size of blob in the magnetic field direction, R the major tokamak radius, n_b the burst density and n_t the density of the plasma. Taking the life time due to the parallel plasma flow as $\tau_b \sim l_b/C_S$, the mean size of the burst is obtained as

$$\delta < \delta_{max} = R\left[\left(\frac{q\rho_i}{R}\right)^2 \frac{n_b}{n_t}\right]^{1/3} \tag{2.21}$$

where q is the safety factor.

Due to difficulty involved in solve the equations caused by the nonlinearity, several codes has been used to simulate the blobs. In references [46], [47] and [48], the propagation of blobs in the SOL is simulated, but the blobs are seeded at the begin of the simulation. In Ref. [49] a comparison is performed between several codes. All the codes show basic features of blobs as density peak, dipole electric fled.

An interesting simulation is presented in Ref.[50] where the aim is the production of burst. As it is shown in the Figure 2.8 there is a density and temperature peak as appears in the graphics for the density n and temperature T. In the graphic for the potential ϕ for the burst there is a dipole structure.

The conditional analysis is used in the results obtained in Ref.[50], where an electrostatic probe model is included in the simulation. This analysis is performed for the temperature of electrons and ions, the electric potential and the density. The result of this analysis is presented in the Figure 2.9. There are clear peaks at the moment of the burst, indicating that those structures are more dense and hot that the surrounding plasma. This result implies a convective transport of energy and particles driven by those coherent structures.

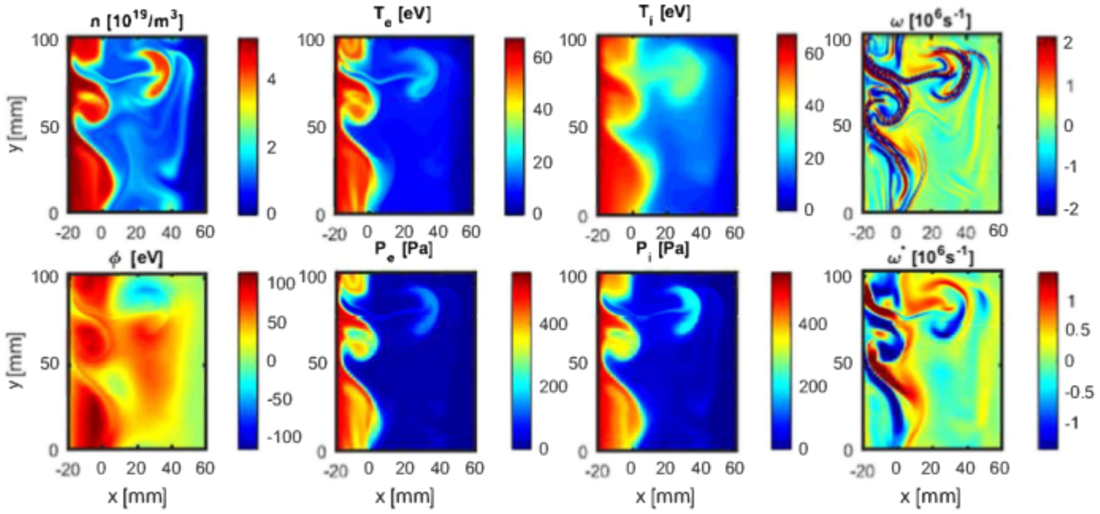

Figure 2.8: Result of the simulation of the burst for the density, electron and ion temperature, electric potential, pressure of ions and electrons and vorticity [50]

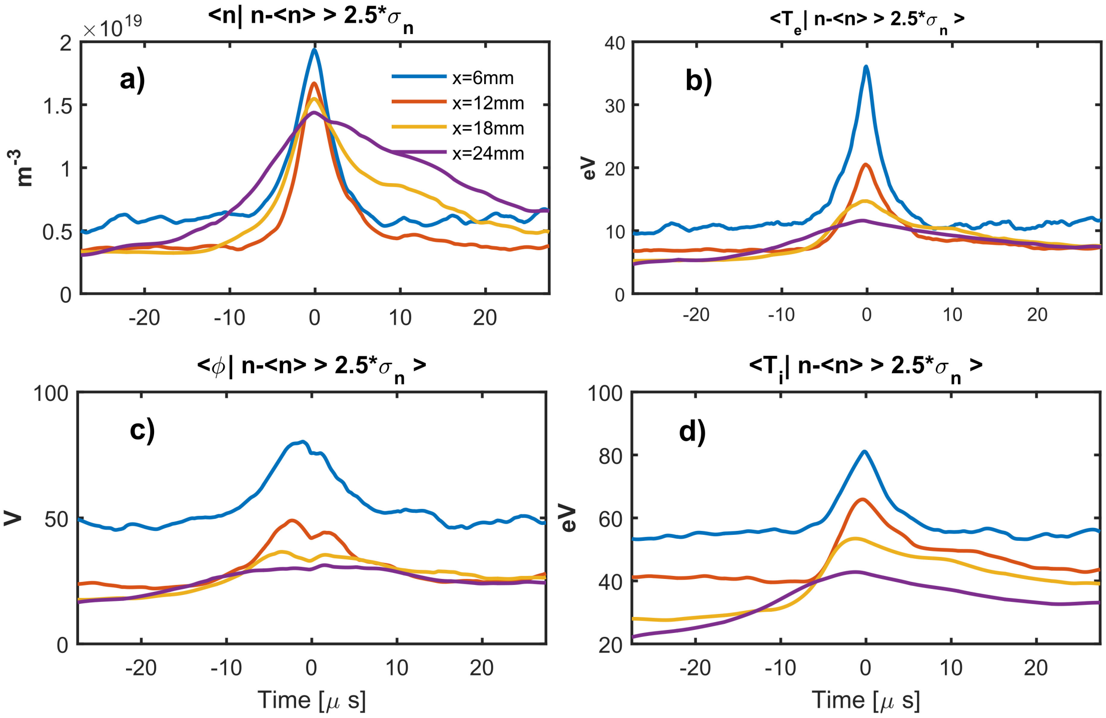

Figure 2.9: Results of the conditional analysis performed for the signals of density, potential, and temperature of ions and electrons [50].

Chapter 3

Electrostatic probes and temperature measuremet

This chapter presents the theoretical and experimental facts about the temperature measurement, and the analysis techniques. Firstly, it is presented a basic theory of electrostatic probes and its uses as a diagnostic for measurement of the temperature, density and plasma potential. Then, in the final part of the chapter, the conditional analysis technique is explained.

3.1 Electrostatic probe

Due to the high temperatures involved in fusion plasmas, even in the edge and SOL regions, several methods have been developed to measure temperature. One of the most used techniques is the so-called *Langmuir probes* or *electrostatic probes*, used in plasma since the first decades of the XIX century. This technique consist basically in measure the current and potential response of a metallic piece inside the plasma.

3.1.1 Plasma sheath

When a piece of material is immersed in the plasma, a layer appears around that piece. This phenomenon is produced by the difference of the ions and electrons fluxes due to different mobilities, forcing the surface of the material to reach a negative potential with respect to plasma. This layer, known as *plasma sheath* has an extension of the order of the Debye length λ_D. This plasma sheath is used as a base for an experimental diagnostic tool so-called the *electrostatic probe* or *Langmuir probe.* In this section we will calculate, in an approximated way, following the Ref.[51], the potential on the material surface, the variation of the density and potential into the sheath, and a theoretical expression that shows the use of the plasma probe to measure the local density, potential and temperature of the plasma.

Basic ideas of the model

The basic idea of the physic phenomenon is that, when plasma particles collide with the material, the ions recombine or return to the plasma, meanwhile, the electrons recombine or enter into the conduction band if the material surface is a metal. Let us suppose that the particles have an isotropic distribution; in this case it follows from statistical mechanics that the number of particles that hit the surface by time is given by

$$\Gamma_\alpha = \frac{n_\alpha < v >_\alpha}{4} \tag{3.1}$$

where α indicates the specie of particles that could be electrons or ions, n_α the density, v the particle's velocity and the $<>$ the average value. If we assume that the distributions of the particles are of Maxwell-Boltzmann type , the mean velocity is given by

$$< v >_\alpha = \left(\frac{8}{\pi}\right)^{1/2} \left(\frac{kT_\alpha}{m_\alpha}\right)^{\frac{1}{2}} \tag{3.2}$$

where m_α and T_α are the mass and temperature of the α type particles, and k the Boltzmann constant. So, we have that the particle flux is given by

$$\Gamma_\alpha = n_\alpha \left(\frac{kT_\alpha}{2\pi m_\alpha}\right)^{\frac{1}{2}} \tag{3.3}$$

An important fact appears in this equation; for the same temperature and density, the flux depend on the inverse of the mass. For this reason, the flux of electrons is larger than the ions one. Therefore, there is a net accumulation of negative charges on the metal surface, as a consequence, the negative potential rise the flux of ions. This process stops at a potential when the two flux cancel, reaching a dynamical equilibrium.

Electric potential on the metal surface

When the plasma sheath is created, we assume the following boundary conditions for the potential

$$\phi(x) = \begin{cases} \phi_w & \text{if} \quad x = 0 \\ 0 & \text{if} \quad x = \infty \end{cases} \tag{3.4}$$

where the reference potential is chosen as the potential inside the plasma. Using again the results from statistical mechanics, we have that the densities of the ions and electrons are [1]

$$\begin{aligned} n_e(\boldsymbol{r}) &= n_0 \exp\left[\frac{e\phi(\boldsymbol{r})}{kT}\right] \\ n_i(\boldsymbol{r}) &= n_0 \exp\left[\frac{-e\phi(\boldsymbol{r})}{kT}\right] \end{aligned} \tag{3.5}$$

At dynamical equilibrium, there is no more accumulation of charge; then the flux of ions and electrons have to balance

$$\Gamma_e(0) = \Gamma_i(0) \tag{3.6}$$

Using the equations (3.1) and (3.5) and solving for the metal surface potential, we obtain

$$\phi_w = -\left(\frac{kT}{4e}\right) \ln\left(\frac{m_i}{m_e}\right) \tag{3.7}$$

Rewriting the equation 3.7 as

---

[1] At this point is neglected the drift velocity of the particles towards the metal surface, this drift will be taken into account with the hydrodynamic equations in the study of the inner structure of the sheath.

$$\frac{|e\phi_w|}{kT} = \frac{1}{4}\ln\left(\frac{m_i}{m_e}\right) \tag{3.8}$$

it is seen that the thermal and potential energy are of the same order, for example, in the case of Hydrogen plasma the potential energy is only twice the thermal energy.

Inner structure of the plasma sheath

Continuing the study of the inner structure of the plasma sheath, we write the conservation equations for particles and moment

$$\frac{dn_\alpha u_\alpha}{dx} = n_\alpha \frac{du_\alpha}{dx} + u_\alpha \frac{n_\alpha}{dx} = 0 \tag{3.9}$$

$$m_\alpha u_\alpha \frac{du_\alpha}{dx} = -\frac{k_B T_\alpha}{n_\alpha}\frac{dn_\alpha}{dx} - q_\alpha \frac{d\phi}{dx} = 0 \tag{3.10}$$

where u is the velocity, m the mass, q the electric charge, T the temperature and k_B the Boltzmann's constant. In the particle conservation equation (3.9), we use the fact that, when the sheath is generated, the system is in dynamical equilibrium as in (3.6). In the case of the momentum conservation equation (3.10), the ideal gas behavior is assumed, and are neglected collisions and magnetic fields. Now, as the ions have a large mass compared with the electrons, we assume that their thermal energy is low. For the electrons, because of its low mass, the kinetic energy is low; then it is valid the assumption that

$$m_e u_e^2 << k_B T << m_i u_i^2 \tag{3.11}$$

Using this approximation in (3.9) and (3.10) we obtain

$$\frac{k_B T_e}{n_e}\frac{dn_e}{dx} - e\frac{d\phi}{dx} = 0 \tag{3.12}$$

$$m_i u_i \frac{du_i}{dx} + e\frac{d\phi}{dx} = 0 \tag{3.13}$$

Solving the equation 3.12 using the boundary conditions $n = n_0$ when $\phi = 0$, we have

$$n_e(x) = n_0 \exp\left[\frac{e\phi(x)}{k_B T}\right] \tag{3.14}$$

To solve the equation for ions (3.13), we integrate; then

$$e\phi(x) + \frac{1}{2}m_i u_i^2(x) = C_2 \tag{3.15}$$

Now, from the conservation equation (3.9)

$$n_i(x)u_i(x) = C_1 \tag{3.16}$$

where C_1 and C_2 are constants. Imposing the boundary conditions in the plasma $x \to \infty$ we must have $\phi(\infty) = 0$, $n_i(\infty) = n_0$, and $u_i(\infty) = u_{0i}$, then

$$n_i(x) = n_0 \left[1 - \frac{2e\phi(x)}{m_i u_{0i}^2}\right]^{-1/2} \tag{3.17}$$

Now, we have a result that is different form (3.5). This variation implies a drift velocity of ions. To obtain the electric potential into the sheath, results 3.14 and 3.17 , are used in the Poisson's equation

$$\nabla^2\phi = \frac{e}{\epsilon_0}(n_e - n_i) \tag{3.18}$$

Then, the result is the nonlinear differential equation

$$\frac{d^2\phi}{dx^2} = \frac{n_0 e}{\epsilon_0}\left[\exp\left(\frac{e\phi}{k_B T}\right) - \left(1 - \frac{2e\phi(x)}{m_i u_{0i}^2}\right)^{-1/2}\right] \tag{3.19}$$

To get an approximate solution for 3.19, we use the fact that, the potential near the plasma side of the sheath goes to 0V; then, using $e\phi/k_B T << 1$ and expanding in a Taylor's series

$$\exp\left(\frac{e\phi}{k_B T}\right) \simeq 1 + \frac{e\phi}{k_B T} \tag{3.20}$$

For the same reason, it is possible to assume for ions that $e\phi/(m_i u_{0i}^2) << 1$;

then, using the Taylor expansion again

$$\left(1-\frac{2e\phi(x)}{m_i u_{0i}^2}\right)^{-1/2} \simeq 1+\frac{2e\phi(x)}{m_i u_{0i}^2} \tag{3.21}$$

Combining the results (3.20) and (3.21) we have a linear equation

$$\frac{d^2\phi}{dx^2}=\frac{\phi}{X^2} \tag{3.22}$$

where

$$X^2=\lambda_D^2\left(1-\frac{2e\phi(x)}{m_i u_{0i}^2}\right)^{-1} \tag{3.23}$$

Taking finally the boundary condition $\phi(\infty)=0$, the result is

$$\phi(x)=A\exp(-x/X) \tag{3.24}$$

This solution is valid near the plasma side of the sheath and the constant has to be negative, because the thermal energy of ions is assumed less than the kinetic energy, $X \approx \lambda_D$ and the size of the sheath is of the order of the Debye length. Assuming the validity of the solution on the metal surface, the constant A becomes ϕ_w. An important fact comes from (3.22) and (3.23): if the value of the parameter X is imaginary, we have an oscillating solution, then there is no sheath. Therefore, the solution requires that the so called Bohm criterion

$$k_B T < m_i u_{0i}^2 \tag{3.25}$$

has to be satisfied for the creation of the plasma sheath.

3.1.2 Electrostatic probe characteristic curve

Now, let calculate the current measured as a function of the potential applied to a tip, when it is introduced into the plasma. This current will be the addition of electrons and ions currents, then

$$I_p = I_i + I_e \tag{3.26}$$

The current for each species can be calculated as

$$I_\alpha = q_\alpha \Gamma_\alpha A_\alpha \tag{3.27}$$

where Γ_α is the flux given by 3.1 and A_α is the collection area. In the simple model there will be used as assumptions that the average velocity, the collection area and the ion density are constants. As for ions and electrons, the Maxwellian distribution function is used, the flux Γ can be expressed in the form of equation 3.3. For ions density we take the value inside the plasma, n_0, and for the electrons we use the density given in equation 3.14. Using the notation $V' \equiv \phi(r = 0)$ for the probe potential and the temperature in electron-volts (eV) units we get that

$$I_p = eA_i n_0 \frac{\langle v \rangle_i}{4} - eA_e \frac{\langle v \rangle_e}{4} n_0 \exp\left(e\frac{V - V_P}{k_B T_e} \right) \tag{3.28}$$

where V_p is the plasma potential, taken as the reference. If the potential of the tip is negative, the second left term becomes negligible and we have a current due almost only to the ions, then we define

$$I_{si} = eA_i n_0 \frac{\langle v \rangle_i}{4} \tag{3.29}$$

On the contrary, for potentials higher than the plasma potential, the second term becomes relevant and we define

$$I_{se} = eA_e \frac{\langle v \rangle_e}{4} n_0 \tag{3.30}$$

Using the definitions 3.29 and 3.30 in 3.28 we get

$$I_p = I_{si} - I_{se} \exp\left(e\frac{V - V_p}{k_B T_e} \right) \tag{3.31}$$

When the current through the probe is null, the potential of the probe is known as *floating potential* V_f, then, using this fact and doing some algebra we arrive to the known relation

$$V_f = V_p - \ln\left(\frac{I_{is}}{I_{es}}\right) T_e \tag{3.32}$$

for hydrogen plasma the value of $\ln(I_{si}/I_{se})$ is approximately 3. Using the relation 3.32 in the equation 3.31, we finally get the probe current in the form

$$I_p = I_{si}\left[1 - \exp\left(e\frac{V - V_f}{k_B T}\right)\right]. \tag{3.33}$$

where the subscript e was dropped in the temperature, this is the notation that will be used in the rest of the text. We have to take into account that equation 3.33 is valid for potentials below the plasma potential, because in the used model there is no electron saturation current.

An interesting result is the possibility of the density calculation. To do this calculation, we use the definition 3.29 for the ion saturation current and the mean velocity 3.2 for a Maxwell-Boltzmann distribution supposing that $T_i = T_e$. Then, we have that the density can be calculated as

$$n = \frac{I_s}{eA_i}\left(\frac{2\pi m_i}{k_B T}\right)^{1/2}. \tag{3.34}$$

The behavior of the probe current as a function of the applied potential, when it is immersed in the plasma, is sketched in the Figure 3.1. We can distinguish three regions in the curve. The region I is for negative potential, when more electrons are repelled from the pin surface, and the net flux is due to the ions. In that condition, we have a measurement of the ion saturation current I_s^i. This ion current is much lower with respect to the electron current. In the region II, the potential is less negative, the number of repelled electrons decreases and the net current becomes a mix between electron and ion currents. When the dynamical equilibrium is achieved, the ion current and electron current cancels, then, the probe reach the floating potential, V_f. In regions I and II, the equation 3.33 describe the behavior of the probe. It was in this regime that the measurements of our experiment were performed. At a certain potential which is called the plasma potential, V_p, the plasma sheath around the probe disappears and collected ions and electrons are those that hits the probe surface. Above the plasma potential the current of ions becomes null and the current is only of electrons. At this point the probe has reached the electron saturation current I_s^e, this is region III. In tokamak plasma due to the reached temperatures and densities, this region produces a high currents that can harm the electronics used in the measurement circuits.

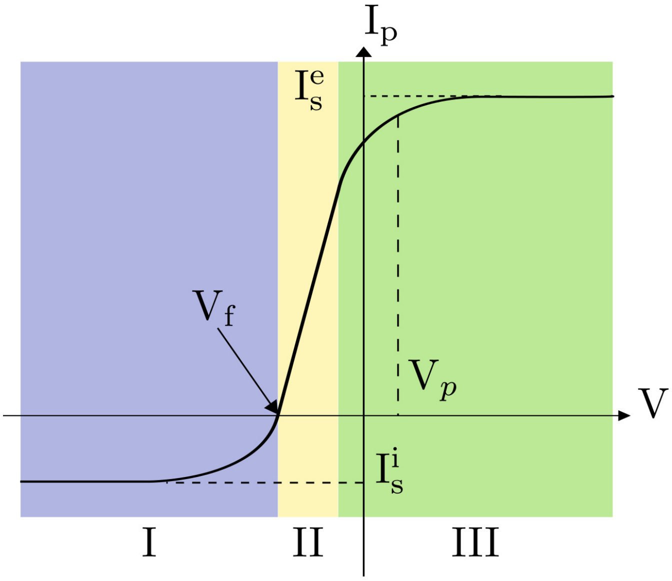

Figure 3.1: Theoretical characteristic curve of the probe [51] .

3.2 Potential sweep technique

For the potential sweep technique, we take the signal of the sweep potential applied to the probe, V_R, and the resultant current, I_R, to get an entire image of the behavior of the probe. The behavior is described by equation 3.33. The scheme of the implementation of the technique is shown in Figure 3.2. The current signal is measured on a shunt resistor of 10Ω, and the sweep potential on a voltage divider due to high potentials in the pin. The potential and current signals measured, are coupled to the coaxial cable impedance using a set of electronic amplifier. Those coupled circuits are shown in the appendix A.

Then, the cycles of the potential sweep are recognized, and for each period, the current is also selected. With those signals, the characteristic curve is constructed and a computational method is used to fit the equation 3.33. Then, the values of the parameters I_s, V_f and k_BT are obtained. One advantage of this method

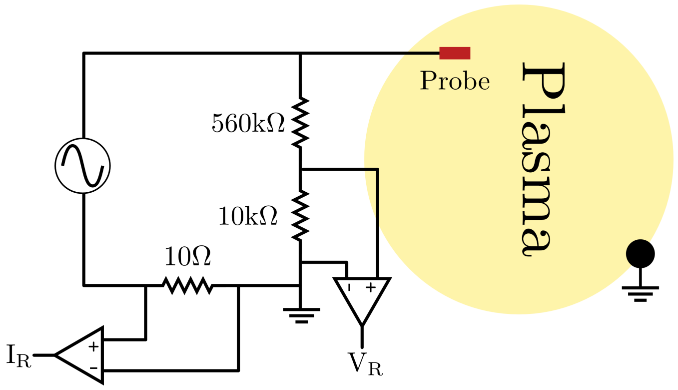

Figure 3.2: Basic system for measurement with the potential sweep technique. The I_R is measured in a shunt resistor of 10Ω. The sweep potential V_R is measured in a voltage divider. The amplifiers couple the signal with the coaxial cable impedance. The reference for the potential measures is the tokamak vessel.

is that the values are well determined when a considerable amount of points is obtained. But, an obvious disadvantage is the sweep frequency, that limits the time rate of the measurements. As an example, for fluctuations in the plasma with typical times lower than 10μs the sweep frequency has to be greater than 100kHz to get at least one characteristic curve. Several practical difficulties related to the implementation of a fast sweeping system at high frequencies (100kHz) are exposed in references [52] and [53]. A variation of this technique is to put the sweep potential between two pins, the so-called *double probe*, described in Ref.[54]. For this configuration the characteristic curve obtained is symmetric, therefore, it has the advantage that high electron currents are not attained.

3.3 Triple probe technique

The triple probe technique was proposed by Chen et al [6] and has become a widely used method for plasma temperature measurement [55, 56, 57, 58, 59]. As the name implies, the technique uses three pins to make the measurement. The configuration of those pins is shown in the Figure 3.3.

From the Figure 3.3, we can see that currents can be described as

$$I_+ + I_- = 0 \tag{3.35}$$

and for the potentials, the configuration gives the equations

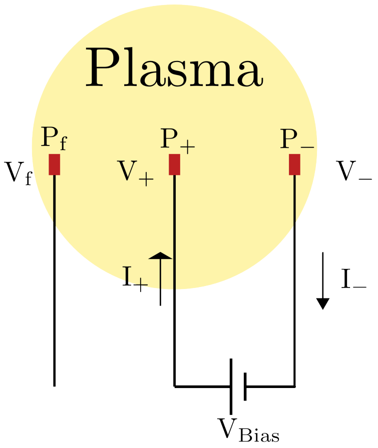

Figure 3.3: Currents and potentials for the triple probe configuration.

$$V_+ - V_- = V_{Bias} \tag{3.36}$$

Now, under the assumption used for the plasma to describe the probes behavior, the currents for the probes can all be described using the equation 3.33

$$I_+ = -I_{s+}\left[1 - \exp\left(e\frac{V_+ - V_{f+}}{k_B T_+}\right)\right] \tag{3.37}$$

$$I_- = -I_{s-}\left[1 - \exp\left(e\frac{V_- - V_{f-}}{k_B T_-}\right)\right] \tag{3.38}$$

Then, knowing the current and potential in the probes we can calculate the ratio between I_+ and the current difference $I_+ - I_-$

$$\frac{I_+}{I_+ + I_-} = \frac{-I_{s+}\left[1 - \exp\left(e\frac{V_+ - V_{f+}}{k_B T_+}\right)\right]}{-I_{s+}\left[1 - \exp\left(e\frac{V_+ - V_{f+}}{k_B T_+}\right)\right] + I_{s-}\left[1 - \exp\left(e\frac{V_- - V_{f+}}{k_B T_-}\right)\right]} \tag{3.39}$$

We will now make the assumption that the plasma is *homogeneous* for the three pin positions. Therefore

$$\begin{aligned} T_{e+} &= T_{e2} &= T_{e-} &= T_e \\ V_{f+} &= V_{f2} &= V_{f-} &= V_f \\ I_{s+} &= I_{s2} &= I_{s-} &= I_s \end{aligned} \tag{3.40}$$

using this assumption in equation 3.39, the fact that $I_+ = I_-$ and factoring the exponential term of the numerator, we have

$$\frac{1}{2} = \frac{1 - \exp\left(-e\dfrac{V_+ - V_f}{k_B T}\right)}{1 - \exp\left(e\dfrac{V_- - V_+}{k_B T}\right)} \tag{3.41}$$

as for the technique, the potential difference $-V_{Bias} = V_- - V_+$ is large than $k_B T$ (in electronvolts) it is possible to ignore this exponential term, then

$$\frac{1}{2} = 1 - \exp\left(-e\frac{V_+ - V_f}{k_B T}\right) \tag{3.42}$$

Finally, solving for the temperature we arrive to the expression

$$\frac{k_B T}{e} = \frac{V_+ - V_f}{\ln(2)}. \tag{3.43}$$

where the temperature is measured in eV units due to the factor k_B/e. For the practical triple probe implementation was used the circuit shown in the Figure 3.4. In this technique we measured the floating potential, V_f, and the positive bias potential, V_+. The floating potential is measured using a voltage divider, as in the case of the potential sweep the relation is 1/56. For the measurement of the V_+ the same configuration is used. For the current, the measurement is done using a shunt resistor of 10Ω, in this case the measurement circuit must be isolated from the system ground. For all the measurements, an operational amplifier is used to couple the impedance of the coaxial cable.

As the triple probe technique uses three pins there is a spatial distribution, this implies that a possible phase error delay occurs if the homogeneous hypothesis is not fulfilled. Because of that, Tsui and coworkers, proposed a modification of the triple probe technique [60], in which, another two pins are added symmetrically with respect to the floating pin, in order to compensate this phase delay error. The main difficult of this modified method is that five pins are needed to make a single temperature measurement. Moreover, the five pin method only considers large scale inhomogeneities, and is still unable to correct spatial inhomogeneities lower or comparable with the whole configuration size.

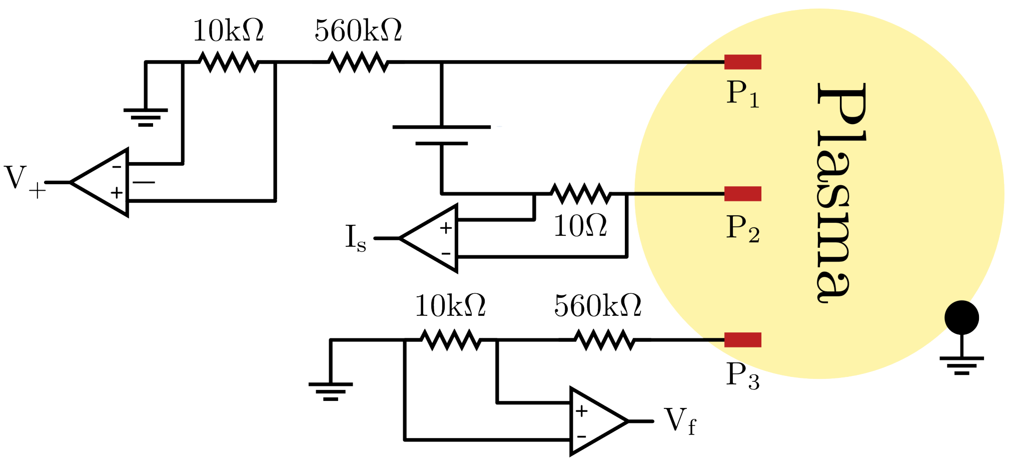

Figure 3.4: Basic system for measurement with the triple probe technique. The reference for the potential measures is the tokamak vessel.

Another approach that has been used more recently is the so called ball pen probe (BPP) [61]. In this approach the electron current that arrives to the probe is diminished because the gyro-radius of electron is smaller than the gyro-radius of the ions as sketched in Figure 3.5.

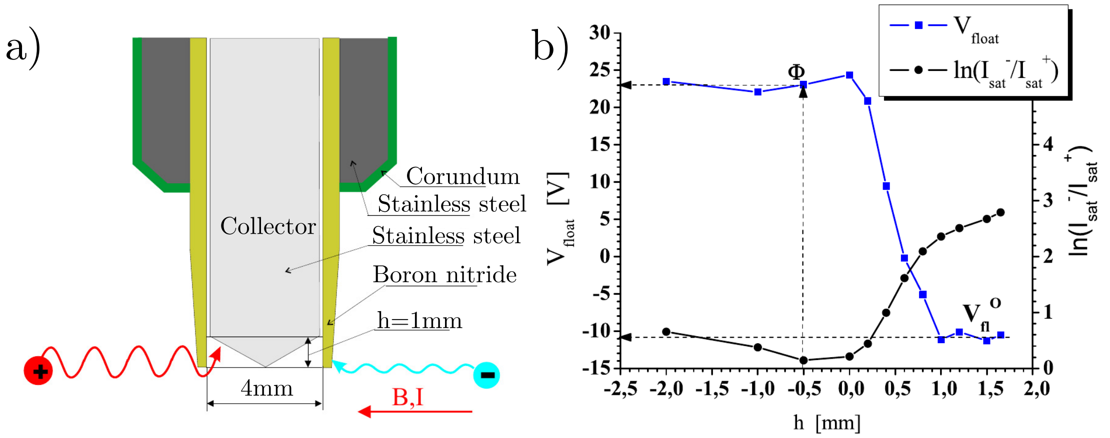

Figure 3.5: a) Basic construction of the ball pen probe. b) Behaviour of the floating potential and ln $\left(I_s^+/I_s^-\right)$ for the BPP. Reproduced form [61].

The retraction of the pin can be increased up to the condition in which the relation between the saturation currents in the equation is one. Therefore, we have that for the BPP, the potential measured, V_{bpp}, is the plasma potential V_p. This result is obtained with the help of the equation 3.32

As we can see from the Figure 3.5.b, if the value of h = 1mm is selected, the ratio between saturation currents is one. To use this technique to measure the plasma temperature it is also needed to measure the V_f with a standard electrostatic probe, and use the fact that for the hydrogen $\ln\left(\frac{I_s^-}{I_s^+}\right) \approx 3$. Finally, the temperature can be calculated from equation 3.32

$$\frac{k_B T}{e} = \frac{V_{bpp} - V_f}{3} \tag{3.44}$$

where the temperature is in eV units.

3.4 Probe arrays

In this work were used two arrays of electrostatic probes. One array use five pin which are set in the configuration show in Figure 3.6. The probes are located at different poloidal and toroidal positions. This array will be call the *five pin probe*.

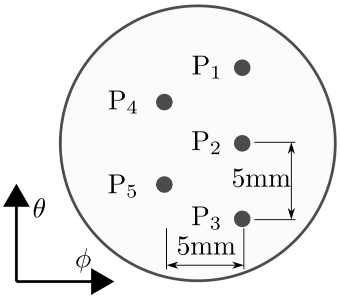

Figure 3.6: Five pin probe array. θ is the poloidal angle and ϕ is the toroidal angle.

The other array is shown in Figure 3.7. In this array the pins are at different radial positions and was developed as a part of the work presented in Ref [17]. This array will be called *rake probe*

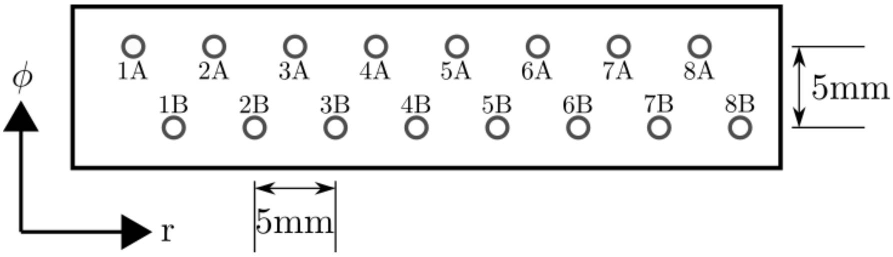

Figure 3.7: Rake probe array. ϕ is the poloidal angle and r is the radial coordinate.

3.5 Conditional analysis

The conditional average is a mathematical tool used to recognize the average characteristics of coherent structures in a turbulent background. The technique was introduced in the 80's by Hussain [7]. The basic idea is to decompose an instantaneous variable $f(\mathbf{x}, t)$ at position $\mathbf{x}$ and instant t as [62]

$$f(\mathbf{x}, t) = F(\mathbf{x}) + f_c(\mathbf{x}, t) + f_r(\mathbf{x}, t) \tag{3.45}$$

where $F(\mathbf{x})$ is the time average of $f(\mathbf{x}, t)$ and $f_c(\mathbf{x}, t) = \langle f(\mathbf{x}, t)\rangle - F(\mathbf{x})$ is the *phase average*. This phase average, is the ensemble average of any property at particular phase of the structure and it is defined as

$$\langle f(\mathbf{x}, t)\rangle = \lim_{N\to\infty} \frac{1}{N} \sum_{i=1}^{N} f(\mathbf{x}, t + t_i) \tag{3.46}$$

where t is the time chose as the reference phase. The term t_i denotes the random time when occurs the coherent structures with the selected phase. Finally, f_r is the part corresponding to randomized background, or structures with spatial and temporal correlations smaller that the selected structure. Now, as show in the Figure 3.8 we select the reference signal, $\phi_{ref}(\mathbf{x}, t)$, in the reference probe and the signal, $\phi_{mov}(\mathbf{x}, t)$, in the movable probe. In the reference signal is searched the condition Φ_c, when the condition is met, the time $\tau = 0$ is defined. Around this the reference time an interval is taken, going from $-\tau_{max}$ to τ_{max}. After the complete scan of the reference signal, there will be N occurrences of the condition Φ_c and an ensemble of N waveforms is obtained. This set is averaged to obtain the *conditional average* for the condition Φ_c. As the pins are separated a distance $\delta\mathbf{x}$ the conditional average is calculated as

$$\begin{aligned} \phi(\mathbf{x} + \delta\mathbf{x}) &= \\ &= \langle \phi_{mov}(\mathbf{x} + \delta\mathbf{x}, t + \tau) | \phi_{ref}(\mathbf{x}, t) = \Phi_c \rangle \\ &= \frac{1}{N} \sum_{i=1}^{N} [\phi_{mov}(\mathbf{x} + \delta\mathbf{x}, t + \tau) | \phi_{ref}(\mathbf{x}, t) = \Phi_c] \end{aligned} \tag{3.47}$$

This conditional average then has the property to extract the coherent component of the signal and average out the turbulent component of the ambient. Therefore, this method is widely used in the study of coherent structures in turbulent systems [42, 63, 64**?**].

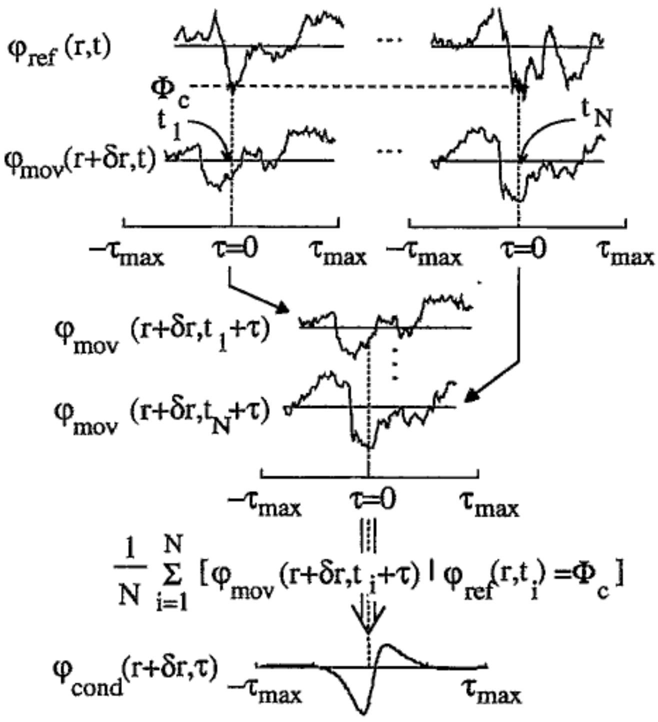

Figure 3.8: Diagram showing the outline of the conditional analysis. Reproduced from Ref.[62].

Chapter 4

Temperature measurements

In this chapter, we present the results obtained from local temperature measurements made by Langmuir probes with voltage sweep method and triple probe method. The two techniques are improved to include a parameter which take into account the correction due to expansion of the sheath region with applied voltage, that gives rise to non saturation of the ion current. Next, we present the comparison between the techniques of triple probe, and voltage sweep. To acquire the experimental data we used discharges with low MHD [1] activity and almost stationary conditions (it is, almost constant density and plasma current). The signals of a typical TCABR plasma discharge considered in this work are presented in Figure 4.1, in this case due to a fail in the interferometer, the bolometer is used to indicate the constant behavior of the plasma density.

The measured signals to use the triple probe technique were, the floating potential, V_f, and the potential of the pin positively biased, V^+. For the potential sweep technique we generate the characteristic curve of the probe by sweeping the probe potential, V_R, and measuring it simultaneously with the probe current, I_R. The sweep frequency was around 1.5 kHz. It is interesting to note in the Figure 4.2 that a little increase of positive potential in the sweep signal V_R causes a rapid increase in the current I_R measured in the pin. Finally, the saturation current I_s is measured by applying a constant biasing in the probe and measuring the probe

---

[1] In our work low MHD activity refers to the absence of high amplitude oscillations in the Mirnov coil signals in the plateau region of density.

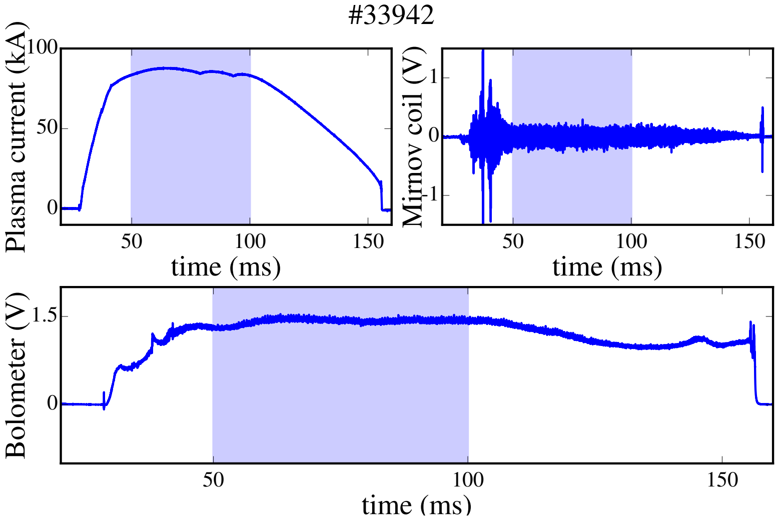

Figure 4.1: Plasma current, the reference Mirnov coil and bolometer for the discharge #33942 as an example of the analysis conditions. The light blue boxes represent the interval of time used for the analysis

current. The potential applied was around -140V. The I_s signal is used in the analysis of the extreme events. Those signals are shown in Figure 4.2.

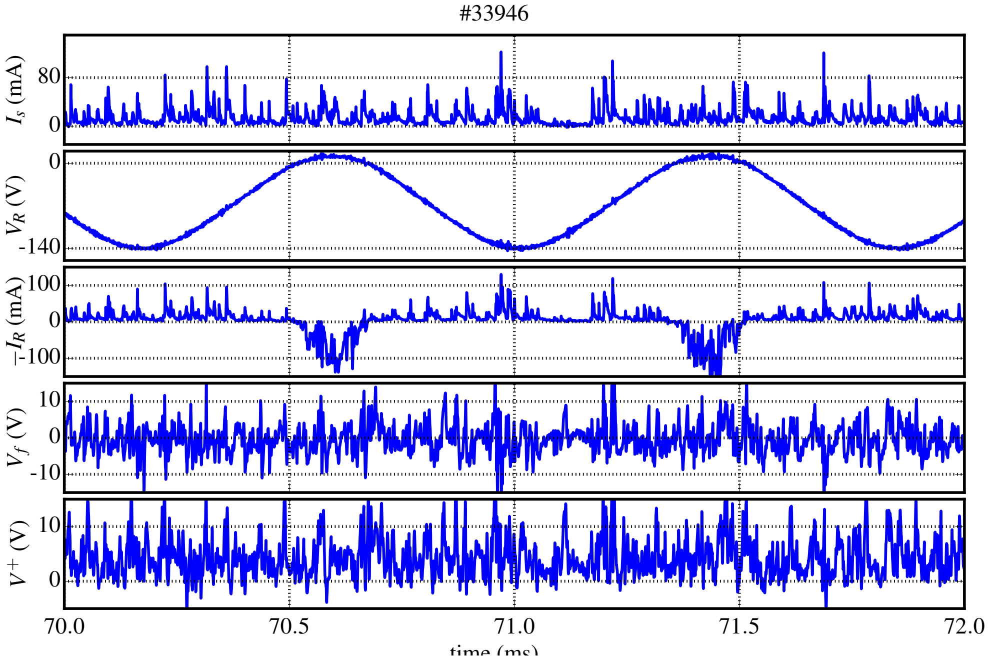

Figure 4.2: Signals used by the sweep potential and triple probe techniques for the discharge #33946. Ion saturation current I_s, sweep potential V_R, current due to the sweep potential I_R, floating potential V_f and positive potential for the triple probe technique V^+.

4.1 Potential sweep technique analysis

To collect the data for the potential sweep technique, we acquire the signal of the ramp voltage, in this case a sinusoidal that goes approximately from -130V to 10V. The maximum and minimum potential values are adjusted using a potentiometer in the module of the biasing sweep system. The limits of the potential are selected in such way that it is possible to see both, the ion saturation side and the beginning of the part when the electron and ion currents contribute to the probe current. Those are the regions I and II that are shown in Figure 3.1. Also, the frequency can be adjusted and in our measurements it was around 1.5kHz. Once we get the data of the applied potential V_R and the current I_R for this potential the result is a great amount of dispersed points as show in Figure 4.3.

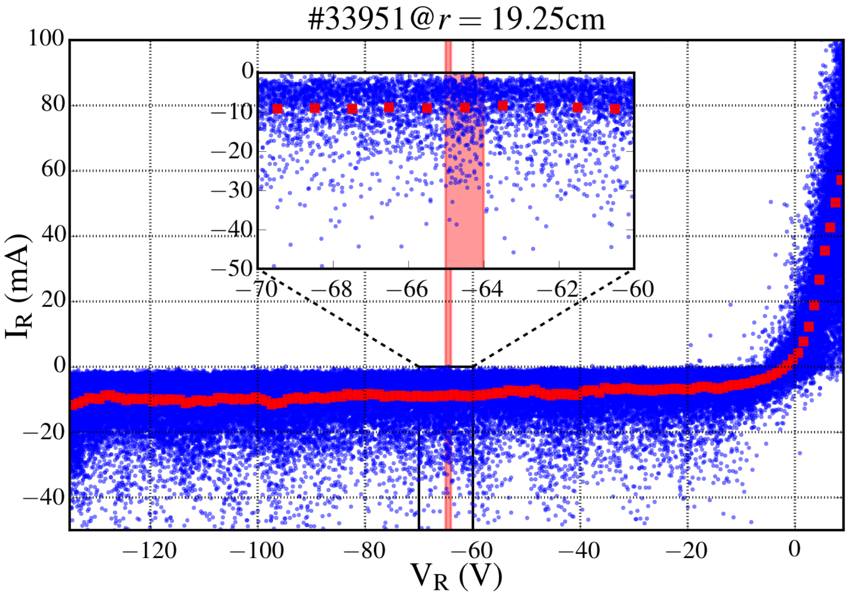

Figure 4.3: Raw data (blue dots) for the I_R as a function of V_R and the mean values for the current for a set of potentials (red squares). In the zoom panel the points in the red light box are those used to get the mean value which is represented by the red squares. The standard deviation of the mean is used as uncertainty but it is too low to appear as an error bar. The data correspond to discharge #33956 at $r = 20.00$cm.

As it can be seen in Figure 4.3, the raw signal of the current as a function of the potential (shown as blue dots) have a great dispersion. For this reason, to get the points to fit the function given by equation 3.33, a set of nvoltage values is selected. For each voltage in an interval around of typically 1V the current values are used to create an ensemble. Then, the mean value of the ensemble is calculated and together with the voltage value, form a pair of values (V_i, I_i). The set of all pairs (V_i, I_i) is used to fit the function 3.33, which describes the probe behavior. The set of data (V_i, I_i) are shown as red squares in the Figure 4.3. As an example, the red box is the region around a voltage value, in this case -64.5±0.5V. The blue dots in the red box are the ensemble of current values, this ensemble has a mean value of -10mA. The standard deviation of the mean value is also calculated for each set of currents, and this standard deviation is used as the uncertainty for the fit; for a great amount of points, this uncertainty is low and for this reason the uncertainty bar can not be seen in the Figure 4.3. Once the set of points is calculated, it is used the Levenberg-Marquardt technique to fit the function for the characteristic curve of the equation 3.33. The Levenberg-Marquardt method is used to fit because the nonlinear relation of the parameters and the data for the used function. The Levenberg-Marquardt is technique is explained in the Appendix B. The data, uncertainties and the fitted functions for different radial positions are show in the Figure 4.4. As it can be seen, when the potential is very negative there is a systematic error because the curve does not fit the behavior. The discrepancy is explained as the model used supposes that the saturation current for the ions is constant, which is not true in this case.

It is known that the non saturation of the ion current is caused by the increase of the thickness of the plasma sheath, when the potential applied increases for negative values. As shown in [4], the length of the plasma sheath around the probe tip as a number of Deby lengths λ_D can be obtained from the Poisson equation

$$\nabla^2 V = -\frac{e}{\epsilon_0}(n_i - n_e) \tag{4.1}$$

In the basic model the electron density is assumed negligible. For the ions the thermal energy is assumed small, then, the velocity is given by

$$v_i = \left(\frac{-2eV}{m_i}\right)^{1/2} \tag{4.2}$$

Now, using the fact that the density current that cross the plasma sheath is

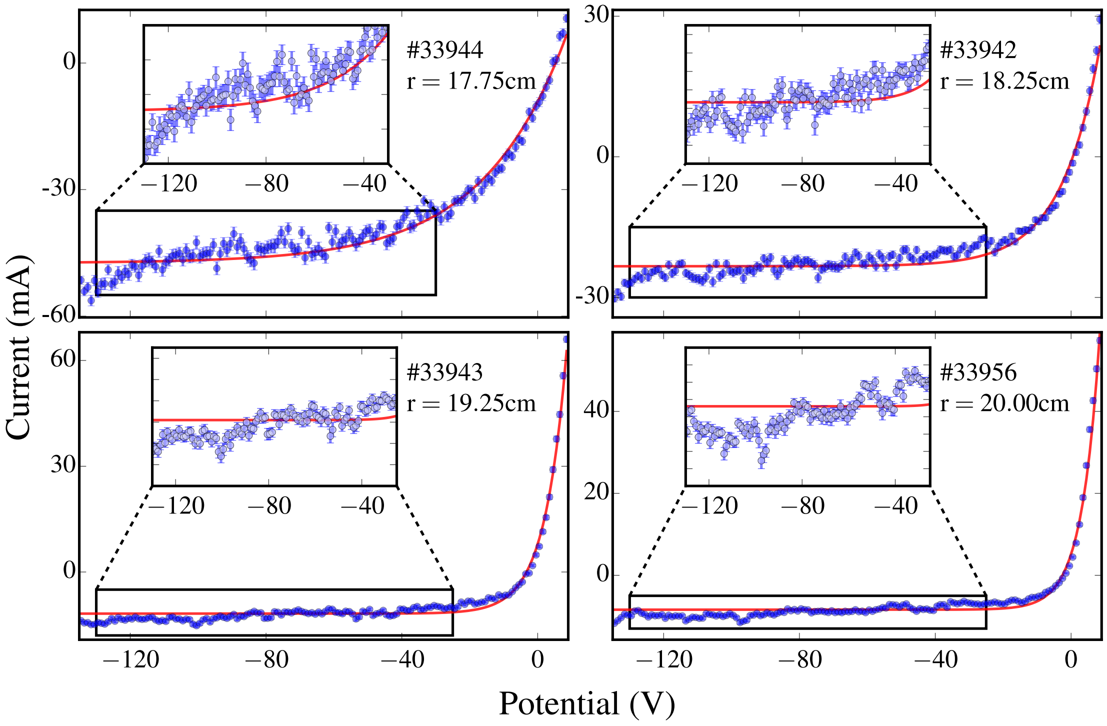

Figure 4.4: Examples of fits of the probe characteristic curve given by the equation 3.33 for four different radial positions. The zoom is shown for the negative potential, the region when the potential is so netive that the model expects a current saturation.

$$J_i = A n_i v_i = A\Gamma_i \tag{4.3}$$

the density can be expressed as

$$n_i = \Gamma_i \left(\frac{m_i}{-2eV}\right)^{1/2} \tag{4.4}$$

where was used the equations 4.2. Using the last expression in 4.1 and a slab approximation we get

$$\frac{d^2V}{dx^2} = -\frac{e}{\epsilon_0}\Gamma_i \left(\frac{m_i}{-2eV}\right)^{1/2} \tag{4.5}$$

Solving this equation for the probe surface $x = 0$ with $V(0) = V_0$ to the *end* of the plasma sheath $x = x_s$ with[2] $V(x_s) = -T_e/2$ (with T_e in eV) we get

$$\frac{x_s}{\lambda_D} = \frac{2}{3}\left[\frac{2}{\exp(-1)}\right]^{1/4}\left[\left(\frac{-V_0}{T}\right)^{1/2} - \frac{1}{\sqrt{2}}\right]^{1/2}\left[\left(\frac{-V_0}{T}\right)^{1/2} + \sqrt{2}\right] \tag{4.6}$$

---

[2] This temperature is valid near the plasma column edge

where the reference potential is the plasma potential. This function is plotted for different temperatures in Figure 4.5.

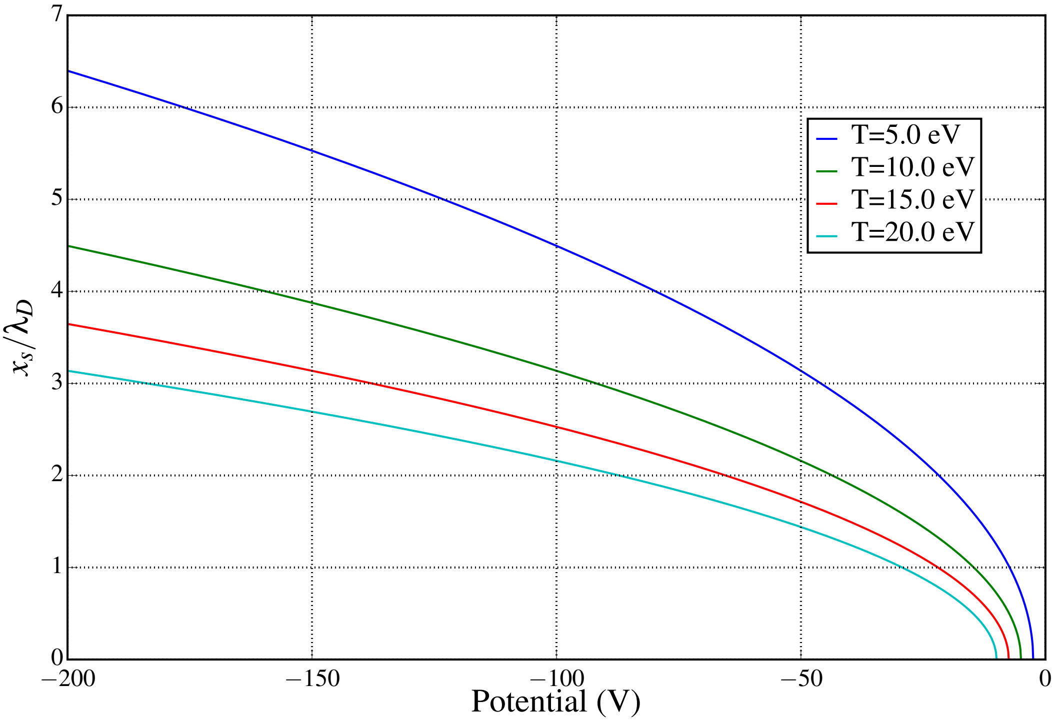

Figure 4.5: Length of the sheath of the ion collection as a function of the tip surface potential for different temperature values.

Taking into account that the plasma potential is given by $V_p \approx V_f + 3T_e$, then all the measured potentials are negatives with respect to the plasma potential. For negative potentials, less than approximately -30V, the behavior of the plasma sheath size becomes approximately linear. Then

$$x_s \approx -aV_0 \tag{4.7}$$

With this result and the fact that, for a cylindrical tip with radius r_t the increase in the area when the radius increases x_s is given by

$$A = A_0 \left(1 + \frac{x_s}{r_t}\right) \approx A_0 \left(1 - \frac{a}{r_t} V_0\right) \tag{4.8}$$

We get that the increase in the area of the ion collection, can be modeled with the addition of a linear factor. This factor reflects the behavior of the not saturation of the ion current when the bias potential is negative. To take in account this behavior, the characteristic equation of the electrostatic probe given in equation 3.33 is modified adding a linear term:

$$I = -I_s \left[1 - \alpha \left(V - V_f \right) - \exp \left(\frac{V - V_f}{T_e} \right) \right] \tag{4.9}$$

where the parameter α express the non saturation in the ion current due to the sheath expansion. Using the same data used for the function without correction, but in this case using the corrected model, we get the fit shown in Figure 4.6. It can be seen that the additional term improves the fit for very negative potentials, this change is observed at all radial positions.

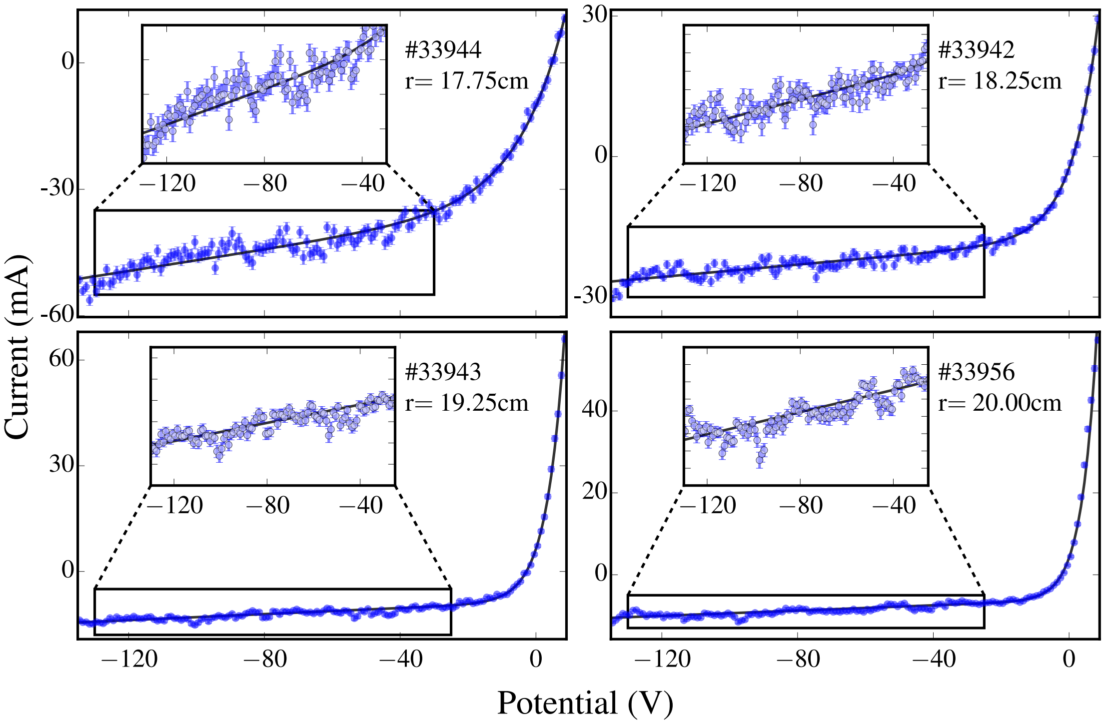

Figure 4.6: Fit for the corrected characteristic function given by equation 4.9 for four different radial positions. A zoom is shown for the region where the potential is negative.

However, it must be noticed that when the parameter α is added, the modulus of the correlation coefficients between α and I_s, and between α and T, reach values near to one as it can be seen in the Figure 4.7.a. Therefore, the introduction of this correction term introduces a high statistical correlation between the saturation current and the temperature.

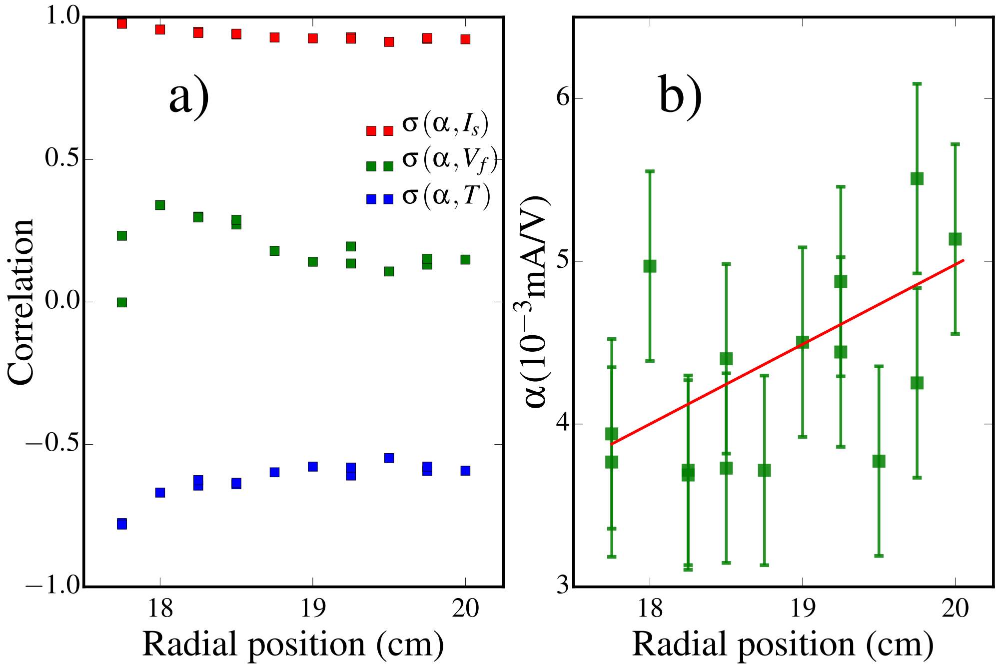

Figure 4.7: a) The correlations for the fit using the α parameter as a free parameter. b) The fit using the quadratic model for α at four different radial positions. A zoom is shown for the functions when the potential is very negative.

Due to the high correlation caused by the α parameter, we decided to use a model to obtain it and then be used as a fixed parameter when the fit is performed. To do that, a linear function were fitted to the values of α as a function of the radial positions, the fit is shown in the Figure 4.7.b. The resultant function fit was:

$$\alpha = [3.94 + 0.43(r - 18)] \times 10^{-3} \tag{4.10}$$

where r is the radial position of the probe in cm, with respect to the geometric center of the plasma column.

Now, the data obtained by the electrostatic probes is fitted using the corrected expression 4.9 . But, in this case the α parameter is calculated with the aid of equation 4.10 and given as a constant in the fitting function. This procedure reduces the number of free parameter to three. The fit for different radial positions using the parameter calculated from the linear model is shown in Figure 4.8.

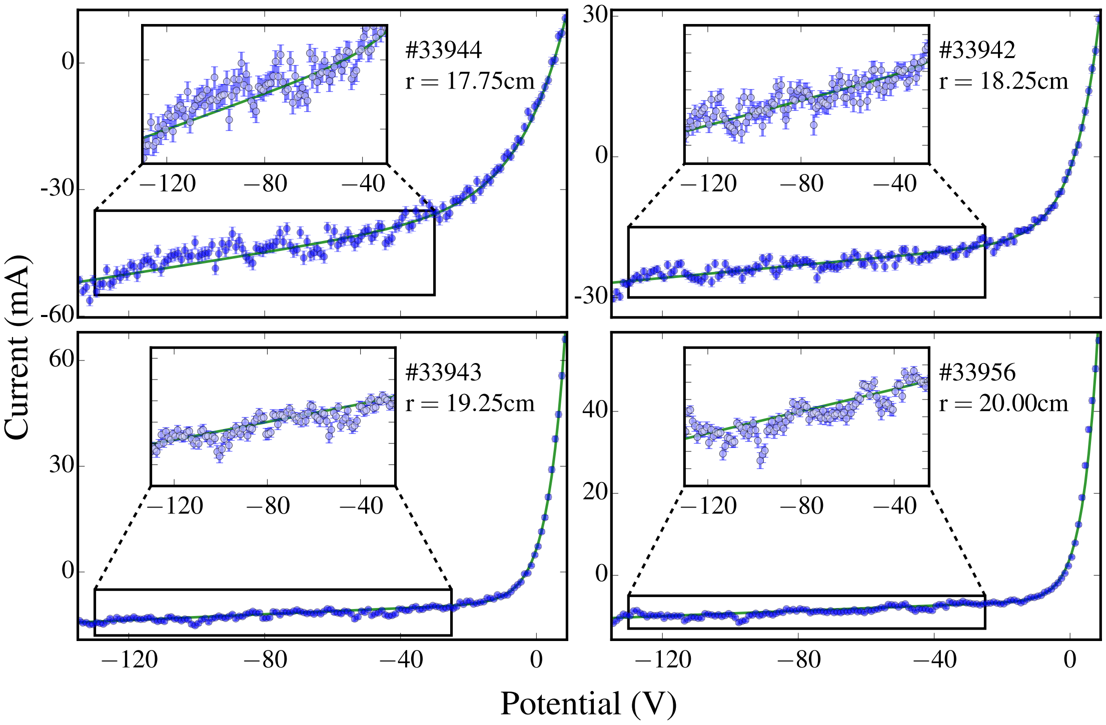

Figure 4.8: Fit for the characteristic function using the linear model of α for four different radial positions. A zoom is shown for the region where the potential is negative.

Another model tested was to use the α parameter as a constant value for all radial positions. The utility of this model will be seen in the chapter 5, when we will deal with a reduced number of points to perform the fit. In this case, as the α parameter is fixed there will be just three free parameters allowing us to perform the fit with a reduced number of points. To test this model, the value of α was used equal to the mean of the values calculated in the case when the α parameter was a free parameter. This calculation gives the value $\alpha = 0.0046\mathrm{mA/V}$. The results of this fit are shown in Figure 4.9. Using the fixed value of the parameter to fit the function seems to be a better fit for radial positions near the plasma edge.

To have a comparison between different procedures to fit the probe function, the *reduced* χ^2 was calculated for several discharges and plotted as function of the radial position. The result is shown in the Figure 4.10. It can be seen that the χ^2_{red} increases with the radial position, although in the function without the correction of the plasma sheath expansion, exist in all cases a low performance of

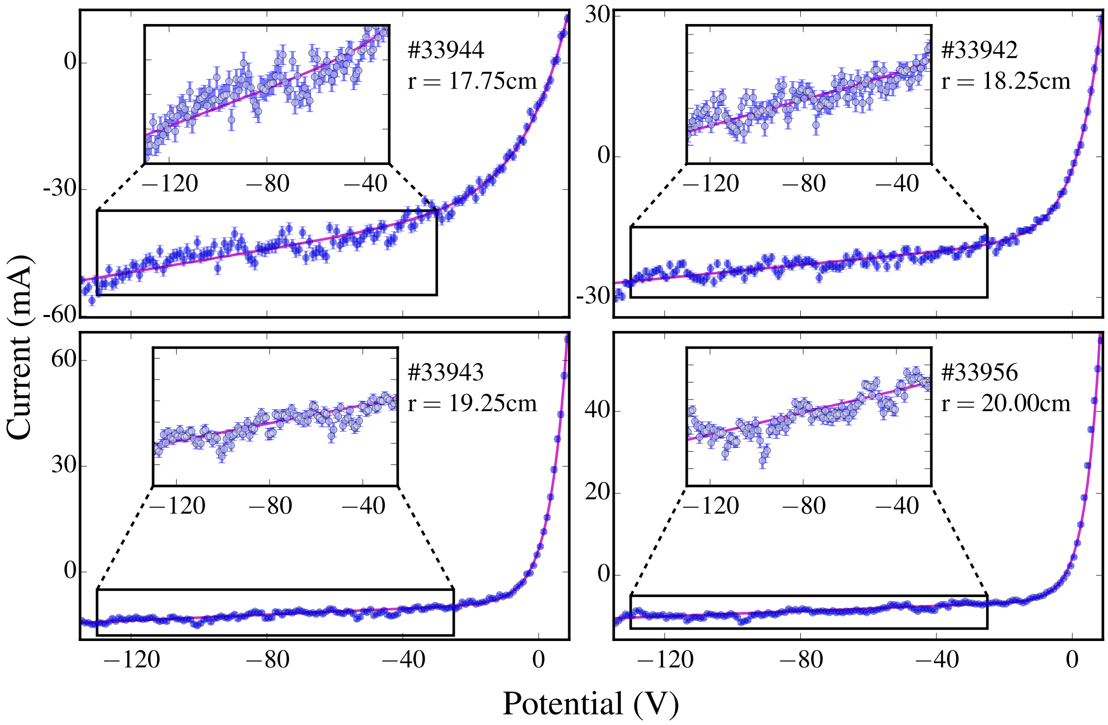

Figure 4.9: Fit for the characteristic function using the mean value of $\alpha = 0.0046\text{mA/V}$ for four different radial positions. A zoom is shown for the region where the potential is negative.

the fit. Another interesting point is that there is no important difference in the χ^2_{red} when α is a free parameter, calculated by the linear model, or a pre-calculated constant. For this reason, the calculation performed in the next analysis used the pre-calculated value for the α parameter.

Although the fit does not reach the desired value of $\chi^2_{red} = 1$, it is necessary take into account that the plasma conditions fluctuate during the analyzed time. Furthermore, the model used is phenomenological and intended for constant conditions and a large number of points with larger uncertainties. These aspects are fulfilled in the subsequent analysis where the work is focused. An important point is the fact that for the pre-calculated value of α the value of χ^2_{red} ranges $2-4$, then, the uncertainties of the fitted parameters can be underestimated. To take into account this fact the uncertainties of the fitted parameters can be corrected by:

$$\sigma_{correted} = \sigma\sqrt{\chi^2_{red}} \tag{4.11}$$

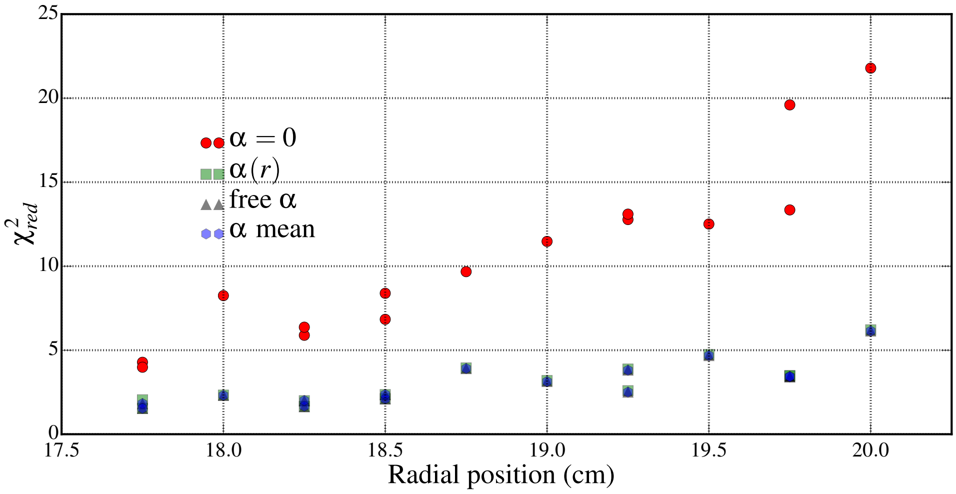

Figure 4.10: Reduced χ^2 for the four fit methods as a function of the radial position

where σ is the uncertainty obtained from the fit.

4.2 Triple probe techique analysis

To test the triple probe technique, it was used the five pin probe in the configuration shown in Figure 4.11, in which it was used two triple probe arrays. In order to estimate the radial profile, the radial position of the probe was changed between the discharges.

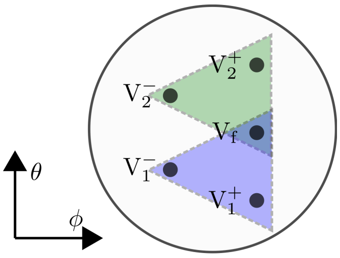

Figure 4.11: Pin configuration used to study the triple probe technique. The shadowed triangles show the spatial distribution of the two triple probe arrays using a common floating potential pin V_f. Besides, for each array the pins with the potentials positive V^+ and negative V^- of the bias source. The poloidal θ and toroidal ϕ directions are shown.

It was discussed in the section 4.1 that the sheath expansion is an important correction in the characteristic function of the probe. Therefore, as the electrostatic probe model is used to obtain the temperature formula for the triple probe technique, the inclusion of the expansion sheath will give a more accurate calculation of the temperature. This is a topic discussed in the references [65, 66, 67]. To estimate the temperature with the sheath expansion correction, the equation 3.39 is used. But in this case with the characteristic function given by equation 4.9 , where it was included the α parameter.

$$\frac{1}{2} = \frac{-1 + \alpha\left(V^+ - V_f\right) + \exp\left(e\frac{V^+ - V_f}{kT}\right)}{-1 + \alpha\left(V^+ - V_f\right) + \exp\left(e\frac{V^+ - V_f}{kT}\right) + 1 - \alpha\left(V^- - V_f\right) - \exp\left(e\frac{V^- - V_f}{kT}\right)} \tag{4.12}$$

Doing some algebra we get

$$\frac{1}{2} = \frac{1 + \alpha\left(V^+ - V_f\right)\exp\left(-e\frac{V^+ - V_f}{kT}\right) - \exp\left(-e\frac{V^+ - V_f}{kT}\right)}{\alpha\left(V^+ - V^-\right)\exp\left(-e\frac{V^+ - V_f}{kT}\right) + 1 - \cancelto{0}{\exp\left(e\frac{V^- - V^+}{kT}\right)}} \tag{4.13}$$

where the canceled term is due to the fact that the applied potential with the source V_{Bias}, given by

$$V_{Bias} = V^- - V^+ \tag{4.14}$$

is of the order of $-6kT/e$, then we have

$$\exp\left(-e\frac{V^+ - V_f}{kT}\right) = \frac{1}{2} + \alpha\left(\frac{V^+}{2} + \frac{V^-}{2} - 2V_f\right)\exp\left(-e\frac{V^+ - V_f}{kT}\right) \tag{4.15}$$

.

Now, solving for the temperature we get the next expression

$$\frac{kT}{e} = \frac{V^+ - V_f}{\ln\left(2 - \alpha\left(V^+ + V^- - 2V_f\right)\right)} \tag{4.16}$$

Using the equation 4.14 to get V^- in terms of V^+ and the applied potential, we can rewrite the expression 4.16 in the form:

$$\frac{kT}{e} = \frac{V^{+} - V_f}{\ln\left(2 - \alpha\left(V_{Bias} + 2(V^{+} - V_f)\right)\right)} \tag{4.17}$$

From the result 4.17 it can be seen that we have an additional term that depends on α. Is important note that the last expression do not needs the measurement of the signal V^{-}, but the value of the bias potential to perform the calculation.

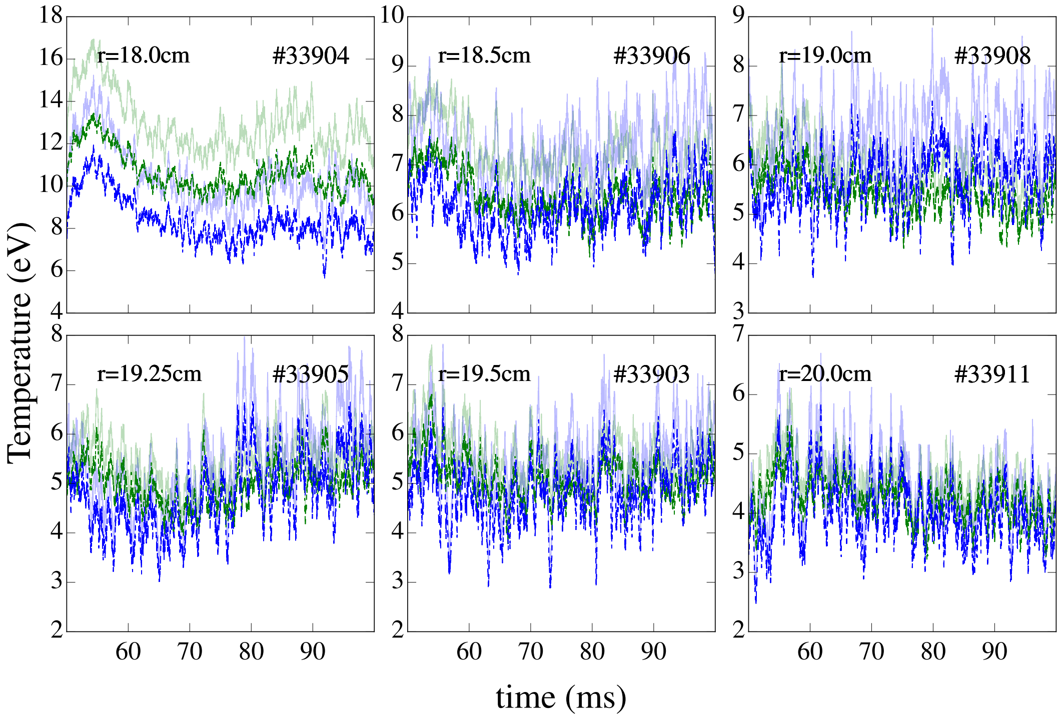

Figure 4.12: Temperature fluctuation measured with the triple probe arrays as a function of time for different radial positions. In green and blue the temperature for the probes 1 and 2 respectively. In light colors the measure for the method without shield expansion correction given by equation 3.43 and in dark colors for the corrected method given by equation 4.17.

To compare the temperature value with and without correction, it was calculated using the normal expression 3.43 and the corrected one given by the equation 4.17. The results are shown in Figure 4.12. For the two arrays, it was used a moving average of 250 points before and 250 points after each point, which implies a total time of 250μs around the point because the acquisition rate is 2MS/s. It can be seen that the temperature decreases with the increase of the radial position of the probe, as expected. The correction makes the temperature values lower with respect to the non corrected ones. An important point is the difference in the values when the probe is in the plasma column edge (r ∼18cm). This difference could be due to a little discrepancy in the gain of the amplification circuits or the shape of the pins in the Langmuir probe wich could change the plasma sheath size.

4.3 Comparation of temperature measurements

To compare the temperature measurement methods, it was used the five pin probe in the configuration shown in Figure 4.13. The technique of sweep potential and the technique of triple probe were implemented at the same radial position, in the equatorial region of the plasma column. For the triple probe, it was used a moving average of 250 points before and 250 points after, this implies a total time of 250μs around.

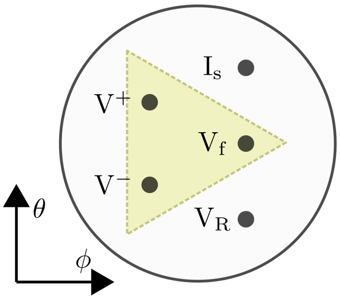

Figure 4.13: Pin configuration for comparison between triple probe and sweep potential techniques. The shadowed triangle shows the spatial distribution of the triple probe array, with the measures of floating potential V_f, the positive potential V^+ and the negative potential V^- of the source. The V_R pin is where the sweep potential is set and the I_{sat} is the pin where saturation current is measured. Also, the directions poloidal θ and toroidal ϕ are shown.

In the case of the sweep potential it was used a senoidal signal with frequency around 1.5kHz. For the calculation of each point it were used four complete cycles, this is, four rising ramps and four falling ramps. The result for the temperature as a function of time is shown in Figure 4.14, where, for two points the experimental data and the characteristic curve fit are presented.

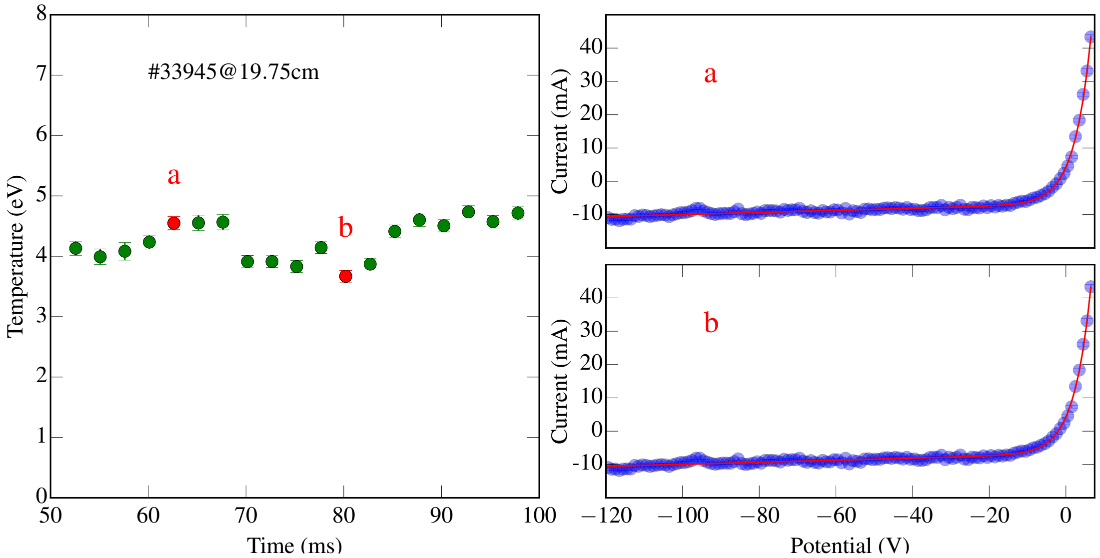

Figure 4.14: Temperature as a function of time using the potential sweep technique. Two points are selected to show the characteristic curve obtained around those times. The fitted functions are shown as red lines

The temperature was calculated using the triple probe technique and voltage sweep technique, for a set of discharges where the probe was put at different radial positions. The results of the measurements of the temperature as a function of time for some discharges are presented in Figure 4.15. The temperature was calculated for the triple probe with and without the correction due to the α parameter. It is interesting how the correction has an important effect inside the plasma, as it can be seen for the radial position 17.75 cm. Another relevant item is that, in the sweep potential, the standard deviations of the measurements increases as the probe gets inside the plasma.

Using the results obtained for several discharges where the 5 pin probe is set at different radial positions, the characteristic profile for the tokamak border is obtained. As expected due to the position of the last closed surface of magnetic field, for positions inside 18cm, the temperature has increases faster. It is interesting to note that the correction that was used in the triple probe technique, decreases the temperature values in the plasma. Those corrected results are more compatible with the potential sweep technique. Moreover, the overestimation of the temperature with the non corrected triple probe technique can be as high as 50%. The overestimation of the temperature value could be a relevant error when the $\mathbf{E}_r \times \mathbf{B}$

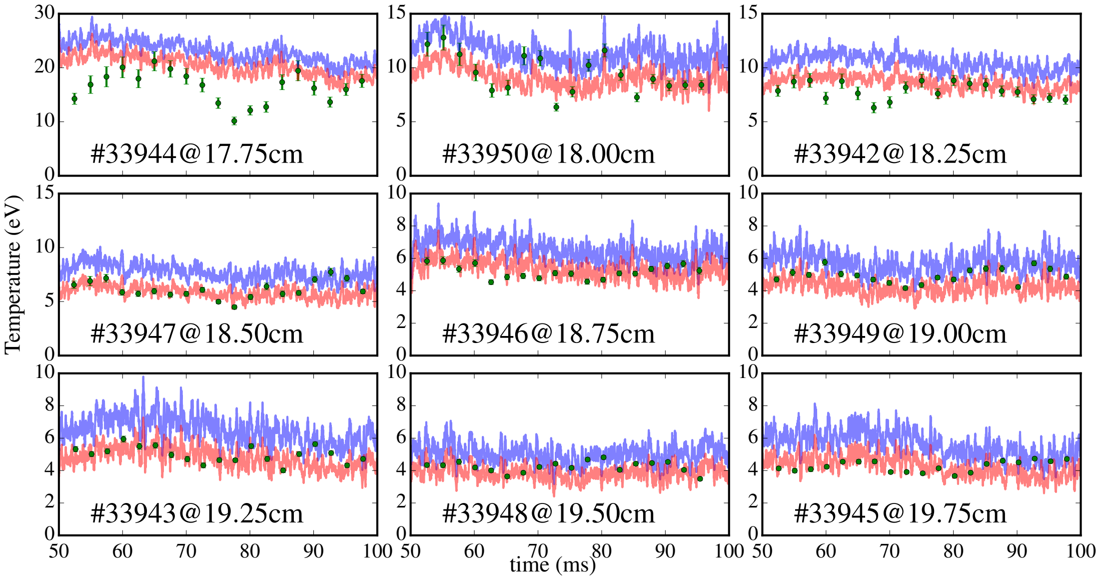

Figure 4.15: Comparison of the temperature calculated for some discharges at different radial positions. In blue the calculation using the triple probe. In red the calculation using the triple probe, but with the sheath expansion correction. In green dots the temperature calculated with the sweep potential technique.

velocity in the poloidal direction is calculated. Because in this case the correction in the plasma potential at different radial positions due to the temperature, will be overestimated by the presence of larger gradient near the plasma border $\sim$ 18cm.

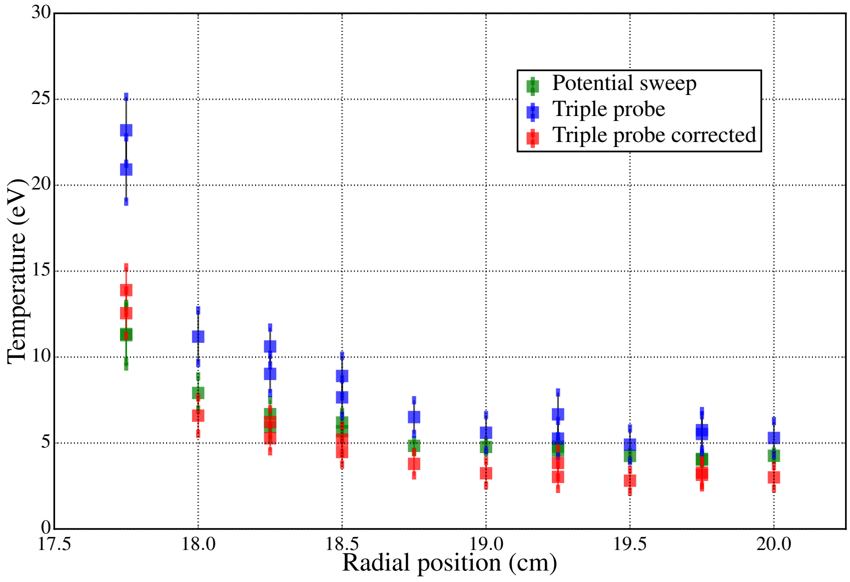

Figure 4.16: The temperature as a function of the radial position for the complete set of the discharges. The measures for the potential sweep, triple probe and its correction due to the α parameter are presented.

4.4 Comparison for V_f and I_s

The potential sweep technique not only gives the local electronic temperature, T, but also the floating potential, V_f, and the ion saturation current, I_s. Those measurements also were obtained by the pin at V_f: a pin with no external polarization. Also, the direct measurement of the saturation current is obtained by the pin that is measuring I_s: a pin biased at a fixed potential of $-120V$. Therefore, those values can be compared to see if the fit for the potential sweep is in agree with another measurement techniques.

To compare the direct measurement of the saturation current and the measurement done by the potential sweep, we have to take into account that in the four parameter function, the I_s constant is not the saturation current measured directly whit a biased pin. When the pin is biased with a negative potential V the equation 4.9 is

$$I = -I_s \left[1 - \alpha \left(V - V_f\right)\right] \tag{4.18}$$

as the exponential part becomes negligible. Then, for the potential sweep technique we really calculate the value of I given by the equation 4.18, using the value of the bias potential applied to the pin in the direct measurement.

In the Figure 4.17 are shown the measurements for V_f and I_s as a function of time for different radial positions. As it can be seen, floating potential measurements are compatible between the potential sweep and the direct measurement. Both have a similar behavior of increase or decrease at the same time, this is clear from the radial position 17.75 cm.

The mean values of V_f and I_s were calculated for each time interval of 50 ms to 100 ms. When there were more than one discharge for one radial position, the mean value of measurements were calculated. The result are the radial profiles of the saturation current and floating potential that are shown in Figure 4.18. In the case of V_f, the values given by the potential sweep technique are systematically a little bit more negative than the values measured directly by the floating pin. In spite of that, the two methods recovers the same behavior, showing an increase

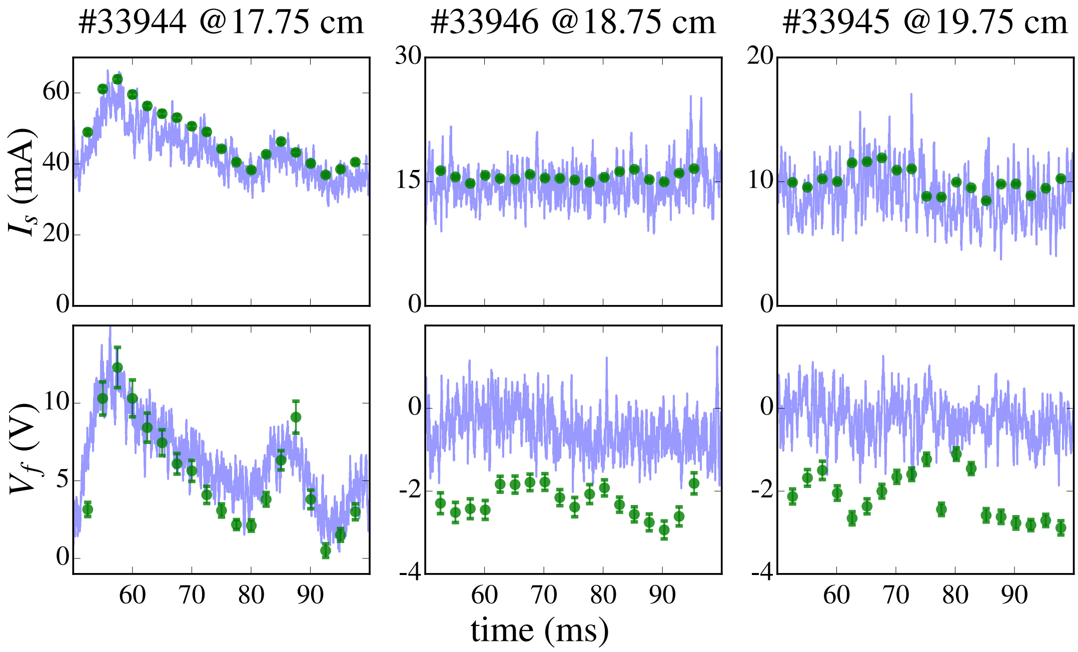

Figure 4.17: I_s and V_f as function of time for three different radial positions with direct measurements (light blue line) and with potential sweep technique (green dots).

toward positive potentials in the radial positions inside the plasma column.

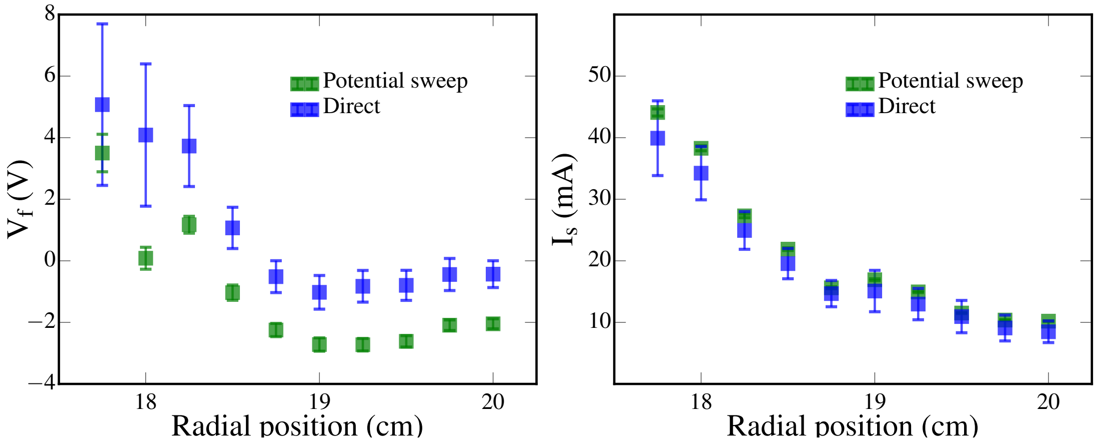

Figure 4.18: I_s and V_f as a function of the radial position of direct measurement (blue dots) and potential sweep (green dots). Those values are calculated as the mean for the time interval 50 ms to 100 ms.

For the ion saturation current, it can be seen that the technique of potential sweep gives values compatibles with the direct measurement, but the two sets have the same tendency to increase the density inside the plasma column. The obtained profile agrees with the expectation because the saturation current has a proportional relation to the density, and for the tokamak there is a rapid increase of the density in the plasma edge due to confinement. This confinement produces a pronounced gradient of the density inside the plasma column.

Chapter 5

Extreme events analysis

The existence of *coherent structures* has been reported in several devices of plasma confinement [33]. Those structures are detected as *extreme events* in the measured signals of the saturation current, which is proportional to the plasma density. Therefore, the term extreme event will be used for the peaks in the saturation current signal and the term coherent structure will be used for the structures that propagates in the plasma and are assumed as the cause of the peaks.

Those coherent structures has been related with the turbulent transport of particles as shown in the Ref. [40]. It is generally accepted that coherent structures are created in the plasma column and then propagates in the radial direction. Those structures propagate with a drift velocity of $\mathbf{E} \times \mathbf{B}$, where $\mathbf{E}$ is the electrid field inside the coherent structure. This drift velocity causes that coherent structures leave the plasma column, propagate across the SOL and finally arrive the vessel wall. This propagation of coherent structures can explain an important part of the anomalous transport. The fact that the drift velocity is compatible with the $\mathbf{E} \times \mathbf{B}$ indicates that an internal dipole is present in the coherent structure. The existence of a coherent structure with higher density that the surrounding plasma and moving in the outside radial direction indicates a particle transport. This topic has been the focus of several works which are reviewed in ref. [3]. However, if the structures comes from the plasma column they will have a higher temperature and this can contribute to the energy transport. The study of this topic has been barely done and more information about this and other characteristic of coherent structures is needed.

Therefore, in this chapter are presented the analysis of coherent structures in the TCABR edge and SOL using the Langmuir probes. First, are presented the statistical behavior that is characteristic of this phenomena and a brief study of the extreme events shape. Then, the conditional analysis is used to obtain information about temperature, floating potential and saturation current when those structures cross the electrostatic probes. To find the temperature the conditional analysis is applied to the signals acquired using the triple probe and the potential sweep techniques. To perform the studies presented in this chapter the main diagnostic was the five pin probe, that allows a detailed turbulence characterization for a poloidal-toroidal plane. A radial rake probe was also used to determine the radial extension of the extreme events.

5.1 Procedure to select the extreme events

The signal of the ion saturation current I_s, which is related to the density as shown in the section 3.1.2, has a series of pronounced spikes as it can be seen in the Figure 5.1. Those signals has been normalized by the standard deviation σ and subtracting the mean value:

$$I_s^{norm} = \frac{I_s - < I_s >}{\sigma} \tag{5.1}$$

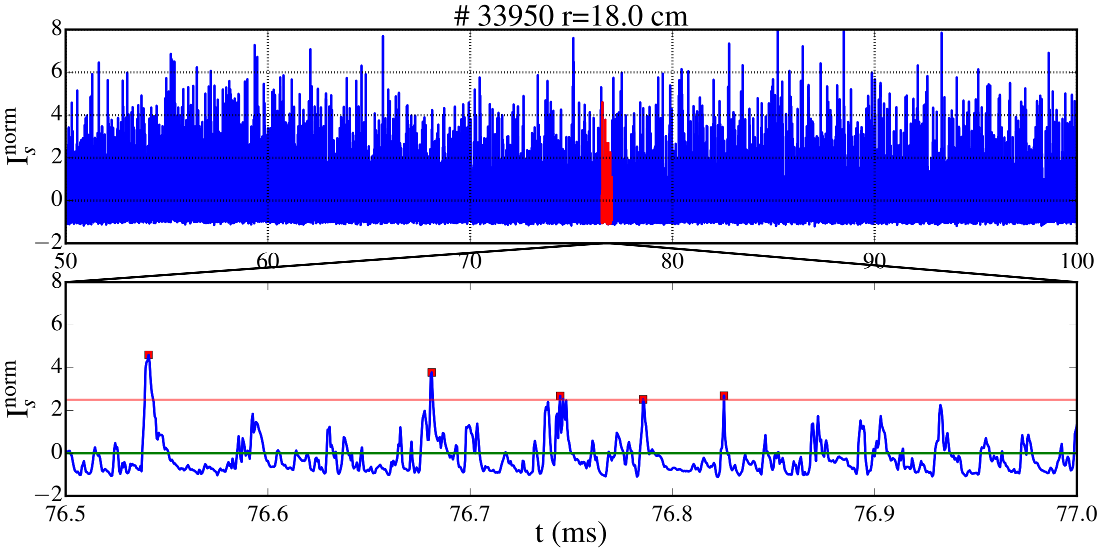

Figure 5.1: Signal for the saturation current with a zoom in the lower graphic. The blue squares indicate the spikes selected as extreme events. The red line shows the level of 2.5 standard deviations above the mean value that was chosen as a criterion to identify the extreme events.

In the same figure a piece of 50μs of the signal is plotted, where the shape of the spikes becomes more clear. This show that those spikes have a quick rising and then a more slow dropping of the I_S value. To select the spikes that are considered *extreme events*, we chose those which the amplitude is at least 2.5 standard deviations above the mean. This trigger value is shown as a red line in the zoom of the I_s.

5.2 PDF, skewness and kurtossis of the signals

A characteristic feature of the extreme events is that the *probability density function* (PDF) for the I_s is a non Gaussian one. To estimate those PDFs the data were normalized in terms of their mean and standard deviations. Then, the histograms were calculated with 200 bins and the counts were normalized by the maximum count of each histogram. In the case where we had two discharges with the probe in the same radial position, the plotted curve is the mean of the two discharges. The PDFs for the saturation current and the floating potential are shown in Figure 5.2. We can see the well known fact that the saturation current, which is related to the density, has a clear deviation from the Gaussian PDF. This deviation is only slightly less pronounced for radial positions toward the center of the plasma column. Meanwhile, for the floating potential the shape of the PDF is similar to the Gaussian PDF for all radial positions.

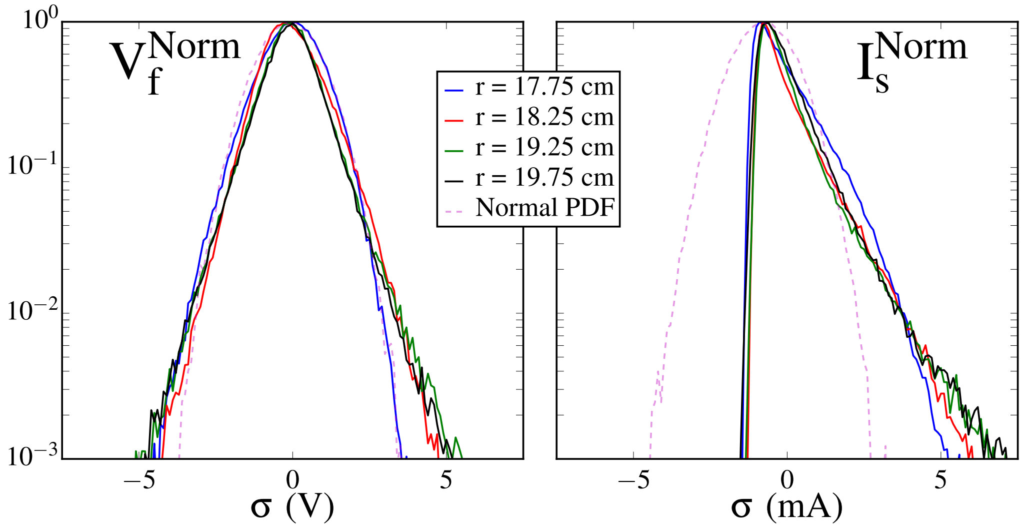

Figure 5.2: PDF for normalized I_s and V_f for different radial positions. The number of events is normalized for the max count. The magenta dashed line is the the Gaussian PDF with standard deviation $\sigma = 1$ and mean zero.

To characterize the PDF shape, the third and fourth moments known as skewness and kurtosis are calculated for the data sets. The result is shown in Figure 5.3 for different radial positions. For the V_f, the skewness and kurtosis values are approximated with those of the Gaussian distribution, skewness=3 and kurtosis=0. For the I_s the values of the two statistical moments increase as increases the radial position. Those behaviors are related to the increase in the positive tail due to the presence of events with amplitudes several times the standard deviation, above the mean value. From this observations, we can conclude that the extreme events are more important for radial positions far from the plasma column.

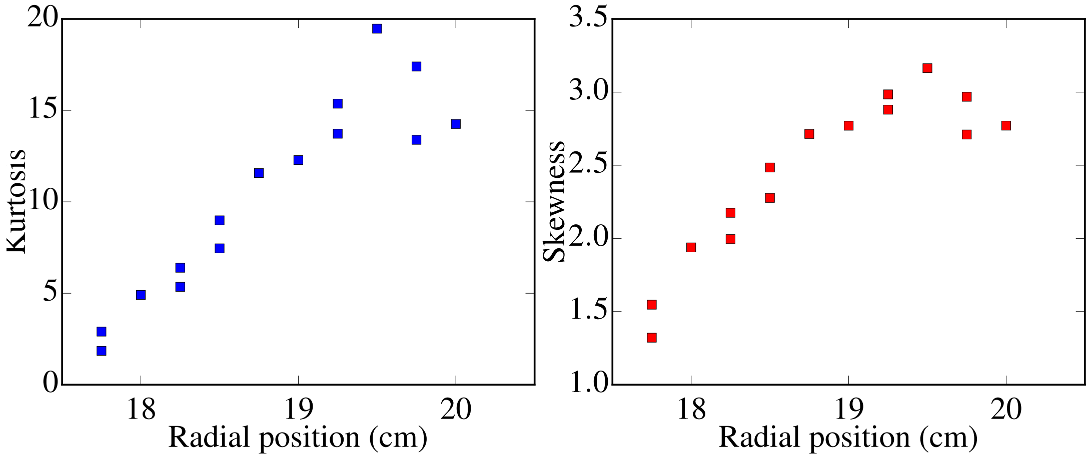

Figure 5.3: Skewness and kurtosis for the saturation current for several discharges at different radial positions.

5.3 Time and amplitude characteristics of the extreme events

As it can be seen in the zoom in Figure 5.1, there are peaks with amplitude several standard deviations above the mean, the so-called extreme events. Those extreme events are related to the detection of coherent structures discussed in the chapter 2, for this reason the term extreme events will be used to refer at those signal peaks. Then the extreme events are assumed to be caused by the pass of a coherent structure across the probe. We can see in the zoom in the Figure 5.1, that the extreme events seem to have a common shape, a quick rise and a relatively slow fall. To obtain a *mean shape* of those events, we used the conditional average method [7] that consists in the following procedure: get all the maxima of the extreme events and around this maxima are collected a given number of points. For our study we use 70 points, that represent $35\mu s$ around the detection time. When we use all the events in the saturation current signal we get a set of different shapes, as shown in Figure 5.4. Finally, the mean value of all the events is calculated and the extreme events mean profile is obtained. This is shown as a black line in the Figure 5.4. This conditional average method is widely used in the study of extreme events in plasma turbulence, see for example ref. [41]. As a result of this method we get a more clear behavior of the extreme events: A symmetric shape for radial positions near the plasma column edge as can be seen for $r = 17.75$, and more asymmetric shape for radial positions in the SOL, where a slowly fall is presented and becomes more clear as the radial position increases. Another interesting fact is that the peaks are lower as the radial position increases, indicating a decrease in the density.

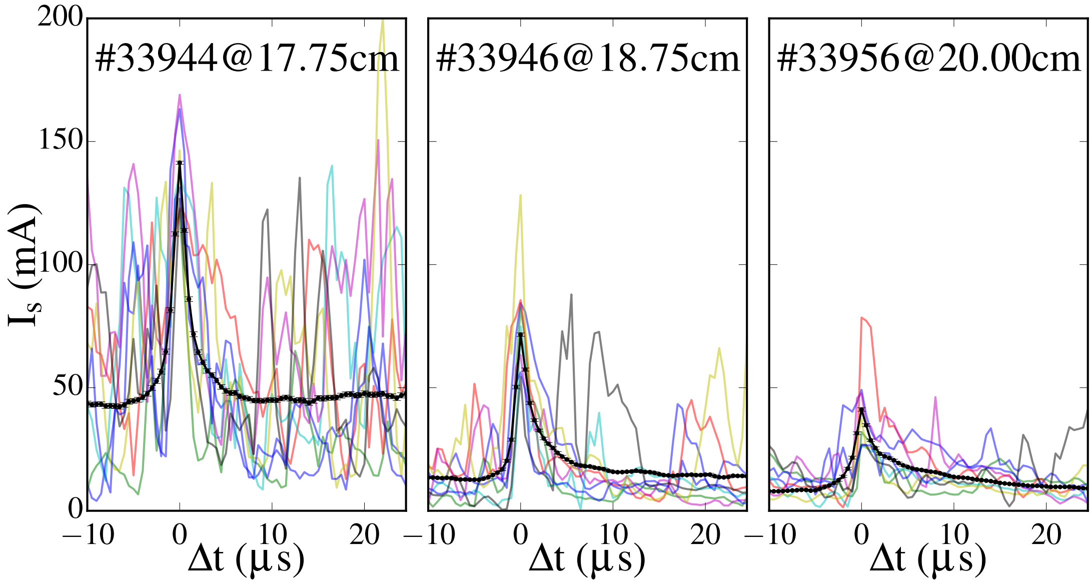

Figure 5.4: Plot of some individual events and in thick black line the correspondent mean profile using all the events in the discharge. The calculations are shown for three radial positions. The three graphics are at the same scale.

To characterize some aspects of the extreme events shape in a phenomenological way, the next model is proposed:

$$I = \begin{cases} A \exp\left(\frac{\Delta t}{\tau_r}\right) + B & \text{if } \Delta t < 0 \\ A \exp\left(-\left[\frac{\Delta t}{\tau_f}\right]^{\gamma}\right) + B & \text{if } \Delta t \geq 0 \end{cases} \tag{5.2}$$

where the parameter B represents the background amplitude, A the amplitude of the peaks, τ_r the rise time constant, τ_f the fall time constant and γ a shape parameter that is used to better adjust the shape of the fall, that is usually slightly different than a simple exponential. In Figure 5.5 is shown the fit of this model for the extreme events mean shape at different radial positions .

In the upper graphics of Figure 5.5 the results are presented using the raw data of the saturation current. In this case, the extreme events amplitude increases for the

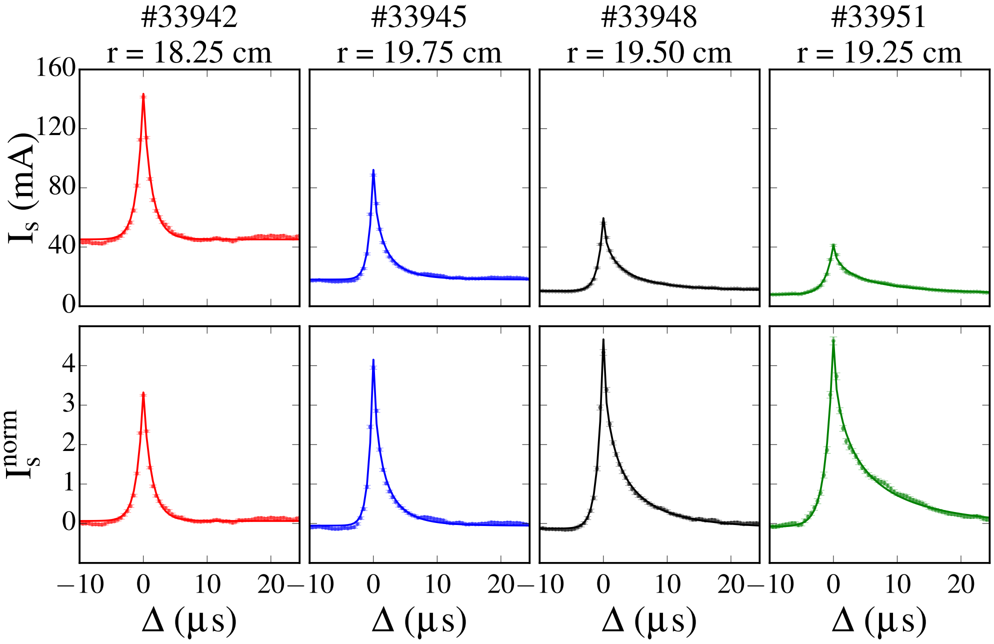

Figure 5.5: Fit of the phenomenological model of equation 5.2 and experimental data for different radial positions. In the upper graphics the result of the conditional average with the raw data and in the lower graphics the result when the saturation current is normalized in terms of the standard deviation

positions near the plasma column, and decreases for positions far from the plasma column. This effect is due to the lower densities outside the plasma column. It is consistent with the widely accepted model that coherent structures comes from the internal part of the plasma column in the case of tokamak or at least from regions with a higher densities for. This model implies that coherent structures can transport particles from internal regions of the plasma column, explaining part of the measurements of anomalous transport. When the function 5.2 is fitted to the extreme event mean shape at several radial positions, we get the results plotted in Figure 5.5. In the lower graphics of Figure 5.5, are presented the results with the saturation current normalized in terms of the standard deviation. When the data is normalized, it can be seen that for radial position near the plasma column, the ratio of the amplitude of the peak in term of standard deviation is less, compared with the amplitude of the peaks as the radial position increases. This behavior indicates that the extreme events are more relevant with respect to the background as the radial position increases. This indicates that in general the coherent structures are more dense that the surrounding plasma at radial positions far from the plasma column. The fitted parameters are shown for several radial positions in the Figure 5.6. In this case the fit has been performed with the raw data of the saturation current.

The background amplitude, B, in Figure 5.6 is proportional to the plasma density without the perturbations and the background level decreases as we go outside the plasma. The extreme event shows a diminution of the density when the coherent structures is detected away from the plasma column. The parameters of extreme events amplitude A, and background B, are calculated without normalize the data. In the part b) of the figure are plotted the parameters that involve the time behavior. The parameters related to the characteristic rise and fall time scales τ_r and τ_r, show the fact that the extreme event becomes more asymmetric as the radial position increases: the extreme events rises quickly indicating a sharper frontal edge of the coherent structure, then, the extreme event has an slow fall indicating a density tail. This behavior can be explained if the structure that crosses the probe has a drop shape consistent with the calculations shown in Ref. [35] and reproduced in the chapter about transport in Figure 2.4. Taking into account that, if the parameter γ is 1 the function is a common exponential, we can see from Figure 5.6.c that the extreme events fall is exponential near the plasma edge and then the fall deviates from the exponential as the radial position increases. This implies an increase in the asymmetry of the coherent structure shape, indicating a mode dense frontal region and a lower dense tail.

Another interesting information, is how many extreme events occur in the selected time interval for different radial positions. As it was commented before, to select a peak as an extreme event a trigger value is fixed and if the amplitude of the event is above this value, the event is selected. Therefore, is calculated the number of event as a function of the trigger value κ, which represent the number of the standard deviations. The result is plotted as blue dots in Figure 5.7 for a signal at $r = 18.25cm$. To fit the obtained results, the exponential function

$$N_b = A \exp\left(\frac{\kappa}{B}\right) \tag{5.3}$$

is used to for the data and the parameter A is taken as the number of extreme

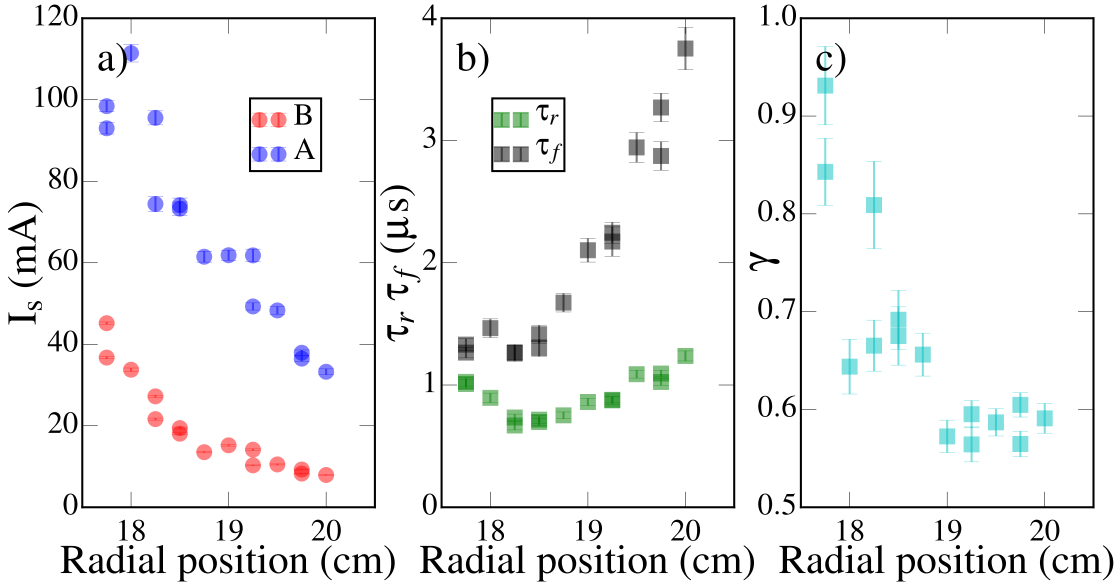

Figure 5.6: Parameters of the model given by equation 5.2 for different radial positions. a) parameters of extreme event amplitude, A, and background amplitude B. b) parameters of the characteristic time scales for the rise, τ_r and fall, τ_c. c) parameter of the fall scale exponent γ.

events for the time interval. An example of the fitted function is plotted in Figure 5.7 as a red line.

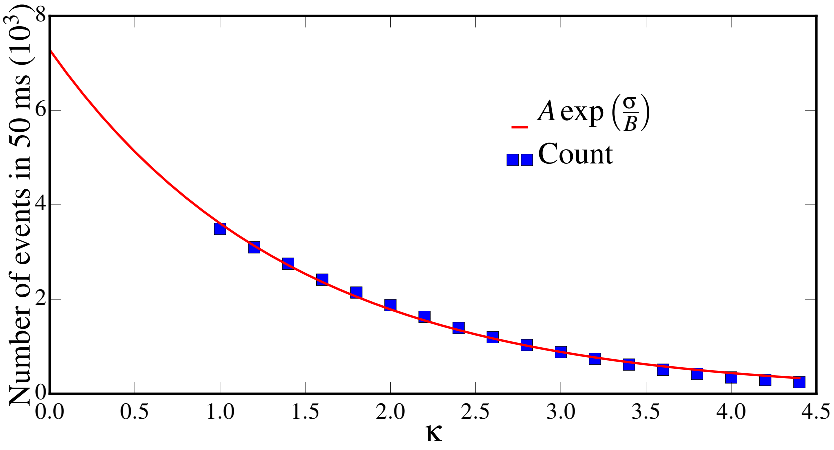

Figure 5.7: The number of selected extreme events in 50ms, N_b as a function of the trigger value in amount of standard deviations above the mean, and the fit for the exponential function given by equation 5.3.

The I_s measured with the five pin probe, is used to calculate the number of events as a function of the radial position using the previous method. Also, the data from a rake probe used in the work of ref. [17] with 8 pins distributed radially and configured in I_S mode, is used to calculate the number of events as a function of the radial positions. The results are show in the Figure 5.8. The two data sets seems to have a compatible behavior. It is important to note that the 5 pin probe and the rake probe have different orientations: the 5 pin probe is place in the poloidal-toroidal plane with it pins oriented in the radial (horizontal) direction, while, the rake probe is placed the radial-toroidal plane with its pins in the poloidal (vertical) direction. Therefore, the pins in the five pin probe measure the mean in the radial direction along the 4mm of the pin length. While, the rake probe measure the mean in the poloidal direction along the 4mm of the pin length. It is interesting that the quantity of extreme events diminish near the plasma column and becomes an almost stable number for positions larger than approximately 19 cm. This behavior could be due to the return of the structures in the plasma for distances near the border that gives different lifetimes, as is shown from the Li-BES (Lithium Beam Emission Spectroscopy) analysis in the ASDEX tokamak [68].

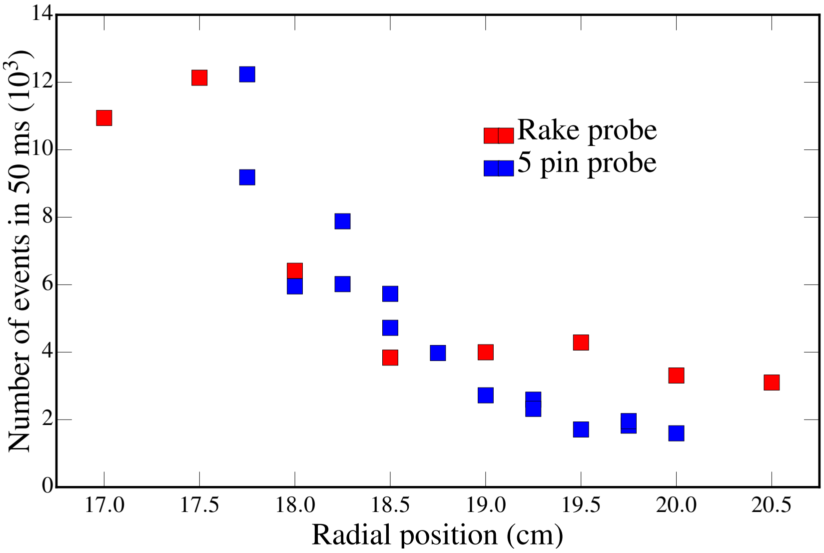

Figure 5.8: The number of extreme events N_b as a function of the radial position.

5.4 Conditional analysis for the extreme events

The conditional analysis is performed for several discharges. In those discharges the five pin probe is set in diverse configurations to perform measurements in the poloidal-toroidal plane to see the dependence of the extreme events characteristics in the poloidal direction. Besides, a rake probe is used to perform some measurements in the radial-toroidal plane to see the extreme event characteristics in the radial direction. In the toroidal direction, the characteristic length of the structures related with the extreme events are of the order of meters as shown in Ref. [38]. Therefore, in the toroidal direction, due to the size of the probes and the kind of measurements done, there are no relevant information obtained. The conditional analysis is performed on the signals in the time interval between 50 ms and 100 ms. This interval corresponds to the region where the macroscopic parameters of the plasma column such as the plasma current and density are almost constants. The N_b extreme events detected in the I_s signal are used as reference to analyze the saturation current, floating potential, electron density, plasma potential and the electron temperature. Meanwhile, in the temperature measurement are used the triple probe and the potential sweep techniques.

5.4.1 Coherent structures poloidal propagation

The first configuration used is shown in Figure 5.9. In this case all five pins are set to measure I_s to see the behavior of coherent structures in the plane perpendicular to the radial direction. This allows the study of the coherent structures propagation in the poloidal direction.

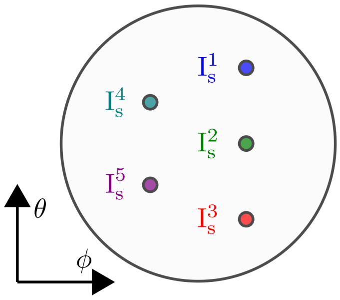

Figure 5.9: Five pin probe configuration using all pins to measure saturation current.

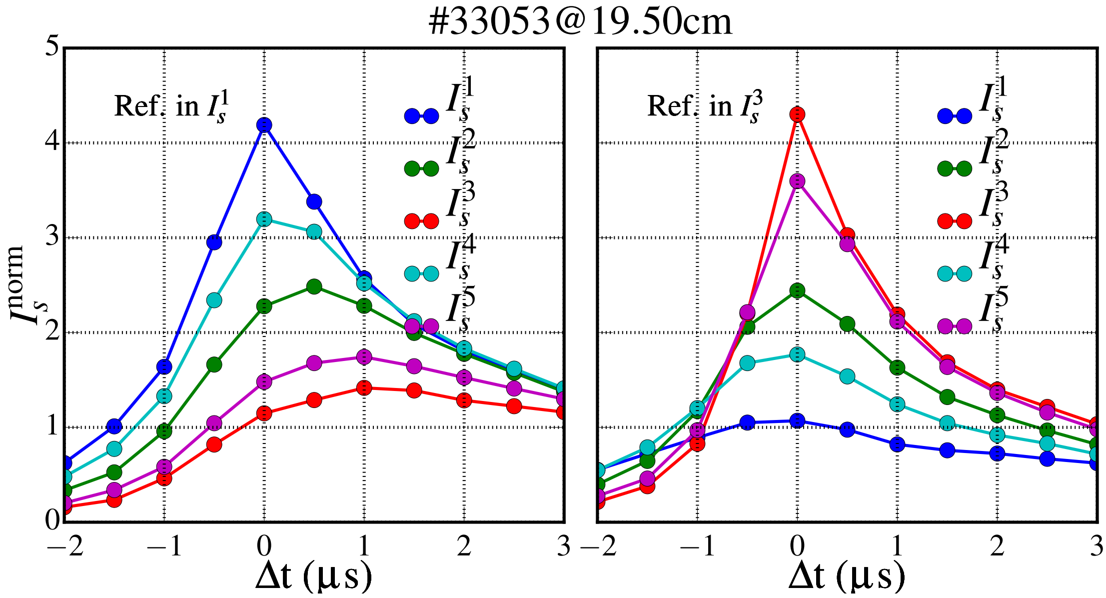

Figure 5.10: Conditional analysis the five saturation currents when the reference is taken in the signals I_s^1 and I_s^3. The measurement is perform with the probe at the radial position 19.5 cm

To perform the conditional analysis, the events in each of the saturation currents can be used as the reference. In the Figure 5.10 are presented the results when the origins of the reference events are selected in pins 1 and 3, this is, the signals I_s^1 of I_s^3 respectively. An interesting observation is that the maximum of the peaks show a delay with respect to the reference pin, in this case up to 1μs. With this delay time and the distance of 1cm between the probes we get an apparent projection velocity in the poloidal direction of the order of 10 km/s consistent in order of magnitude with the measures reported in [41]. One important remark is that this calculation does not mean the poloidal velocity. As shown in [42] the coherent structure has an elongated and tilt structure with a combination of poloidal and radial velocities. Therefore, from this measurement we can obtain and erroneous value of the magnitude and direction for the structure velocity. This topic will be discussed more deeply in the next section.

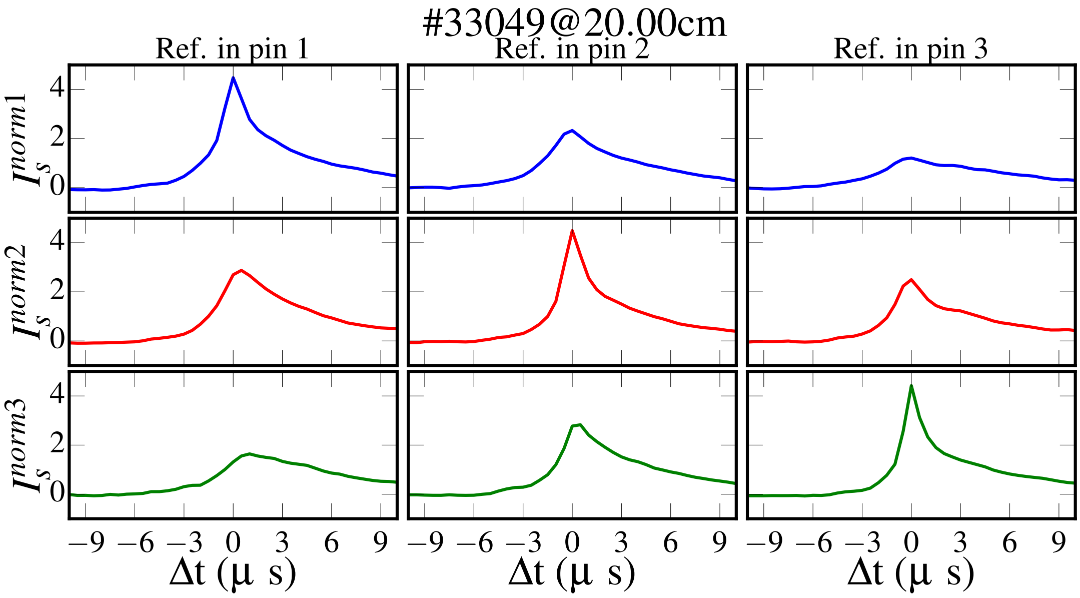

Figure 5.11: Conditional analysis for pins 1, 2, and 3 in the 5-pin probe. In each row a different pin is used for reference. The probe is placed at 19.5 cm

In the Figure 5.11 is presented the conditional analysis for the pins 1, 2, and 3 aligned in the poloidal direction. In each row a different pin is taken as the reference for the conditional analysis. The results of the analysis for pins 1, 2 and 3 is in the columns 1, 2 and 3 respectively. An important point is the symmetry of the coherent structure in the poloidal direction, as can be seen when the the middle pin (pin 2) is taken as reference. When the reference is taken in the extreme pins (1 and 3) we can see again this symmetry in the poloidal direction. The fact that the amplitude decreases as the pin of measure is more distant in the poloidal direction from the reference indicates that the poloidal size of the coherent structure is of the order of two times the poloidal size of the probe. Then, as the distance between the more distant pins 1 and 3 is $\sim$ 1 cm, the structure size is about 2 cm.

5.4.2 Coherent structures radial propagation

Using the rake probe in the configuration shown in Figure 5.12, using pins in saturation current configuration at different radial position, the measure of the coherent structures propagation projection in the radial direction is possible.

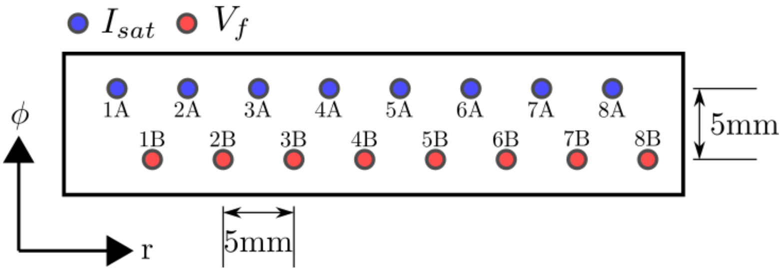

Figure 5.12: Rake probe configuration using all pins in the line A to measure saturation current.

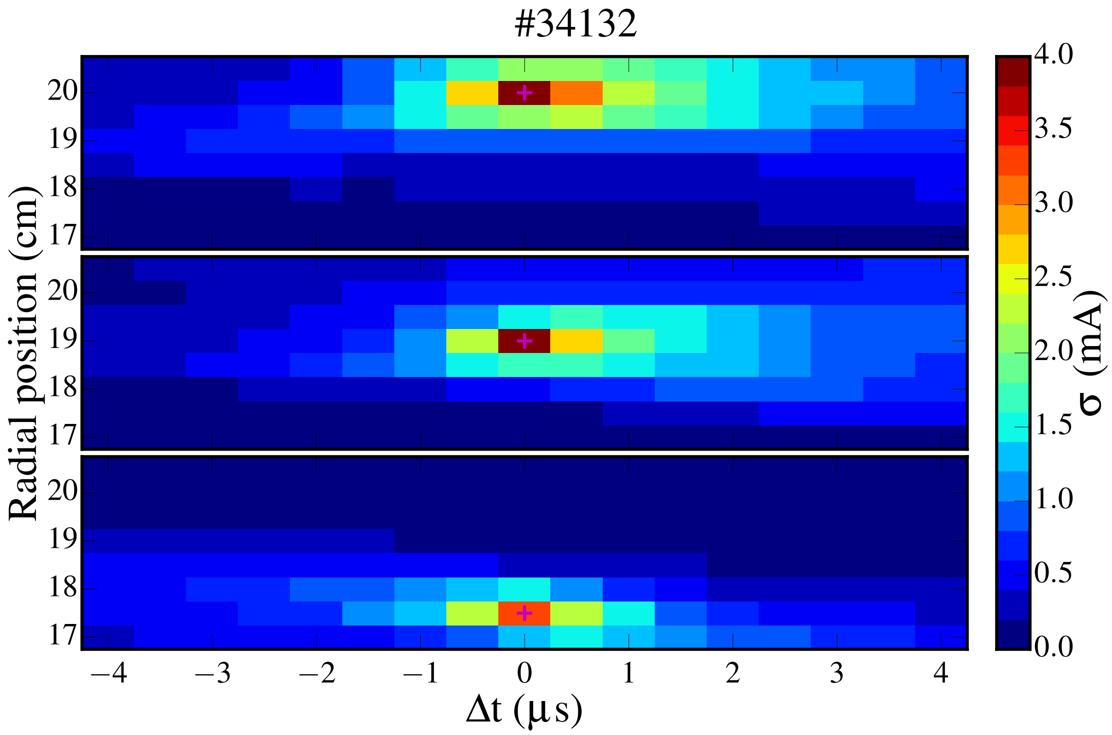

Figure 5.13: Conditional analysis as a function of time and the radial position for the saturation current using the rake probe to analyze coherent structures in the radial direction. The analysis is shown taking as reference 3 pins in different radial positions: 17.5 cm, 19.0 cm and 20.0 cm. The reference pin is marked with a magenta plus symbol. The value of the saturation current show in a color scale is normalized in term of the standard deviation.

In Figure 5.13 are shown the results of the conditional analysis for the eight pins of the rake. In each graph a pin at different radial positions is taken as reference. In this case the results are shown for reference in 17.5 cm, 19.0 cm and 20.0 cm. It can be seen that the extreme events decay more quickly for positions near the plasma edge, producing a more concentrated peak. This result is compatible with the obtained for the 5-pin probe at different radial positions, as can be seen in

Figure 5.5. Since the results are normalized in term of standard deviations, it can be seen how the extreme events are more intense with respect to the background for radial positions far from the plasma edge. It is, the maximum value at 17.75 cm is about 3 standard deviations. Instead, at 20 cm the maximum amplitude is around 4 standard deviations. From the result when the reference is set at 20.0 cm, we can inferred the structure apparent size in the radial direction. Therefore, this structure seems to have a size of about 2 cm, similar to the value obtained for the poloidal direction.

It is interesting to note that, if the reference for the conditional analysis is taken at 20.0 cm coherent structures are detected first in the inward radial positions. This is, the coherent structure begin to appears in the probe at 19.5 cm when time is -1.5 μs, indicating a radial propagation in the outward direction. On the other side, when the reference is taken at 17.5 cm coherent structures begin to appears at 18 cm when time is -2 μs. Therefore, the conditional analysis indicates that the structure is propagating radially inward. When the the reference is taken at 19 cm the movement seems to be radially outward. This behavior can be explained if the structure is tilt in the radial direction. To see this, in the Figure 5.14 is presented the model for an structure tilt with an angle β, propagating with velocity $\mathbf{V_b}$ and detected by the pins P_1 and P_2 separated a distance d. Suppose the structure be detected by the two pins with a delay Δt, then, the apparent velocity $\mathbf{V}_a$ has a magnitude which is calculated as

$$V_a = \frac{d}{\Delta t} \tag{5.4}$$

On the other hand, the real distance d_{ef} traveled by coherent structures is related to the distance d by

$$d = \frac{d_{ef}}{\cos\alpha} \tag{5.5}$$

Then, the apparent velocity using the result of equation 5.5 in 5.4 is

$$V_a = \frac{d_{ef}}{\Delta t \cos\alpha} = \frac{V_b}{\cos\alpha} \tag{5.6}$$

Therefore, the calculation of the velocity using just the delay between the detection of coherent structures in two pins, is incomplete if the tilt angle θ is unknown. Even more, if the angle $\alpha > \pi/2$ the velocity can be calculated with the direction reversed. This effect can explain the results in the TCABR tokamak as show in Figure 5.13.

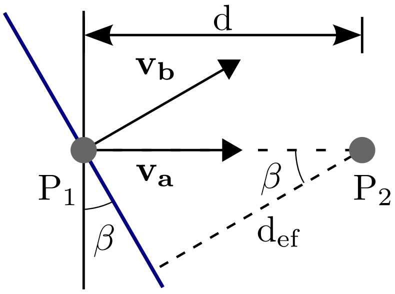

Figure 5.14: Model used to explain the error in the measurements for the velocity using the delay time when the structure is tilt an angle θ.

The model of the tilt structure is used in the data obtained in the HELIMAK machine where this is tilt is shown and it is discussed in the Ref. [69]. In the Figure 5.15, is shown the difference between the real velocity calculated using the 2D data obtained by a grid of probes and the velocity calculated using the delay time between the detection in two pins. The results are presented for the radial and poloidal directions.

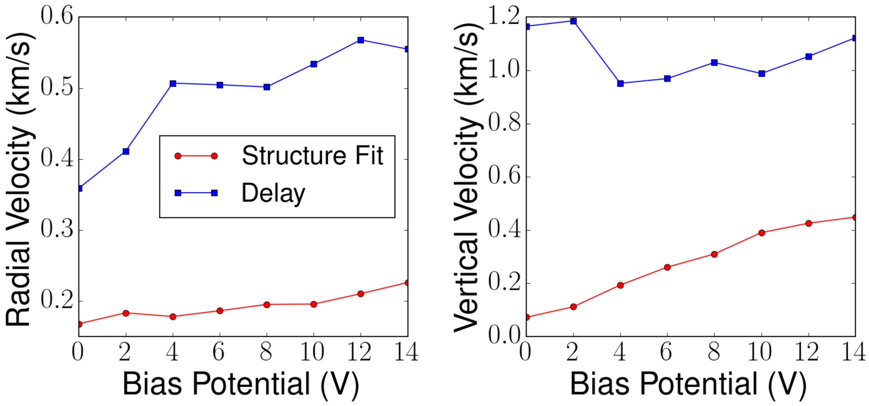

Figure 5.15: Radial and poloidal Velocities of coherent structures calculated using a 2D data, compared with the velocity calculated using the delay between the peak detection in two pins. The data was obtained in the HELIMAK [70].

5.4.3 Coherent structures temperature from triple probe and potential sweep methods

The conditional analysis is used in the signals obtained with the the five pins probe in the configuration shown in Figure 5.16. From this conditional analysis is obtained information about the electron temperature, saturation current, floating potential, plasma potential and electron density. The times of reference for the conditional analysis are the times when extreme events are detected in the pin I_s. The temperature was calculated using the triple probe and the potential sweep techniques and a comparison is done.

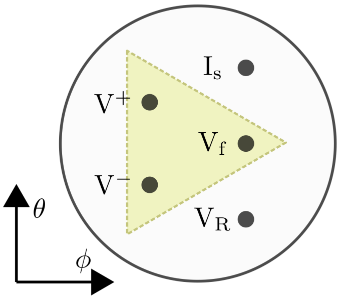

Figure 5.16: Pin configuration for comparison between triple probe and sweep potential techniques. The shadowed triangle shows the spatial distribution of the triple probe array with the pins to measure the floating potential V_f, the positinve potential V^+ and the negative potential V^- of the bias source. The V_R pin is where the sweep potential is set and the I_{sat} is the pin where saturation current is measured. Also, the directions poloidal θ and toroidal ϕ are shown.

The extreme events in the ion saturation current and the reference time in the signals used to calculate the temperature with the triple probe technique are show in Figure 5.17. Inn the raw signals can not be observed any special behavior at the times when the extreme events are detected. Therefore, the conditional analysis is used to obtain information about the temperature.

For the triple probe technique the conditional analysis is calculated in the following way: around each maximum of each extreme event, we collect M_b points backward and forward. In the case of our analysis M_b was chosen as 40 points, that gives a time Δt of $\pm 20\mu$s. Taking the data around each extreme event for the signals V_f and V^+, the temperature profile was calculated for each extreme event. With the set of N_b temperature profiles, the mean one was calculated, producing a *mean extreme event temperature profile* and the results are shown in

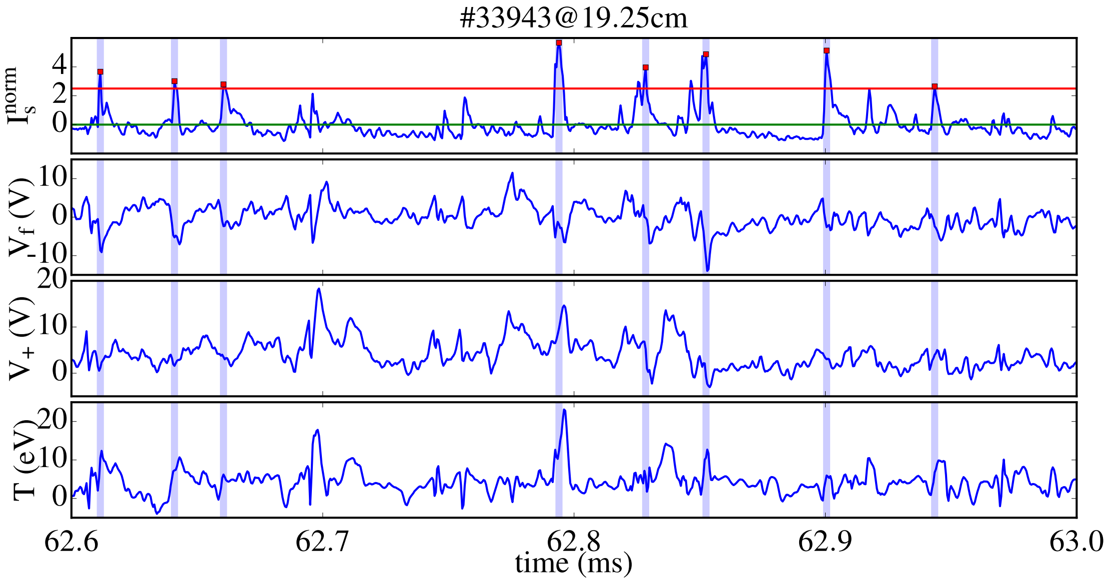

Figure 5.17: Signals as function of time for a short time interval of 0.1 ms. For the I_s, the extreme events peaks in red squares are shown. The red line correspond to the threshold at $I_s^{Norm} = 2.5$ (2.5 standard deviations above the mean value) and the light blue boxes the instant of occurrence of the extreme events in other signals. The temperature was calculated using the expression taking into account the sheath expansion.

Figure 5.18. For the triple probe technique, we have a temperature fall before the extreme event peak and an abrupt rise at the exact moment of the extreme event. The temperature fall is more accentuated for radial positions near the plasma edge. This behavior is not present in the measurement of the potential sweep as we will see. This effect could be due to the fact that the triple probe measure is performed by three pins at different spatial positions. Therefore, the measurement is perturbed by the internal structure of the coherent structure. This kind of signal was also obtained in ref. [71], where measurements of the coherent structure temperature were presented using the triple probe technique and erroneously analyzed as a real temperature fall in the coherent structure.

To see this effect clearly, the five pin probe was set in the configuration shown in Figure 5.19. In this configuration three floating potentials and two saturation currents were used to study the spatial structure of the floating potential when coherent structures are detected.

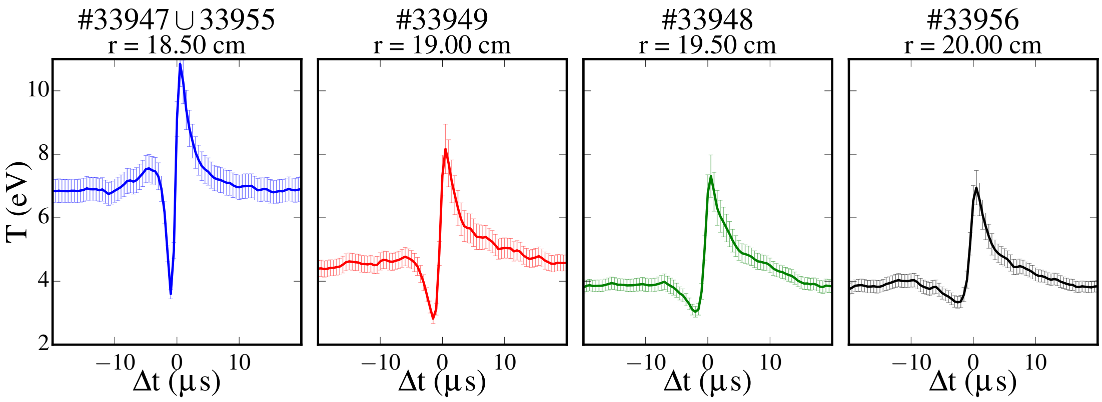

Figure 5.18: Conditional mean for the temperature measured with triple probe technique for different radial positions. The conditional average method was used for these calculations.

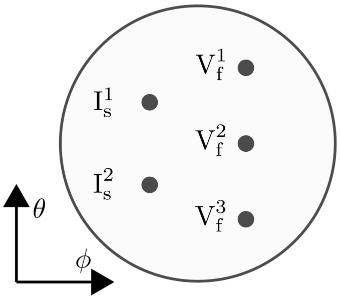

Figure 5.19: Configuration of the LP5p to analyze the spatial structure of the coherent structure via conditional analysis.

The conditional analysis was used taking as a reference the signal of I_s^1, the result is shown in the Figure 5.20. We can see that when there is a peak in the pin of I_s^2, the shape of the fluctuation potential measured in the other pins are different between them, an indication of an internal potential structure of the coherent structure. This potential structure has a poloidal size of the same order of the 5-pin probe size, thereby the measurements with triple probe take different parts of this internal dipole. This fact destroys the assumption that the three pins are in an almost uniform plasma region, which is one of the main hypothesis used to deduce the equation for the triple probe technique.

For the potential sweep technique, again the signal in the saturation current pin is used as the reference for the other signals. In Figure 5.21 are presented the signals for the saturation current, in this case the maximum of the extreme events are marked as red dots. Also, are presented the signal for the potential sweep V_r and the sweep current I_r. It is interesting to note how the current increases quickly

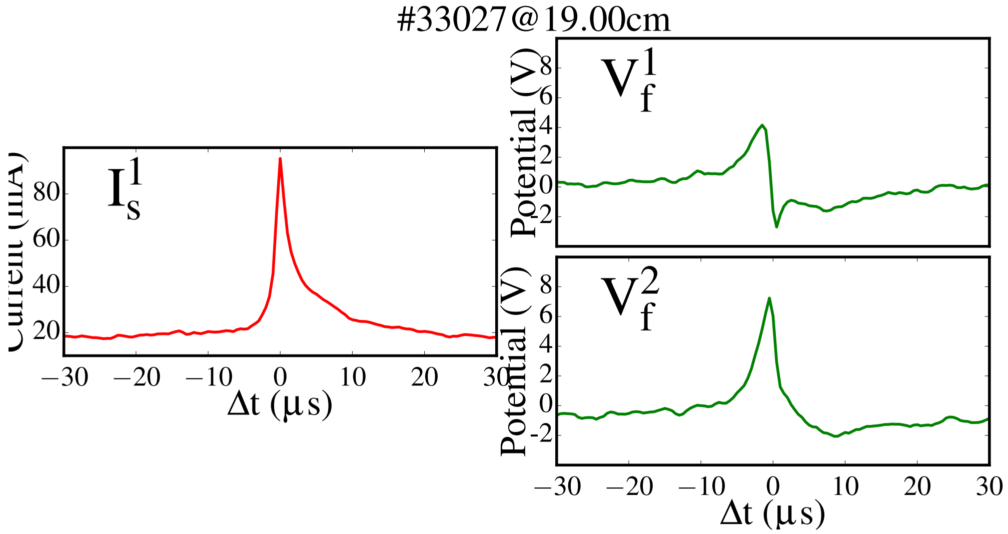

Figure 5.20: Conditional analysis of the V_f signals at different poloidal positions, taking as reference the I_s^1 pin.

for potentials above the 0V, showing the exponential behavior of the current due to the increase in the collection of electrons by the probe. On the contrary, the currents are low when the potential is negative, as it was expected by the limited mobility of the ions.

To apply the conditional analysis to the potential sweep technique, we take the signal of I_R and V_R around the extreme events to get an array of N_b rows and $2M_b + 1$ columns for each signal. Then, we used the n-th column of the arrays of I_R and V_R to get a set of N_b. Those points are used to fit the probe characteristic function given by equation 4.9. where the α parameter is the fixed value given by the mean value as discussed in section 4.1 . From the fit of the function are obtain the temperature, the floating potential and the saturation current. An example of this fit is shown in Figure 5.22, where the upper figure presents the result of the fit taking all the points in the complete interval from 50 ms to 100 ms. In the bottom side if the figure there were used only the points obtained in the extreme events for the conditional analysis at different times around the peak detection. The negative values corresponding to times before the peak detection (which correspond to the time zero) and the positive values correspond to times after the detection of the peak. It is interesting that, at the moment of the peak the saturation current increases to it maximum value, it will produce a peak in the saturation current fit

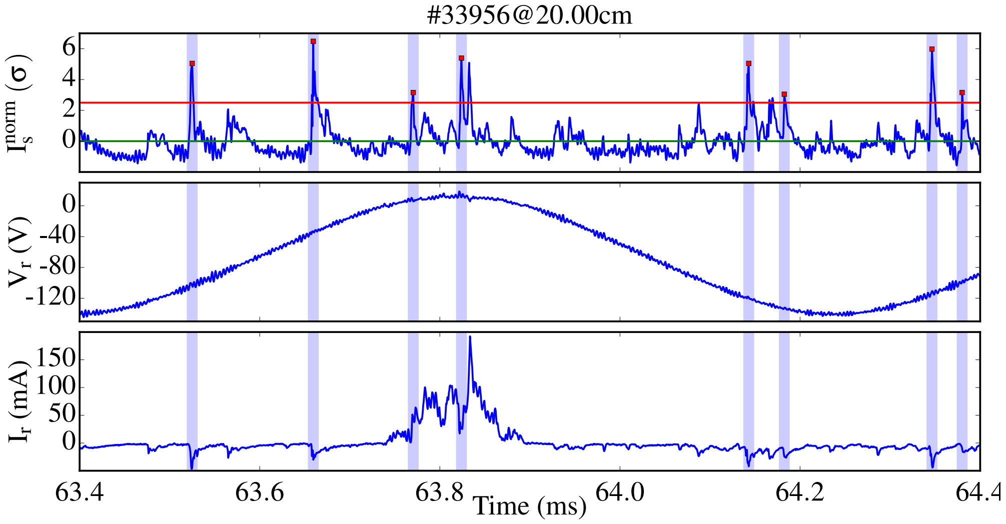

Figure 5.21: Signals as function of time for a short time interval of 1 ms. For the I_s, the extreme events peaks are marked with red squares. The red line is the $\sigma = 2.5$ and the light blue boxes the instant of occurrence of the extreme event in other signals.

parameter in the reference time 0μs. It is important to note that the uncertainties of the points increases due to the diminution of the number of points used in the fit, in this case N_b: one point for each detected extreme event. This issue is the reason to select as the fit method, the one in which the shield expansion factor (the α parameter) is fixed. Because it reduces the number of parameters to fit. Furthermore, as was show in the section 4.1 this method to fit the function gives results compatibles with the obtained when all four parameters are free. However, with lower uncertainties in the fitted parameters.

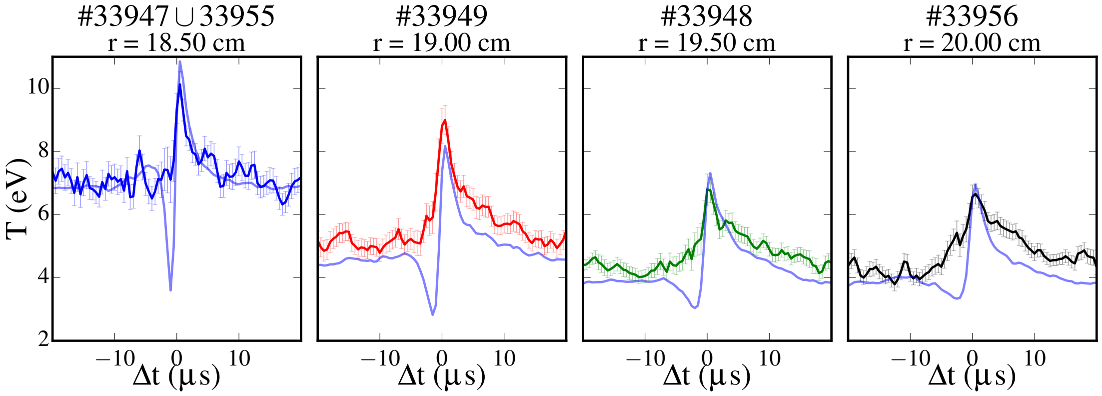

Figure 5.23: The conditional mean for the temperature measured using the potential sweep technique and in light colors the temperature calculated before using the triple probe technique. The conditional mean is presented for different radial positions.

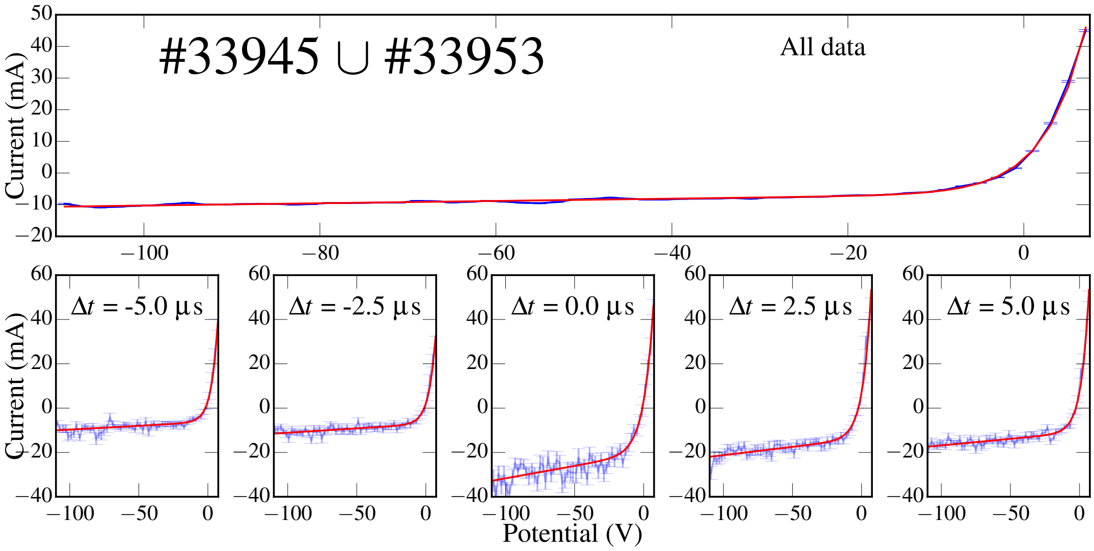

Figure 5.22: Experimental data and fitted function for the characteristic curve of the electrostatic probe using the potential sweep technique. The probe is at 19.75 cm, this is 1.75 cm outside the plasma column. In the upper panel is presented the data for all the time interval, that goes from 50 ms to 100 ms. In the bottom panels the data correspond only to the extreme event, in this case the data for all extreme events at -5 μs, and -1.5 μs before the extreme event peak, at the moment of the extreme event peak (0 μs), at 5 μs, and 2.5 μs after the extreme event peak.

Finally, the result of the conditional analysis is a set of $2M_b + 1$ values of the parameters. This is, we get the mean profile for the temperature, saturation current and floating potential. The temperature profiles obtained using triple probe and potential sweep are shown in Figure 5.23. The most important fact is that there is a pronounced peak of temperature when we have the maximum of the extreme event intensity, indicating that coherent structures have a temperature above the surrounding medium. This temperature peak decreases as the radial position increases, indicating a cooling of the coherent structure as it goes away from the plasma column. When we compare the triple probe and potential sweep techniques it is found that the maximum of the temperature peak is compatible between the two techniques. However, the negative peak in the temperature observed with the triple probe is not present in the case of the potential sweep, indicating a problem with the triple probe technique measurement that is related with the spatial distributions of the used pins. It is interesting that the temperature peak at, least in the $\theta - r$ plane is synchronous with the density peak. Similar result was also obtained in the simulations presented in Ref. [50], where conditional analysis was performed in the data obtained using numerical simulations. The existence of this temperature peak indicates an energy transport caused by the propagation of the coherent structure associated with the extreme event, as it moves from the plasma column to the SOL and even to the chamber wall.

In the Figure 5.24 is shown maximum coherent structure temperature value for different radial positions, obtained using the triple probe and potential sweep methods. Besides, the mean value of the background is presented. To calculate the background value, the temperature values were selected for times outside the extreme event mean time, this is, time values before -10μs and after 10μs. It can be seen that measurements are compatible using the two methods. Therefore, despite of the distortion in the mean profile in the triple probe measurement, the values of the background and maximum and maximum temperature are compatibles for the two methods. It is interesting to note that the difference between the temperature if the peak and the surrounding media seems to decrease as the radial position increases.

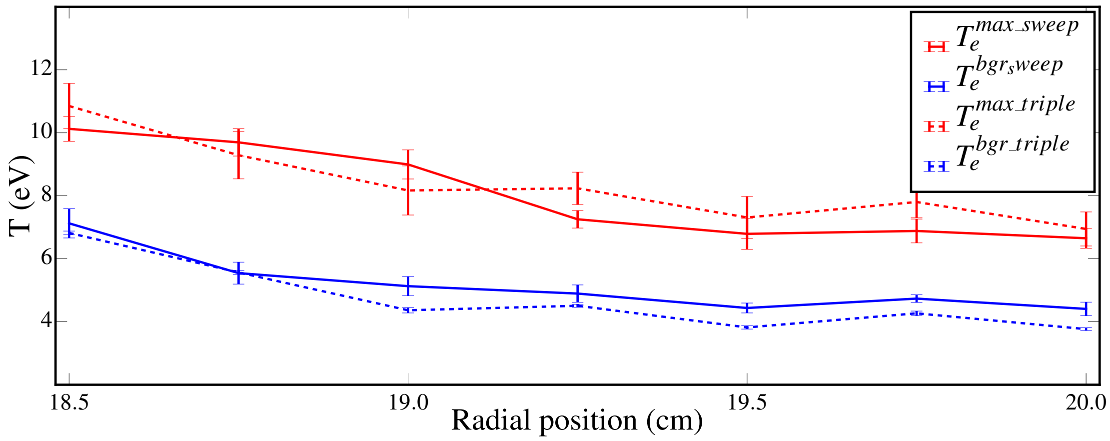

Figure 5.24: Maximum temperature values for the coherent structure (red) and background plasma temperature (blue) at different radial positions. The solid lines indicates the use of the triple probe technique and the dotted lines the use of the triple probe technique.

5.4.4 Saturation current and floating potential analysis for coherent structures

From the conditional analysis applied to the potential sweep we can also obtain the *mean profile* in time for the V_f and I_s. Furthermore, applying the conditional analysis to the signals of I_s and V_f obtained in the pins shown in Figure 5.16, we can obtain a mean profile in a direct way to compares with the results of the potential sweep. The resulting profiles of this analysis and the profiles obtained via potential sweep for the I_s signals are shown in Figure 5.25. As it can be seen, the results obtained using the potential sweep technique and the results of the direct measurement of the saturation current are compatible. The increase in the mean time of the extreme events that was observed in the results presented in Section 5.3 is also obtained.

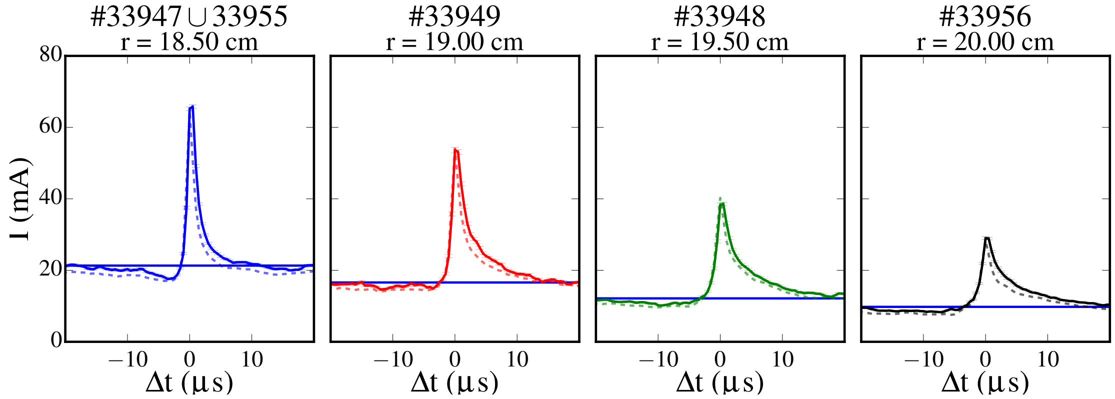

Figure 5.25: The conditional mean for the saturation current using the data from potential sweep technique and direct measurement in light color. The conditional mean was calculated for different radial positions but the distance between the probes did not change.

In Figure 5.26 it is presented the results for the mean profile of the V_F using conditional analysis, obtained by the direct measurement and by the potential sweep technique. As the pins are in different positions with respect to the reference probe, that corresponds to different parts of the coherent structure, the obtained mean profiles have different shapes as it was shown in Figure 5.20. The pin that was used for the potential sweep, detect a sharper peak of potential, instead, the pin at floating potential detect an abrupt change in the polarity. There is a decrease in the value of the potential peak as the radial positions are far from the plasma column edge, decreasing from 6V in the innermost position to 1V at the outermost position. Another interesting aspect is that the mean life of the coherent structure is around 15μs and this time interval is almost the same for the perturbations observed in the temperature, saturation current and fluctuating potential.

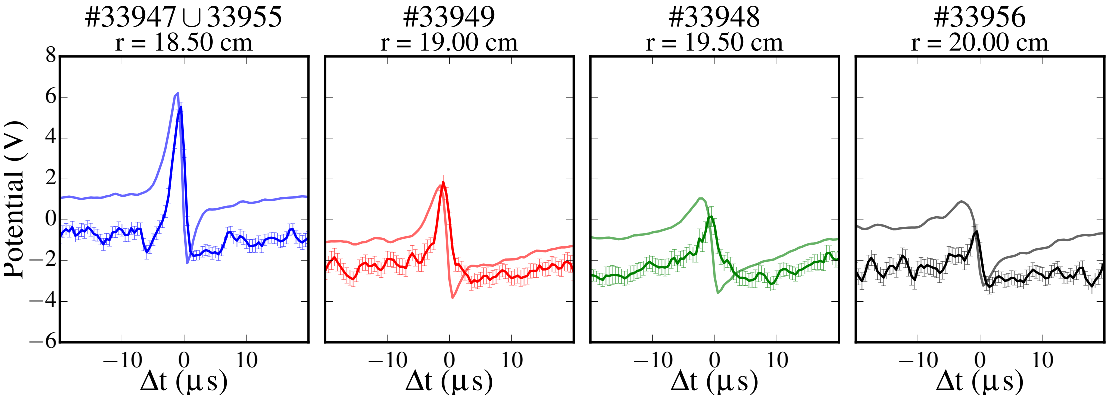

Figure 5.26: The conditional mean for the floating potential using the data from the potential sweep technique with uncertainties and direct measurement in light colors. The conditional mean was calculated for different radial positions.

5.4.5 Plasma potential and density of coherent structures

As we can calculate the conditional analysis for the saturation current, floating potential and temperature, it is possible calculate the conditional analysis of the density n and plasma potential V_p for coherent structures. To perform those calculations we used the equations presented in the section 3.1.2. The expressions are repeated here: equation 3.32 for the plasma potential

$$V_f = V_p - \ln\left(\frac{I_{is}}{I_{es}}\right) T_e \tag{3.32}$$

and equation 3.34 for the density

$$n = \frac{I_s}{eA_i}\left(\frac{2\pi m_i}{kT_e}\right)^{1/2} \tag{3.34}$$

with $\ln(I_{si}/I_{se}) \approx 3$. The result of these calculations are shown in Figure 5.27. As expected, there is a density peak at the moment of the coherent structure detection. Those peaks are more sharper for radial positions near the plasma border, but it is not possible conclude if this is an effect of the coherent structure size or the coherent structure velocity: if the velocity is higher but the size is the same, the measured effect in the probe position will be a sharper peak in time. For the plasma potential there is only a peak when the coherent structure is measured, this is different from the fluctuation potential shape, indicating the importance of the temperature contribution to the potential measurement. In both measurements, the uncertainties are mainly dominated by the uncertainties of the temperature calculation.

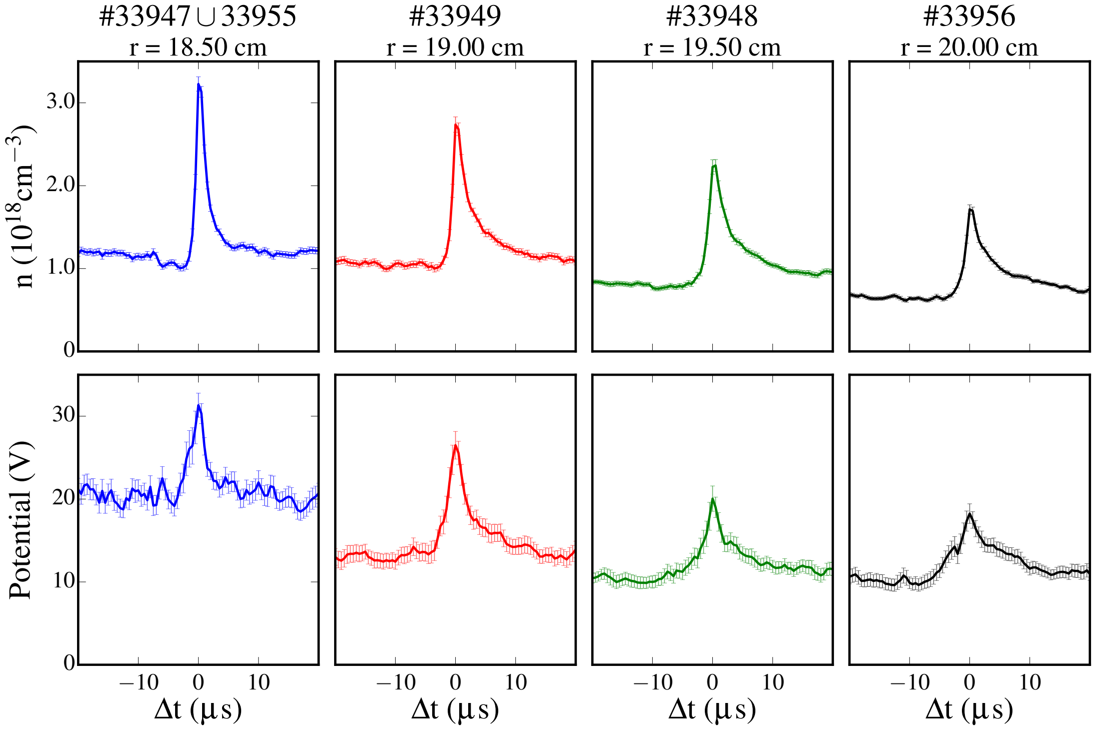

Figure 5.27: The conditional mean for the density and plasma potential. The conditional mean was calculated for different radial positions.

Chapter 6

Conclusions and perspectives

As shown in the previous chapters, almost all the necessary tools to study the effect of temperature fluctuations on the turbulence properties in the plasma edge region of TCABR were developed and results in stationary standard plasma conditions were obtained. As part of the project, were constructed a set of amplifier circuits, with the output designed to couple the impedance of coaxial cable used to connect the measurement circuit (localized as close as possible to the probes) up to the ADCs (localized ∼5m far from the probes). Also, were developed codes to analyze data from the triple probe technique and the sweep potential technique. The codes to perform the conditional analysis used to characterize the bursts were also developed in the work.

The inclusion of the sheath expansion effect introduced by the α parameter enhances the quality of the data fit for the sweep potential technique. However, it was shown that when α is a free parameter, there is an increase in the correlation between the ion saturation current I_s and the electron temperature T_e. Therefore, to avoid this issue, the mean value of α was adopted to perform the fit. A good correspondence between the average of I_s and the fluctuating potential V_f, measured with the sweep potential technique and by direct measurements is obtained. These measured values for I_s and V_f and T_e are in agreement with the expected values for the plasma column edge region. Due to the improvement on the probe characteristic curve fit, considering the sheath expansion effect, the equation to obtain the fluctuating temperature from the tripe probe method was also revised and a new equation including this effect was derived. The recalculated equation gives a temperature estimations whose average value is compatible with those obtained by the potential sweep technique. We found that uncorrected triple probe calculation overestimates the temperature, this overestimation inside the plasma column can be up to 50%.

For the extreme events in TCABR we observed as it was expected, that the ion saturation current has non-Gaussian PDFs, related to the presence of coherent structures. However, the PDF for the V_f is more similar to the Gaussian distribution.

Furthermore, extreme events were studied using the conditional analysis to select peaks in the ion saturation current measurements. From this analysis was found that the order of the size for coherent structures in TCABR is around 2 cm in radial and poloidal directions. The use of conditional analysis shows that the fluctuating potential is modified by coherent structures. It is interesting to note that although coherent structures affect the fluctuating potential, the PDF is a Gaussian distribution.

Data of the ion saturation current from a rake probe were used to measure the characteristics of coherent structures in the radial direction. Those data indicate that coherent structures, associated with extreme events, are tilted in the poloidal direction. This result is compatible with the obtained in HELIMAK, where a 2D grid of probes is used. The tilt of structures implies that the simple and widely used method to estimate the coherent structure velocity: measuring the delay time of events detection and dividing the distance between probes in this time, is erroneous. In order to obtain real velocities values it is needed to know the tilt angle. The analysis of the coherent structures temperature shows a discrepancy between the triple probe and potential sweep techniques. We propose that this discrepancy is due to the spatial configuration of the triple probe, as the three pins are placed at different parts of the internal structure of the coherent structure. Using the temperature results obtained from the potential sweep technique, it was possible to calculate the plasma potential and density using the temperature correction.

After the measurement methods be tested, there are aspects that have to be improved. One aspect that has to be improved is the isolated circuit for current measurements in the triple probe configuration, because the noise level is still high. This circuit allows the measurement of the ion saturation current using the triple probe configuration. Another subject of interest, is test geometrical configurations that could reduce the distortion in the measures of the local temperature measurements by the triple probe method due to the spatial structure of coherent structures.

Further studies can now be done in order to better characterize the coherent structures effects in TCABR plasmas. The new measurements could have the aim to calculate transport of particles and energy due to those structures with the corrections due to the electron temperature. Another possibility is to focus on the study of the changes in the coherent structures behavior when the bias electrode is applied. The main motivation for these studies is that previous works have shown that the electrode improves the confinement conditions in TCABR. Another interesting scenario to perform temperature measurements is when the MHD activity is present. In this condition, the effect of the edge plasma modulation by the MHD activity on effect on the propagation and structure of coherent structures could be performed. All the analysis proposed for these further works will use the hardware and software tools developed in this doctoral work.

Appendix A

Measurement circuits for the probes

It was improved and constructed a set of circuits with the aim to measure in several configurations of triple probe and potential sweep. The improvement of the circuits has the objective to reduce the effect of the transmission lines between the measurement place and the digitizer device. There are basically three kinds of circuits.

- **Potential meter**: This circuit can be used to measure the fluctuating potential V_f, the sweep potential V_R and the positive bias potential for the triple probe technique V_+. The circuit has three stages as shown in figure A.1. The first part is a voltage divider with gain 1/60. Then we have a pre-amplification part with high impedance input. Finally a second amplifier stage with low impedance output to couple with the coaxial cable impedance. The circuit is besides a low-pass filter with cut frequency $\sim$ 700kHz.

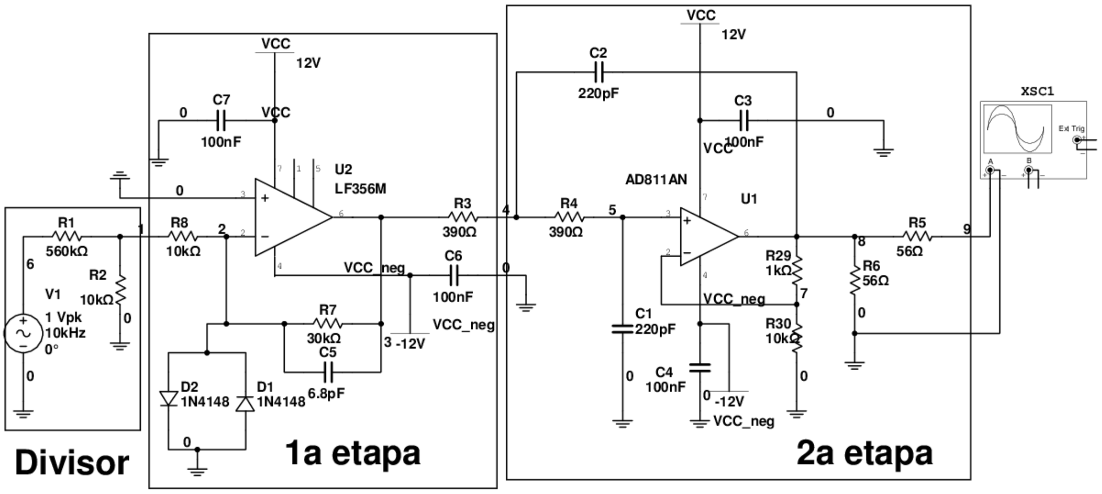

Figure A.1: Potential measurement circuit with the three stages.

- **Current meter**: This circuit is shown in the figure A.1. The circuit has as objective the measurement of the ion saturation current I_s and the current of the potential sweep. The circuit has three stages. First, we have a shunt resistor where the current produces a voltage, following the Ohm's law this voltage is $V = IR$. The second stage is a high impedance input operational amplifier. The third stage is a low impedance output is implemented to couple with the coaxial cable impedance.The second and third stages act as a low-pass filter with cut frequency about 700kHz.

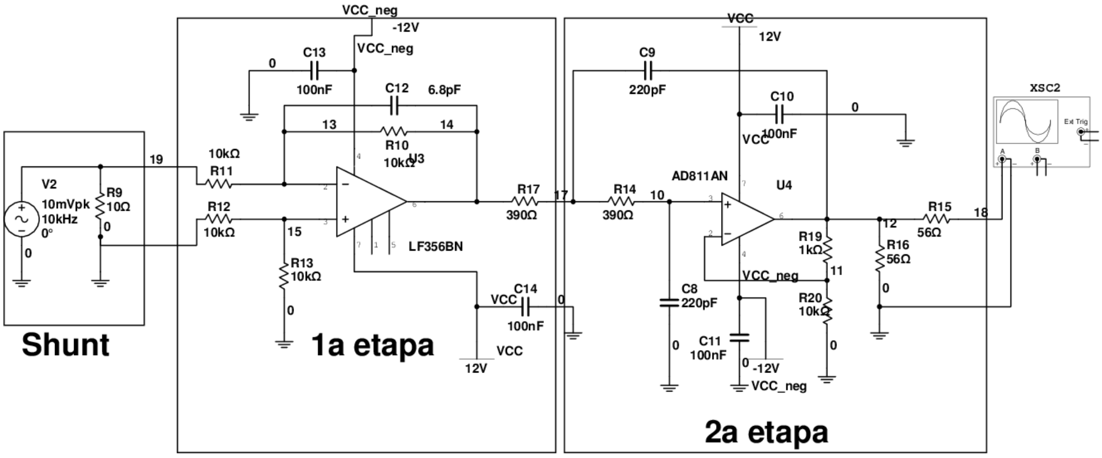

Figure A.2: Current measurement circuit with the three stages.

The frequency response of the circuits used to get the experimental data are shown in figure A.3. It is important to note that for frequencies below 250kHz the gain and phase shift are very similar to the different circuits.

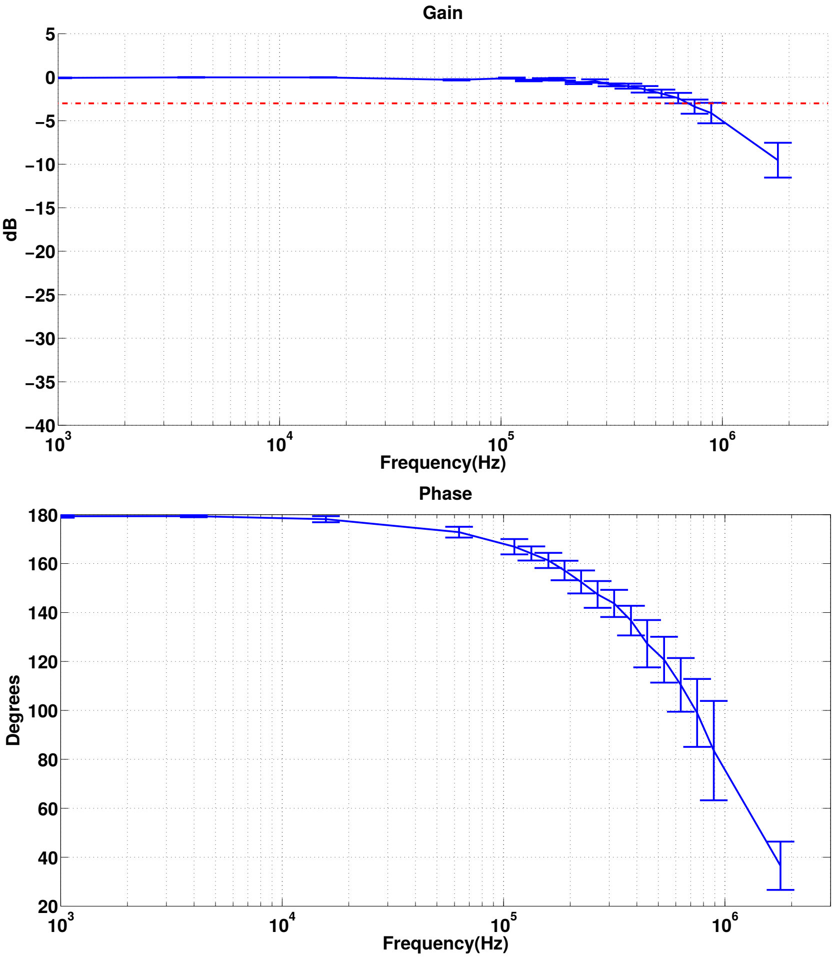

Figure A.3: Mean response in frequency for phase and gain for the complet set of 12 measurement circuits.

- **Isolated meter of current**: This circuit is still in development, because the results have been not satisfactory in the performed measurements. The circuit has two stages isolated electrically, a necessary condition to measure the current in the triple probe technique. In the figure A.4 the part a) corresponds to the input circuit and the b) part the output circuit. The input part (remarked with the square) begins with the shunt resistor as the case of the non-isolated current meter. The potential in the shunt resistor is measured using an operational amplifier in the differential configuration. The signal is amplified and then applied to an IL388 optocoupler that will isolate the input and output circuits leaving the input fluctuating. In the b) part of the figure the output circuit is shown. This circuit performs an amplification and a DC level correction. Finally the output is amplified and the circuit is coupled to the coaxial cable impedance.

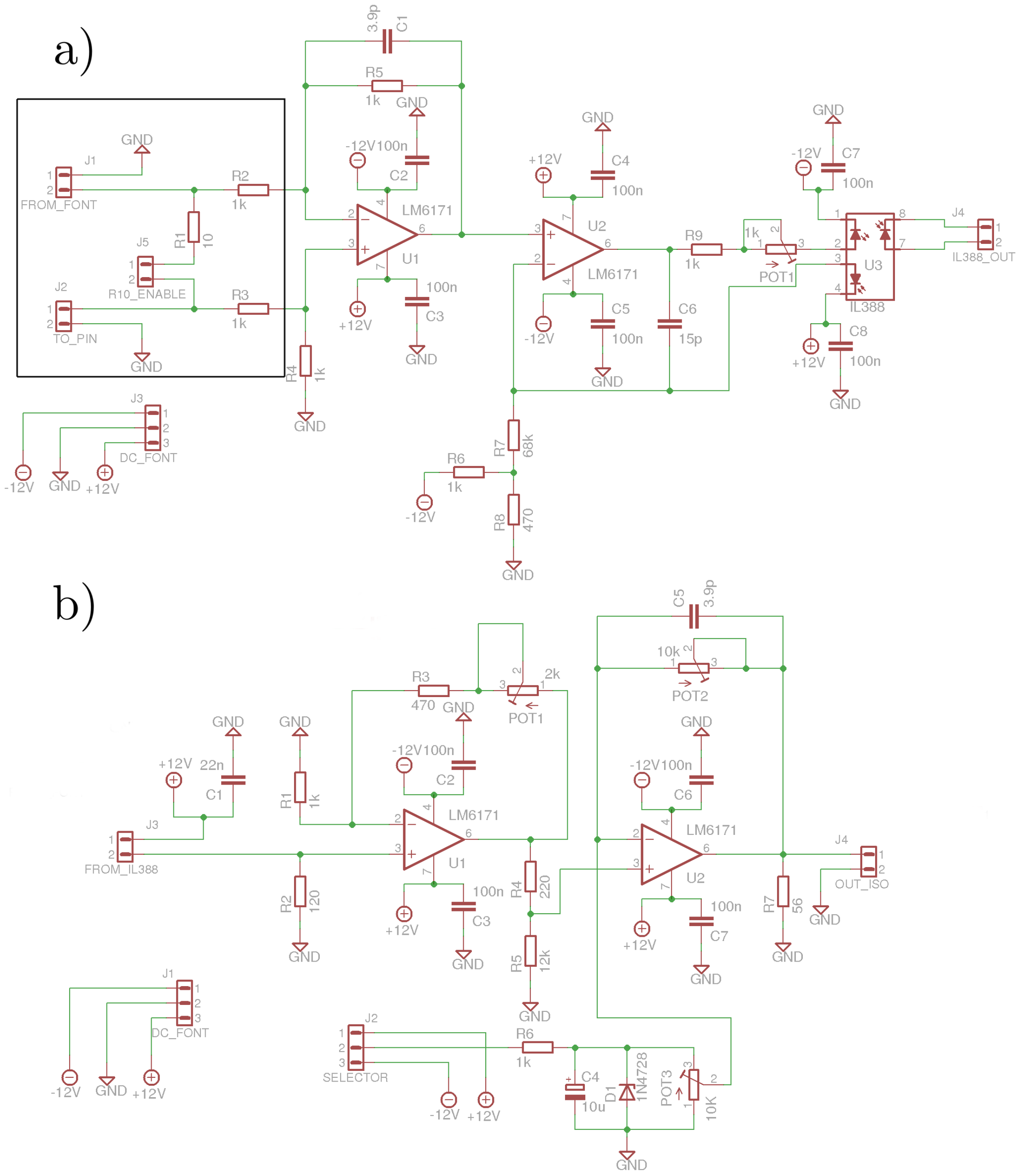

Figure A.4: Circuit for the measurement of the isolated current in the triple pin probe configuration. The circuits of a) and b) are electrically isolated by the IL388 optocoupler.

Appendix B

Gauss-Marquart

The Gauss-Marquardt (or Levenberg-Marquart) method [72] is a widely used method for fitting when the parameters have a nonlinear functional dependence, as is the case for the probe current-voltage relation. To explain the algorithm we will follow [73]. Suppose we have for certain values of x_i a set of experimental data of y_i with uncertainties σ_i. From the measurement $\{(x_i, y_i, \sigma_i), i = 1, ..., N\}$ we need to adjust the function g that depends of $\{a_\nu, \nu = 1, ..., \mu\}$ parameters. Now, to get the best values for the parameters a_i is needed to minimize the function

$$Q = [\mathbf{y} - \mathbf{g}(\mathbf{a})]^t \, \mathbf{V}^{-1} \, [\mathbf{y} - \mathbf{g}(\mathbf{a})] \tag{B.1}$$

where $\mathbf{y}$ is a vector with the N measurements of y and $\mathbf{g}(\mathbf{a})$ is the vector with the fitted function $g_i = g(x_i; \mathbf{a})$ where $\mathbf{a}$ is the vector with the μ parameters. $\mathbf{V}^{-1}$ is the inverse of the variance-covariance matrix of the data where the diagonal elements are the variances σ_i^2 and the terms out of the diagonal are the covariances of the measurements. As $g(\mathbf{x}_i; \mathbf{a})$ is not linear, the equations

$$\left.\frac{\partial Q}{\partial a_\nu}\right|_{\hat{\mathbf{a}}} = 0$$

do not form a linear system. Therefore, one way to solve this problem is to expand the function $g(\mathbf{x}_i; \mathbf{a})$ in a Taylor series around .a vector of values a' that is supposed near to the value of $\hat{\mathbf{a}}$. Then, expanding till first order

$$g(x_i;\hat{\mathbf{a}}) \approx g(x_i;\mathbf{a'}) + \sum_{\nu=1}^{\mu} \left.\frac{\partial g(x_i;\mathbf{a})}{\partial a_\nu}\right|_{\mathbf{a'}} (a_\nu - a'_\nu) \tag{B.2}$$

now defining

$$\Delta g_i = g(x_i;\hat{\mathbf{a}}) - g(x_i;\mathbf{a'}) \tag{B.3}$$

$$X_{i\nu} = \left.\frac{\partial g(x_i;\mathbf{a})}{\partial a_\nu}\right|_{\hat{\mathbf{a}}'} \tag{B.4}$$

$$\Delta a_\nu = \hat{a}_\nu - a'_\nu \tag{B.5}$$

we can express B.2 in the form

$$\Delta g_i = (\mathbf{X}\boldsymbol{\Delta}\mathbf{a})_i \tag{B.6}$$

supposing that the result to first order is approximated, then the equation B.1 can be approximated by

$$Q_a = [\mathbf{y} - \mathbf{g}(\mathbf{a'}) - \mathbf{X}\boldsymbol{\Delta}\mathbf{a}]^t \, \mathbf{V}^{-1} \, [\mathbf{y} - \mathbf{g}(\mathbf{a'}) - \mathbf{X}\boldsymbol{\Delta}\mathbf{a}] \tag{B.7}$$

defining

$$\mathbf{y}' = \mathbf{y} - \mathbf{g}(\mathbf{a'}) \tag{B.8}$$

we have finally

$$Q_a = [\mathbf{y'} - \mathbf{X}\boldsymbol{\Delta}\mathbf{a}]^t \, \mathbf{V}^{-1} \, [\mathbf{y'} - \mathbf{X}\boldsymbol{\Delta}\mathbf{a}] \tag{B.9}$$

Now, an analytic minimization of the equation B.9 is possible because

$$\left.\frac{\partial Q_a}{\partial a_\nu}\right|_{\hat{\boldsymbol{\Delta}}\mathbf{a}} = 0$$

is a linear system of equations and can be solved as

$$\hat{\boldsymbol{\Delta}\mathbf{a}} = \left(\mathbf{M}^{\lambda}\right)^{-1} \mathbf{X}^t \mathbf{V}^{-1} \mathbf{y}' \tag{B.10}$$

where the $\mathbf{M}^{\lambda}$ is defined as

$$M^{\lambda}_{\nu\eta} = (1 + \lambda\delta_{\eta\nu})(\mathbf{X}^t \mathbf{V}^{-1} \mathbf{X})_{\eta\nu}. \tag{B.11}$$

The value of λ is selected to be small, of the order of 10^{-3}. With the value of $\hat{\boldsymbol{\Delta}\mathbf{a}}$ calculated, we improve our approximation of the $\mathbf{a}'$ values using the relation

$$\mathbf{a}'' = \mathbf{a}' + \hat{\boldsymbol{\Delta}\mathbf{a}} \tag{B.12}$$

Now with this $\mathbf{a}''$ it is possible to calculate $Q(\mathbf{a}'')$. The next step is to calculate the difference

$$\Delta Q = Q(\mathbf{a}'') - Q(\mathbf{a}') \tag{B.13}$$

if ΔQ is positive the λ parameter increases typically 10 times. With the new value of λ, are recalculated the values of the equations B.11, B.10 and B.13 until the value of ΔQ becomes negative. When this happens the λ parameter decreases typically 10 times. By doing it iteratively few times, at the end, we obtain the vector of parameters $\hat{\mathbf{a}} \approx \mathbf{a}^n$ with n the number of iterations until the convergence parameter is reached. When the algorithm has been finished the variance-covariance matrix for the parameters has to be calculated in the next way

$$\mathbf{V}(\hat{\mathbf{a}}) \approx \left(\mathbf{X}^t \mathbf{V}^{-1} \mathbf{X}\right)^{-1}$$

where $\mathbf{X}$ is given by equation B.4.

Bibliography

[1] Ongena, J., Koch, R., Wolf, R. & Zohm, H. Erratum: Magnetic-confinement fusion. *Nature Physics* **12**, 717–717 (2016).

[2] Carreras, B. a. Progress in anomalous transport research in toroidal magnetic confinement devices. *IEEE Transactions on Plasma Science* **25**, 1281–1321 (1997).

[3] D'Ippolito, D. A., Myra, J. R. & Zweben, S. J. Convective transport by intermittent blob-filaments: Comparison of theory and experiment. *Physics of Plasmas* **18**, 060501 (2011).

[4] Hutchinson, I. H. *Principles of Plasma Diagnostics* (Cambridge University Press, 2002), 2 edn.

[5] Liewer, P., McChesney, J., Zweben, S. & Gould, R. Temperature fluctuations and heat transport in the edge regions of a tokamak. *Physics of Fluids* **309** (1986).

[6] Chen, S.-L. & Sekiguchi, T. Instantaneous Direct-Display System of Plasma Parameters by Means of Triple Probe. *Journal of Applied Physics* **36**, 2363 (1965).

[7] Hussain, A. K. M. F. Coherent structures reality and myth. *Physics of Fluids* **26**, 2816 (1983).

[8] Cheng, F. F. *Introduction to Plasma Physics* (Plenum Press, 227 West 17h Street, New Yotk, N. Y. 10011, 1974).

[9] Lin, Z., Ethier, S., Hahm, T. S. & Tang, W. M. Size scaling of turbulent transport in magnetically confined plasmas. *Physical Review Letters* **88**, – (2002).

[10] Lawson, J. D. Some Criteria for a Useful Thermonuclear Reactor (1955).

[11] Goebloed, J. P. & Poedts, S. *Principles of magnetohydrodynamics* (Cambridge University Press, The Edinburgh Building, Cambridge CB2 8RU, UK, 2004).

[12] Nakai, S. & Mima, K. Laser driven inertial fusion energy: present and prospective. *Reports on Progress in Physics* **67**, 321–349 (2004).

[13] Smirnov, V. Tokamak foundation in USSR/Russia 1950^s 1990. *Nuclear Fusion* **50**, 014003 (2009).

[14] Mliná, J. *Focus on: JET the european centre of fusion research* (EURATOM, Prague, 2007).

[15] Levinson, S., Beall, J., Powers, E. & Bengtson, R. Space/time statistics of the turbulence in a tokamak edge plasma. *Nuclear Fusion* **24**, 527–539 (1984).

[16] Burrell, K. H. Effects of $\boldsymbol{E} \times \boldsymbol{B}$ velocity shear and magnetic shear on turbulence and transport in magnetic confinement devices. *Physics of Plasmas (1994-present)* **4**, 1499 (1997).

[17] Grenfell, G. G. *Estudo de Efeitos da Polarização Eletrostatica Periférica no Tokamak TCABR.* Master's thesis, Universidade de São Paulo Instituto de Física (2016).

[18] Ferreira, A. A. *et al.* Turbulence and transport in the scrape-off layer TCABR tokamak. *Plasma Physics and Controlled Fusion* **46**, 669–679 (2004).

[19] Ferreira, a. a., Heller, M. V. a. P. & Caldas, I. L. Experimental analysis of mode coupling and plasma turbulence induced by magnetic fields. *Physics of Plasmas* **7**, 3567–3572 (2000).

[20] Ferreira, A. A. *Turbulência em um plasma toroidal medida por sonda electrostáticas.* Master's thesis, Universidade de São Paulo Instituto de Física (1999).

[21] Guimarães Filho, Z. *et al.* Recurrence quantification analysis of electrostatic fluctuations in fusion plasmas. *Physics Letters A* **372**, 1088–1095 (2008).

[22] Guimarães-Filho, Z. O. *et al.* Characterizing electrostatic turbulence in tokamak plasmas with high MHD activity. *Journal of Physics: Conference Series* **246**, 012014 (2010).

[23] Dos Santos Lima, G. Z. *et al.* Self-organized criticality in MHD driven plasma edge turbulence. *Physics Letters, Section A: General, Atomic and Solid State Physics* **376**, 753–757 (2012).

[24] Hack, E. *Desenvolvimento de sonda de vorticidade para caracterizacã0 de turbulência na borda da coluna de plasma no TCABR.* Master's thesis, Universidade de São Paulo Instituto de Física (2016).

[25] Artsimovich, L. Tokamak devices. *Nuclear Fusion* **12**, 215–252 (1972).

[26] Furth, H. P. Tokamak research. *Nuclear Fusion* **15**, 487–534 (1975).

[27] Mazzucato, E. Small-Scale Density Fluctuations in the Adiabatic Toroidal Compressor. *Physical Review Letters* **36**, 792–794 (1976).

[28] Zweben, S. J. *et al.* Edge turbulence measurements in toroidal fusion devices. *Plasma Physics and Controlled Fusion* **49**, S1–S23 (2007).

[29] Pedrosa, M. *et al.* Empirical Similarity of Frequency Spectra of the Edge-Plasma Fluctuations in Toroidal Magnetic-Confinement Systems. *Physical Review Letters* **82**, 3621–3624 (1999).

[30] Ritz, C. P. *et al.* Fluctuation-Induced Energy Flux in the Tokamak Edge. *Physical Review Letters* **62**, 1844–1847 (1989).

[31] Wootton, a. J. *et al.* Fluctuations and anomalous transport in tokamaks. *Physics of Fluids B: Plasma Physics* **2**, 2879 (1990).

[32] LaBombard, B. *et al.* Cross-field plasma transport and main-chamber recycling in diverted plasmas on Alcator C-Mod. *Nuclear Fusion* **40**, 2041–2060 (2000).

[33] Zweben, S. J. Search for coherent structure within tokamak plasma turbulence. *Physics of Fluids* **28**, 974 (1985).

[34] Sarazin, Y. & Ghendrih, P. Intermittent particle transport in two-dimensional edge turbulence. *Physics of Plasmas* **5**, 4214 (1998).

[35] Endler, M. *et al.* Measurements and modelling of electrostatic fluctuations in the scrape-off layer of ASDEX. *Nuclear Fusion* **35**, 1307–1339 (1995).

[36] Grulke, O., Klinger, T., Endler, M. & Piel, A. Analysis of large-scale fluctuation structures in the scrape-off layer of the Wendelstein 7-AS stellarator. *Physics of Plasmas* **8**, 5171–5180 (2001).

[37] Nielsen, A. H., Pécseli, H. L. & Rasmussen, J. J. Turbulent transport in low β plasmas. *Physics of Plasmas* **3**, 1530–1544 (1996).

[38] Liu, H. Q. *et al.* Study of blob-like structures in QUEST. *Journal of Nuclear Materials* **415**, S620–S623 (2011).

[39] Maqueda, R. J. *et al.* Edge turbulence measurements in NSTX by gas puff imaging. *Review of Scientific Instruments* **72**, 931–934 (2001).

[40] Antar, G. Y. *et al.* Experimental evidence of intermittent convection in the edge of magnetic confinement devices. *Physical review letters* **87**, 065001 (2001).

[41] Antar, G. Y., Counsell, G., Yu, Y., Labombard, B. & Devynck, P. Universality of intermittent convective transport in the scrape-off layer of magnetically confined devices. *Physics of Plasmas* **10**, 419 (2003).

[42] Toufen, D. L., Pereira, F. A. C., Guimarães-Filho, Z. O., Caldas, I. L. & Gentle, K. W. Electrostatic turbulence intermittence driven by biasing in Texas Helimak. *Physics of Plasmas* **21** (2014).

[43] Krasheninnikov, S. I. On the origin of plasma density blobs. *Phys. Lett. Sect. A Gen. At. Solid State Phys.* **380**, 3905–3907 (2016).

[44] Krasheninnikov, S. I. On scrape off layer plasma transport. *Phys. Lett. Sect. A Gen. At. Solid State Phys.* **283**, 368–370 (2001).

[45] Furno, I. *et al.* Direct two-dimensional measurements of the field-aligned current associated with plasma blobs. *Physical Review Letters* **106** (2011).

[46] D'Ippolito, D. A., Myra, J. R., Krasheninnikov, S. I., Yu, G. Q. & Pigarov, A. Y. Blob transport in the tokamak scrape-off-layer. *Contributions to Plasma Physics* **44**, 205–216 (2004).

[47] Naulin, V. Turbulent transport and the plasma edge. *Journal of Nuclear Materials* **363-365**, 24–31 (2007).

[48] Angus, J. R. & Umansky, M. V. Modeling of large amplitude plasma blobs in three-dimensions. *Physics of Plasmas* **21**, 012514 (2014).

[49] Riva, F. *et al.* Blob dynamics in the TORPEX experiment: a multi-code validation. *Plasma Phys. Control. Fusion* **58**, 044005 (2016).

[50] Nielsen, A. H. *et al.* Numerical simulations of blobs with ion dynamics. *Plasma Physics and Controlled Fusion* **59**, 025012 (2017).

[51] Bittencourt, J. A. *Fundamental of Plasma Physics* (Springer, 7th floor, Vijaya Building, 17 Barakhamba Road, New Delhi - 110 001, India, 2004).

[52] Nagashima, Y., Inagaki, S., Fujisawa, A., Arakawa, H. & Yamada, T. Observation of Parallel Force Balance for Drift Wave Fluctuation by a Fast Voltage Sweeping Method in a Linear Plasma. *Journal of Physical Society of Japan* **063501**, 10–12 (2015).

[53] Boedo, J. A. *et al.* On the harmonic technique to measure electron temperature with high time resolution. *Review of Scientific Instruments* **70**, 2997–3006 (1999).

[54] Johnson, E. O. & Malter, L. A Floating Double Probe Method for Measurements in Gas Discharges. *Physical Review* **80**, 58–68 (1950).

[55] Ogram, G. L., Chang, J.-S. & Hobson, R. M. The triple-probe method applied to the direct display of plasma parameters in a supersonic flowing continuum plasma. *Journal of Applied Physics* **50**, 726 (1979).

[56] Budaev, V. & Ivanov, R. Correlative properties of edge plasma turbulence in tokamak TV-1. *Journal of Nuclear Materials* **162-164**, 322–326 (1989).

[57] Castro, R. & Heller, M. Temperature fluctuations and plasma edge turbulence in the Brazilian tokamak TBR. *Physics of Plasmas* **3**, 971–977 (1996).

[58] Gatsonis, N. a., Byrne, L. T., Zwahlen, J. C., Pencil, E. J. & Kamhawi, H. Current-mode triple and quadruple Langmuir probe methods with applications to flowing pulsed plasmas. *IEEE Transactions on Plasma Science* **32**, 2118–2129 (2004).

[59] Qayyum, A., Ahmad, S., Ahmad, N., Deeba, F. & Hussain, S. Triple probe measurements in transient plasma of pulsed capacitive discharge. *Journal of Fusion Energy* **34**, 405–410 (2015).

[60] Tsui, H. Y. W. *et al.* A new scheme for Langmuir probe measurement of transport and electron temperature fluctuations. *Review of Scientific Instruments* **63**, 4608 (1992).

[61] Adámek, J. *et al.* A novel approach to direct measurement of the plasma potential. *Czechoslovak Journal of Physics* **54**, C95–C99 (2004).

[62] Filippas, A. V. *et al.* Conditional analysis of floating potential fluctuations at the edge of the Texas Experimental Tokamak Upgrade (TEXT-U). *Physics of Plasmas* **2**, 839–845 (1995).

[63] Johnsen, H., Pecseli, H. L. & Trulsen, J. Conditional eddies in plasma turbulence. *Plasma Physics and Controlled Fusion* **28**, 1519–1523 (1986).

[64] Antar, G. Y., Devynck, P., Garbet, X. & Luckhardt, S. C. Turbulence intermittency and burst properties in tokamak scrape-off layer. *Physics of Plasmas* **8**, 1612 (2001).

[65] Theiler, C., Furno, I., Kuenlin, a., Marmillod, P. & Fasoli, a. Practical solutions for reliable triple probe measurements in magnetized plasmas. *The Review of scientific instruments* **82**, 013504 (2011).

[66] Ghosh, S., Barada, K. K., Chattopadhyay, P. K., Ghosh, J. & Bora, D. Resolving an anomaly in electron temperature measurement using double and triple Langmuir probes. *Plasma Sources Science and Technology* **24**, 015017 (2015).

[67] Laux, M. Application of triple Probes to Magnetized Plasmas. *Contributions to Plasma Physics* **41**, 510–516 (2001).

[68] Birkenmeier, G. *et al.* Magnetic field dependence of the blob dynamics in the edge of ASDEX upgrade L-mode plasmas. *Plasma Physics and Controlled Fusion* **56**, 075019 (2014).

[69] Pereira, F. A. C., Toufen, D. L., Guimarães-Filho, Z. O., Caldas, I. L. & Gentle, K. W. Burst propagation in Texas Helimak. *Plasma Physics and Controlled Fusion* **58**, 054007 (2016).

[70] Guimarães-Filho, Z. O. Personal communication. unpublished (2017).

[71] Spolaore, M. *et al.* Electromagnetic turbulent structures: A ubiquitous feature of the edge region of toroidal plasma configurations. *Physics of Plasmas* **22** (2015).

[72] Marquardt, D. W. An algorithm for least-squares estimation of nonlinear parameters. *Journal of the Society for Industrial and Applied Mathematics* **11**, 431–441 (1963).

[73] Vanin, V., Gouffon, P. & Helene, O. Análise estatística de medidas em ciências exatas (2014).